

Scaling Up 3D Imaging, Analysis, and Culture of Complex Brain Models

by

Justin M. Swaney

B.S. Chemical Engineering
University of Wisconsin-Madison, 2014

SUBMITTED TO THE DEPARTMENT OF CHEMICAL ENGINEERING IN
PARTIAL FULFILLMENT OF THE REQUIREMENTS FOR THE DEGREE OF

DOCTOR OF PHILOSOPHY IN CHEMICAL ENGINEERING
AT THE
MASSACHUSETTS INSTITUTE OF TECHNOLOGY

DECEMBER 2019

© 2019 Massachusetts Institute of Technology. All rights reserved.

Signature of Author

Department of Chemical Engineering
December 11, 2019

Certified by

Kwanghun Chung
Professor of Chemical Engineering
Thesis Supervisor

Accepted by

Patrick Doyle
Professor of Chemical Engineering
Chairman, Committee for Graduate Students

Abstract

The brain is the most complex human organ, containing components from the nanometer scale to the centimeter scale, such as synapses, neurons, and brain regions. However, many experimental techniques in imaging, analysis, and tissue culture have been optimized for smaller brain models. This thesis summarizes a body of work aimed at scaling up imaging, analysis, and tissue culture techniques for large-scale brain models. Fluorescence imaging of large-scale models is limited by diffusion of molecular probes and the resolution of long working distance objectives. We present a technique termed SWITCH that inhibits probe binding to allow for diffusion without the formation of a reaction front. To improve imaging resolution, we present a tissue expansion technique called MAP that physically magnifies tissue samples for super-resolution imaging. We demonstrate a 4-fold increase in effective resolution using long working distance objectives and show that the tissue distortion through expansion is comparable to the deformation that occurs during handling. Volumetric imaging of large-scale models generates petabyte scale data, for which we present horizontally scalable image processing pipelines for analysis of intact mouse brains and cerebral organoids. The mouse brain pipeline allows region-based statistical analysis of protein expression and cell counts. The cerebral organoid pipeline allows single-cell, cytoarchitectural, and morphological analyses to be combined into a hyperdimensional statistical analysis. We use this pipeline to show phenotypic changes during development. In order to overcome limitations in multicolor imaging, we also present a 3D image coregistration pipeline capable of aligning multiple rounds of staining of the same whole-brain sample at single-cell resolution. We show that the average distance between corresponding nuclei after coregistration is less than 4 um. Finally, large-scale tissue cultures are limited by nutrient transport since they lack a vascular system. To address this issue *in vitro*, we fabricated synthetic vasculature by two-photon photopolymerization of polyethylene glycol based resins. Printed micro-vessels were 100 um in outer diameter, durable yet flexible, and permeable to bio-molecules in a tunable manner. Perfusion of vascularized cerebral organoids cultured for 30 days resulted in the expected neuronal differentiation as well as integration of the vascular network. Future studies can use and build on these technical advances to further our understanding of the brain through the use of large-scale brain models.

Acknowledgements

I would like to acknowledge all of my colleagues at MIT for their continued support throughout various research projects. We accomplished a great deal and learned even more together. I have no doubt that those individuals that I have had the privilege to work with at MIT will continue to impact the world in positive ways.

This work never would have been possible without my family. I am grateful for my fiancé, Kassi, who has been with me side-by-side as an MIT PhD student since the beginning. We made it through grad school together, and I'm excited to share our hardships and victories in the future. My brother, Jason, and his wife, Shanon, always gave me a place to stay whenever I went home to Wisconsin during my PhD. My sister, Amy, and neice, Lexi, also welcomed me home when I visited. My dad, Rich, has supported me throughout my entire life and academic career.

Lastly, I'd like to dedicate this thesis to my mother, Margaret Swaney, to whom I owe everything. She has been and will always be my guiding light.

Table of Contents

| | |
|---|-----------|
| Abstract | 2 |
| Acknowledgements | 3 |
| List of figures | 7 |
| List of tables | 10 |
| Abbreviations | 11 |
| Introduction | 13 |
| Multiscale intrinsic complexity of the brain | 13 |
| Trends in biological models used in neuroscience | 13 |
| Evolution of experimental techniques | 13 |
| Thesis aims | 13 |
| 1 Simple, scalable proteomic imaging for high-dimensional profiling of intact systems | 14 |
| 1.1 Summary | 14 |
| 1.2 Introduction | 15 |
| 1.3 Results | 16 |
| 1.4 Discussion | 32 |
| 1.5 Experimental Procedures | 35 |
| 1.6 Supplemental Information | 37 |
| 1.7 Author Contributions | 37 |
| 1.8 Acknowledgments | 37 |
| 1.9 References | 39 |
| 2 Multiplexed and scalable super-resolution imaging of three-dimensional protein localization in size-adjustable tissues | 43 |
| 2.1 Summary | 43 |
| 2.2 Introduction | 44 |
| 2.3 Results | 45 |

| | | |
|----------|---|------------|
| 2.4 | Discussion | 57 |
| 2.5 | Methods | 59 |
| 2.6 | Acknowledgements | 59 |
| 2.7 | Author Contributions | 59 |
| 2.8 | Competing Financial Interests | 60 |
| 2.9 | Methods | 60 |
| 2.10 | References | 67 |
| 3 | Ultrafast immunostaining of organ-scale tissues for scalable proteomic phenotyping | 70 |
| 3.1 | Abstract | 70 |
| 3.2 | Introduction | 71 |
| 3.3 | Results | 72 |
| 3.4 | Discussion | 84 |
| 3.5 | Acknowledgements | 86 |
| 3.6 | Author Contributions | 87 |
| 3.7 | Competing Interests | 87 |
| 3.8 | Methods | 87 |
| 3.9 | References | 95 |
| 4 | Scalable image processing techniques for quantitative analysis of volumetric biological images from light-sheet microscopy | 100 |
| 4.1 | Abstract | 100 |
| 4.2 | Introduction | 101 |
| 4.3 | Materials | 112 |
| 4.4 | Procedure | 116 |
| 4.5 | Anticipated Results | 116 |
| 4.6 | Acknowledgements | 116 |
| 4.7 | Author Contributions | 116 |
| 4.8 | Competing Interests | 117 |
| 4.9 | References | 118 |
| 5 | 3D Imaging and High-Content Morphological Analysis of Intact Human Cerebral Organoids | 120 |
| 5.1 | Introduction | 120 |
| 5.2 | Method | 120 |
| 5.3 | Results | 121 |
| 5.4 | Discussion | 122 |
| 5.5 | Conclusion | 122 |

| | |
|---|------------|
| 6 Vascularization of cerebral organoids using two-photon stereolithography | 123 |
| 6.1 Introduction | 123 |
| 6.2 Method | 123 |
| 6.3 Results | 124 |
| 6.4 Discussion | 124 |
| 6.5 Conclusion | 124 |
| Conclusion | 125 |
| 6.6 Thesis summary | 125 |
| 6.7 Future work | 125 |
| Appendix 1: Curriculum Vitae | 126 |
| Appendix 2: Image processing protocol | 129 |
| Part A: Destriping LSFM images using pystripe | 130 |
| Part B: Stitching LSFM stacks using TSV | 132 |
| Part C: Atlas alignment with manual refinement using nuggt | 136 |
| Appendix 3: Supplemental Information | 147 |
| Chapter 1 | 148 |
| Chapter 2 | 148 |
| Chapter 3 | 148 |
| Chapter 4 | 148 |
| Chapter 5 | 148 |
| Chapter 6 | 148 |

List of figures

Figure 1.1 pp

Synchronizing Dialdehyde-Tissue-Gel Formation Enables Scalable Tissue Preservation

Figure 1.2 pp

SWITCH and Co-registration Algorithms Enable Highly Multiplexed Imaging at Single-Cell Resolution

Figure 1.3 pp

SWITCH Enables Proteomic Imaging and High-Dimensional Quantitative Phenotyping of Human Clinical Samples

Figure 1.4 pp

SWITCH Enables Simple, Rapid, and Scalable Tissue Clearing

Figure 1.5 pp

SWITCH Enables Visualization and Quantitative Analysis of Entire Myelinated Fiber Tracts

Figure 1.6 pp

SWITCH Increases Uniformity of Antibody Labeling in Thick Tissues

Figure 2.1 pp

Magnified and accessible 3D proteome library of whole intact organs

Figure 2.2 pp

Comparison of multiscale architectures before and after MAP processing

Figure 2.3 pp

Super-resolution imaging showing the 3D proteome library and subcellular details of MAP-processed intact tissue

Figure 2.4 pp

Multiplexed staining of MAP-processed tissue

Figure 2.5 pp

Intercellular connectivity and its reconstruction at single-fiber resolution in MAP-processed tissue

Figure 2.6 pp

Immunolabeling and imaging of thick MAP-processed tissues

Figure 3.1 pp

eFLASH enables rapid, uniform, and cost-efficient labeling of organ-scale tissues

Figure 3.2 pp

Single eFLASH protocol enables complete and uniform staining of various tissue types with a wide range of molecular probes

Figure 3.3 pp

Quantitative brain-wide cell type mapping

Figure 3.4 pp

Brain-wide comparison of genetic cell-type labeling and eFLASH-driven protein-based cell type labeling

Figure 3.5 pp

Multidimensional analysis of an eFLASH-stained marmoset brain block at single cell resolution

Figure 4.1 pp

Overall image processing pipeline for whole brain analysis

Figure 4.2 pp

Destriping of light-sheet microscopy images using pystripe

Figure 4.3 pp

Stitching and illumination correction of light-sheet microscopy images using
TSV

Figure 4.4 pp

Atlas alignment and region-based fluorescence quantification using nuggt

List of tables

| | |
|---|----|
| Table 5.1 This is an example table . . . | pp |
| Table x.x Short title of the figure . . . | pp |

Abbreviations

| | |
|------------------|---|
| 3D | three-dimensional |
| AA | acrylamide |
| ABA | Allen Brain Atlas |
| BAC | bacterial artificial chromosome |
| BSA | bovine serum albumin |
| CB | calbindin |
| ChAT | choline acetyltransferase |
| CLARITY | Clear Lipid-exchanged Acrylamide-Hybridized Rigid Imaging/Immunostaining/In Situ Hybridization-Compatible Tissue-Hydrogel |
| CR | calretinin |
| DTI | Diffusion Tensor Imaging |
| eFLASH | electrophoretically driven Fast Labeling using Affinity Sweeping in Hydrogel |
| ECC | error-correcting code memory |
| EGDGE | ethyleneglycol diglycidyl ether |
| EX-313 | glycerolpolyglycidyl ether |
| FFT | fast Fourier transform |
| FISH | fluorescence in situ hybridization |
| GA | glutaraldehyde |
| GABA | gamma-aminobutyric acid |
| GE21 | 1,4-butanediol diglycidyl ether |
| GE23 | dipropylene glycol diglycidyl ether |
| GFAP | glial fibrillary acidic protein |
| (e)GFP | (enhanced) green fluorescent protein |
| GPU | graphics processing unit |
| HCl | hydrochloric acid |
| IEG | Immediate Early Gene |
| IHC | immunohistochemistry |
| LA-ICP-MS | laser-ablation inductively coupled plasma |

| | |
|-----------------|--|
| | mass spectrometry |
| LSFM | light-sheet fluorescence microscopy |
| MALDI-MS | matrix-assisted laser desorption ionization mass spectrometry |
| MAP | Magnified Analysis of Proteome |
| mRNA | messenger ribonucleic acid |
| NA | numerical aperture |
| NaDC | sodium deoxycholate |
| NF-M | neurofilament medium subunit |
| NPY | neuropeptide Y |
| NeuN | neuronal nuclei |
| O/N | overnight |
| PBS(T) | phosphate-buffered saline (with Triton X-100) |
| PV | parvalbumin |
| PFA | paraformaldehyde |
| RI | refractive index |
| RT | room temperature |
| SDS | sodium dodecyl sulfate |
| SE | stochastic electrotransport |
| SHIELD | Stabilization to Harsh Conditions via Intramolecular Epoxide Linkages to Prevent Degradation |
| SOX2 | (sex determining region Y)-box 2 |
| SST | somatostatin |
| SWITCH | System-Wide Control of Interaction Time and Kinetics of Chemicals |
| TBR1 | T-box brain transcription factor 1 |
| TH | tyrosine hydroxylase |

Introduction

Multiscale intrinsic complexity of the brain

Brain = Complex system with components over multiple length scales. This complexity is intrinsic as opposed to incidental...

Trends in biological models used in neuroscience

Trend towards more larger, more complex brain models in neuroscience—presumably to model more complex phenotypes

Evolution of experimental techniques

Techniques optimized for simpler systems, hard to apply to directly to these new models

Technological breakthroughs in neuroscience are often those advances that allow researchers to attack long-standing biological questions in new ways.

CLARITY, optogenetics, organoid culture - all examples of this for different reasons

Thesis aims

This work is aimed at addressing technical challenges associated with scaling up the staining and imaging of large brain models, the computational analysis of whole-brain scale datasets, and the culture of organoid brain models.

Chapter 1

Simple, scalable proteomic imaging for high-dimensional profiling of intact systems

Evan Murray*, Jae Hun Cho*, Daniel Goodwin*, Taeyun Ku*, **Justin Swaney***, Sung-Yon Kim, Heejin Choi, Young-Gyun Park, Jeong-Yoon Park, Austin Hubbert, Margaret McCue, Sara Vassallo, Naveed Bakh, Matthew P. Frosch, Van J. Wedeeng, H. Sebastian Seung, and Kwanghun Chung¹

1.1 Summary

Combined measurement of diverse molecular and anatomical traits that span multiple levels remains a major challenge in biology. Here, we introduce a simple method that enables proteomic imaging for scalable, integrated, high-dimensional phenotyping of both animal tissues and human clinical samples. This method, termed SWITCH, uniformly secures tissue architecture, native biomolecules, and antigenicity across an entire system by synchronizing the tissue preservation reaction. The heat- and chemical-resistant nature of the resulting framework permits multiple rounds (>20) of relabeling. We have performed 22 rounds of labeling of a single tissue with precise co-registration of multiple datasets. Furthermore, SWITCH synchronizes labeling reactions to improve probe penetration depth and uniformity of staining. With SWITCH, we performed combinatorial protein expression profiling of the human cortex and also interrogated the geometric structure of the fiber pathways in mouse brains. Such integrated high-dimensional information may accelerate our understanding of biological systems at multiple levels.

¹* indicates co-first authorship.

1.2 Introduction

Biological systems are comprised of vast numbers of molecules, cell types, and intricate tissue organizations (Alivisatos et al. 2013; Kasthuri et al. 2015; Yuste 2015). Understanding the complex interactions of these components is essential for many fields of biology and often requires high-dimensional information across many scales. Although it is desirable to obtain such information from the same tissue due to large individual variations, combined measurement of many molecular and anatomical traits remains an unmet goal in biology despite the remarkable success of current pioneering methods, such as array tomography (Rah et al. 2013).

Rapidly evolving tissue-clearing techniques may enable multiplexed labeling and imaging of intact samples using light microscopy (Chung et al. 2013; Richardson & Lichtman 2015; Susaki et al. 2014). For instance, the CLARITY technique has demonstrated three rounds of immunostaining of mouse brain tissue (Chung & Deisseroth 2013). However, we have noticed that the polyacrylamide-based framework loses structural integrity upon repeated exposure to the elution condition. Recent reports also suggest that preservation of antigenicity in the CLARITY method may not be optimal (Renier et al. 2014). Furthermore, the necessary tissue-gel hybridization step requires delivery of charged thermal initiators with limited diffusivity and stability. This necessity imposes a limit on the tissue size that can be processed without the use of transcardial perfusion.

We set our goal to develop a simple, scalable, and generalizable tissue-processing method for proteomic imaging of intact biological systems. To achieve this, we created SWITCH (system-wide control of interaction time and kinetics of chemicals), which tightly controls a broad range of chemical reactions in tissue processing via a set of buffers: a SWITCH-On buffer that facilitates chemical reactions between exogenous chemicals and endogenous biomolecules, and a SWITCH-Off buffer that suppresses the reactions. SWITCH-mediated fixation transforms tissue into a heat- and chemical-resistant hybrid while preserving tissue architecture, native molecules, and their antigenicity to a degree suitable for multiplexed proteomic imaging. The hybrids can be rapidly cleared at high temperature without damage. The method does not require perfusion and is thus applicable to both animal and large human samples. In molecular labeling of the processed samples, SWITCH controls probe-target binding kinetics to improve probe penetration depth and the uniformity of molecular labeling. This method is simple, passive, and does not require any special equipment or reagents.

Using SWITCH, we demonstrated that a minimum of 22 rounds of molecular labeling of a banked postmortem human tissue with precise co-registration of multiple datasets at single-cell resolution is possible. We also demonstrated extraction of a wide range

of system variables, such as various cell types and microvasculature from a single sample. In summary, we have developed simple tissue processing methods and a volumetric co-registration algorithm that can be readily adopted by most laboratories for scalable proteomic imaging of intact biological systems.

1.3 Results

1.3.1 Synchronizing Dialdehyde-Tissue-Gel Formation Enables Scalable Tissue Preservation

First, we sought to develop a way to transform animal and human samples into a mechanically and chemically stable form for multiplexed imaging. We hypothesized that small, non-ionic, multifunctional crosslinkers might satisfy two key requirements for such a transformation: (1) rapid penetration without the use of perfusion and (2) a high degree of molecular crosslinking to improve sample durability (Sung et al. 1996). Among many options, we chose to evaluate the following owing to their small size and high water solubility (Figure 1.1A): ethyleneglycol diglycidyl ether (EGDGE), dipropylene glycol diglycidyl ether (GE23), 1,4-butanediol diglycidyl ether (GE21), glycerolpolyglycidyl ether (EX-313), and glutaraldehyde (GA).

We found that all of these chemicals except GE23 formed a solid gel upon incubation with 15% bovine serum albumin (BSA), indicating the formation of a crosslinked network (Figure 1.1B). We examined the stability of the gels along with poly-acrylamide (AA)-BSA gels by measuring the change in their volume after incubation in a 200 mM SDS solution heated to 80C (elution condition). AA-BSA gels swelled and became fragile after exposure to the harsh condition (Figures 1.1B and 1.1C), whereas multifunctional fixative-BSA gels maintained their structural integrity. In particular, GA-BSA gels showed minimal volume change at a wide range of BSA and GA concentrations, whereas others only gelled at high protein concentrations (Figure 1.1C). This result indicates that multifunctional fixatives alone might be sufficient to form a stable matrix that can withstand the harsh elution condition. However, because the average protein content throughout mouse brain samples is around 10% and may be lower within certain regions, we decided that GA is the crosslinker most likely to form a uniform framework throughout all regions of a sample.

Next, we asked whether GA can rapidly penetrate tissue to form a uniform tissue-gel without the use of perfusion, which is required for processing most human clinical samples. We incubated a non-fixed whole adult rat brain in PBS containing 1% GA for 2 days and

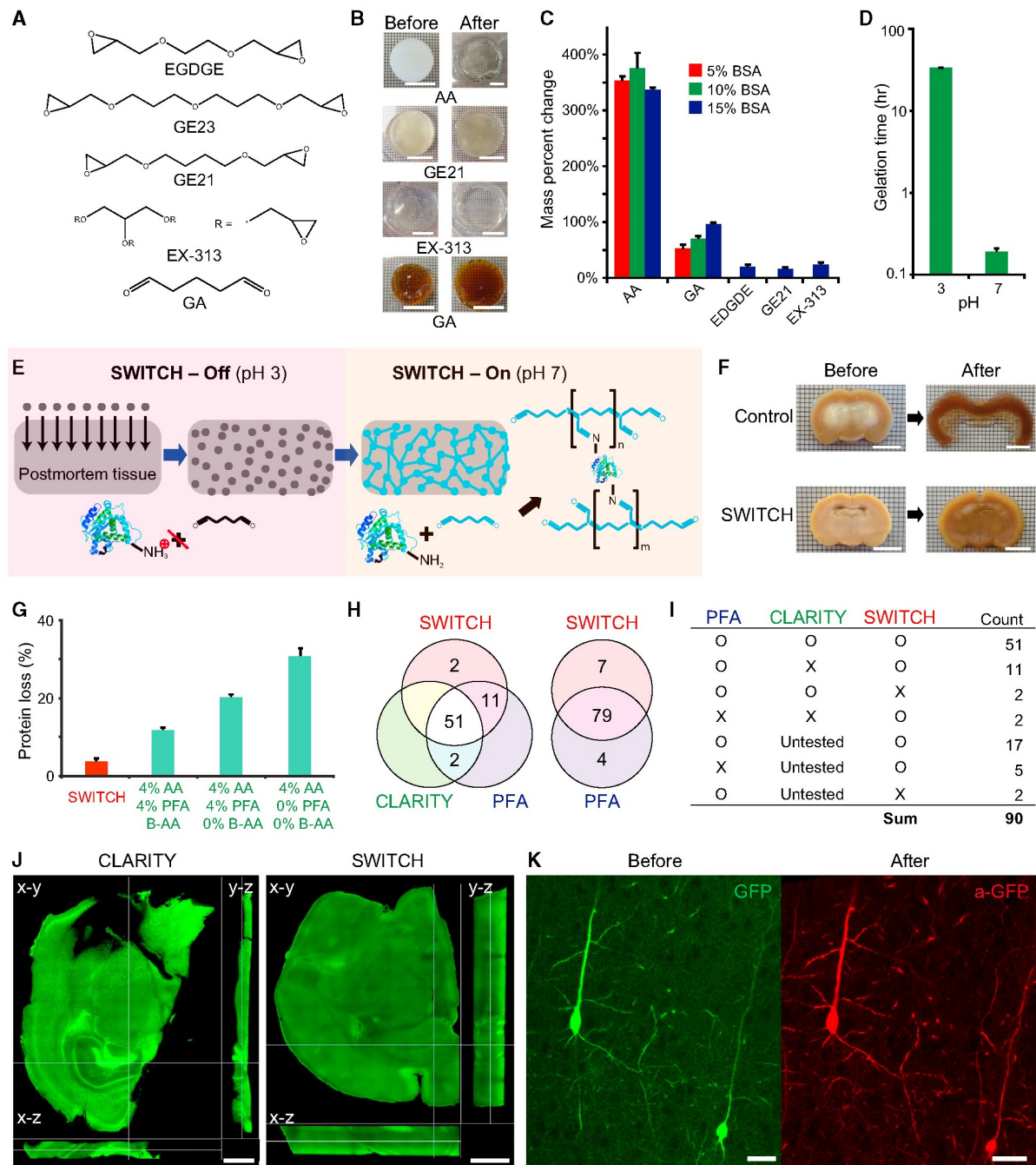


Figure 1.1: Synchronizing Dialdehyde-Tissue-Gel Formation Enables Scalable Tissue Preservation.

(A) Chemical structures of various multifunctional fixatives. (B) Crosslinked protein gels before and after exposure to the elution condition. Scale bars, 10 mm. Polyacrylamide (AA) gel swelled and became fragile, whereas multifunctional fixative gels remained intact with minimal expansion. (C) Mass percent change of crosslinked protein gels after exposure to the harsh condition. EDGDE, GE21, and EX-313 were incapable of forming gels at low BSA concentration. Error bars show mean \pm SD. (D) The gelation time for protein gels crosslinked with GA is nearly 200-fold higher at pH 3 than it is at neutral pH at 4C. Error bars show mean \pm SD. (E) Schematic diagram illustrating the process of scalable and uniform tissue-gel formation without perfusion using SWITCH. GA molecules diffuse into an intact tissue without reacting with biomolecules in pH 3 buffer (SWITCH-Off step). When GA is uniformly dispersed throughout the tissue, the sample is moved to pH 7 buffer (SWITCH-On step) to initiate global gelation/fixation and achieve uniform tissue preservation. (F) Coronal slices from the middle of whole rat brains passively fixed with (bottom) or without (top) SWITCH. After fixation, the middle coronal slices were cut and incubated in the elution condition for 1 hr. The core of the control slice completely disintegrated, whereas the SWITCH-processed slices remained intact. Scale bars, 6 mm. (G) Only 3proteins are lost in SWITCH-processed brain tissues as opposed to 10AA-based methods. Error bars show mean \pm SD. (H and I) Antigenicity of proteins is well preserved throughout the clearing process in SWITCH. Of the antibodies tested, 86 of 90 are compatible with SWITCH. (J and K) SWITCH-mediated fixation maximally preserves macroscopic (J) and microscopic (K) structures throughout the elution process. (J) Cross-sectional images of 1-mm-thick mouse coronal slices after exposure to the elution condition. The CLARITY-processed tissue shows significant tissue deformation and collapse, whereas the SWITCH-processed tissue is highly uniform with no signs of macroscopic deformation. Z-step size, 20 μ m; 10x, 0.3 NA, water-immersion objective. Scale bars, 1 mm. (K) GFP-expressing neurons in the cortex of Thy-1-EGFP mouse brain before and after exposure to the elution condition and anti-GFP staining. 25x, 0.95 NA, water-immersion objective. Scale bars, 30 μ m.

characterized the GA penetration depth and gel formation. Although the small size of GA should make it highly mobile, only the outer layer of the brain was fixed (Figure 1.1F). When a coronal slice from the middle of the brain was exposed to the elution condition, the core of the tissue completely disintegrated, indicating that no gel matrix had formed in the center of the brain (Figure 1.1F). Limited GA penetration has significantly hampered its use in preserving large postmortem tissues (Hopwood 1967). We suspect that rapid reaction of GA with native biomolecules within the outer layer of the brain may cause depletion of GA molecules before they can reach the core.

To overcome this issue, we sought to control the reaction kinetics of GA and biomolecules throughout the system using the SWITCH approach to achieve uniform tissue preservation. We noted that the GA reaction rate is pH-dependent (Hopwood 1970). Indeed, when we titrated solutions of GA and BSA to pH 3, GA-BSA gel formation time increased by nearly 200-fold (Figure 1.1D). Using this pH dependence, we were able to disperse GA uniformly throughout a sample by switching off the crosslinking reaction with a low-pH buffer (Figure 1.1E, left). After 2 days of incubation at low pH, we switched on sample-wide GA-tissue crosslinking by shifting the pH of the sample to a neutral pH (Figure 1.1E, right). Using this passive buffer-switching approach, we were able to achieve complete GA penetration and uniform gel formation throughout the entire rat brain (Figure 1.1F).

1.3.2 Dialdehyde-Tissue-Gel Preserves Structural and Molecular Information Effectively

We next asked whether the GA-tissue-gel has mechanical and chemical properties desirable for multiplexing-based proteomic imaging. Proteomic imaging requires (1) high preservation of endogenous biomolecules and their antigenicity, (2) high structural integrity, and (3) minimal tissue damage during repeated cycles of destaining, labeling, and imaging processes.

We first tested whether endogenous biomolecules are well preserved by measuring protein loss after clearing (see Supplemental Experimental Procedures). We found that control tissues lost an average of 30%–40% protein and AA-tissue-gel lost 10%–20%, but GA-tissue-gel slices lost only 3%–5% of their protein content (Figure 1.1G).

We next asked whether antigenicity of the retained biomolecules is well preserved. We tested 90 antibodies, targeting biomolecules of different sizes (single amino acid to proteins) and subcellular localizations (membrane bound, cytoplasm, nucleus, synapses). Surprisingly, 86 of 90 antibodies were compatible with GA-tissue-gel (Figures 1.1H, and 1.1I, and S1; Table S1). Note that even small molecules, such as dopamine, which are not typically compatible with PFA-fixation, were observable in GA-tissue-gel after the complete removal of lipid bilayers (Figure S1). These biomolecules were stable against heat and chemical treatment, and their antigenicity was well preserved after exposure to elution conditions.

Good structural preservation is essential for resolving protein location with high precision and for studying molecular inter relationships. To characterize the macroscale structural preservation of the samples, we cleared 1-mm-thick tissue blocks using the elution condition and visualized their structural deformation (Figure 1.1J). The PFA-only tissue completely disintegrated. Even the AA-tissue-gel exhibited large deformations overall. GA-tissue-gel, however, showed no signs of structural damage throughout the entirety of the sample.

We next examined structural preservation on a microscopic scale. We imaged GFP-expressing neurons in the cortex of a PFA-fixed 1-mm-thick Thy1-EGFP M line block (Figure 1.1K). We then SWITCH-processed the tissue, cleared it using the harsh elution condition, stained it against GFP, and imaged the same neurons. As shown in Figure 1.1K, the microscopic morphology of the neurons was well preserved throughout the entire process. These results show GA-tissue-gel may be ideal for highly multiplexed structural and molecular phenotyping.

1.3.3 SWITCH and Robust Computational Algorithms Enable Highly Multiplexed Imaging at Single-Cell Resolution

Interrogating the three-dimensional (3D) distribution of molecules, cells, and the overall tissue organization requires precise co-registration of multiple volume images. We first asked if simple manual overlay of two datasets allows precise co-registration. As a stringent test, we used datasets from multi-round imaging of a SWITCH-processed 100- μm -thick human brain slice (100 μm , 200 μm , 200 μm) (Figure 1.2A). The high aspect ratio of such tissues makes it more prone to physical warping, which renders co-registration particularly challenging. We first stained the tissue using DAPI and anti-parvalbumin (PV) antibody. The slice was then enclosed in a space larger than the tissue to exaggerate possible tissue deformation in the mounting process (Figure 1.2B). After imaging, the sample was exposed to the elution condition overnight (O/N) to completely remove imaged probes. We then restained the tissue using the same probes and repeated the imaging process. Note that only GA-tissue-gels could maintain their integrity against the elution treatment. Both AA-tissue-gels and PFA-fixed samples deteriorated rapidly in the same condition.

As predicted, a large degree of tissue warping in the mounting process (Figure 1.2C) made manual overlay insufficient for the task of interrogating a tissue across multiple staining rounds. To achieve precise co-registration of volume images in the presence of such high-degree warping, we custom-designed a robust computational software based on a feature-detection approach that was ideal for our experimental procedure (Figure 1.2D). Each staining round contained one fluorescence channel devoted to a lectin stain because the morphology of blood vessels creates distinctive keypoints that computer vision algorithms are well suited to identify. With the keypoints, the algorithm warps the tissue in a physically plausible manner into the correct position (see Supplemental Experimental Procedures).

As a stringent test of the algorithm, we used the same SWITCH-processed human sample with the high aspect ratio (Figure 1.2A). For each round, the sample was stained with DAPI, lectin, and one antibody to label a target protein. Although at least three antibodies can be used for each round in addition to lectin and DAPI (Figure S2), we chose to use one antibody for each round to eliminate any possible cross-talk between channels. After acquiring images, we destained the sample and began the next round of labeling. We repeated the above procedure 22 times using markers for various cell types (Figure 1.2H; Table 1). Staining was not successful in every round due to the use of non-validated antibodies, sub-optimal staining conditions, or human error, all of which often occur in general laboratory settings and can result in the loss of important samples. However, a SWITCH-processed sample is free from this issue as the tissue can be washed and reused

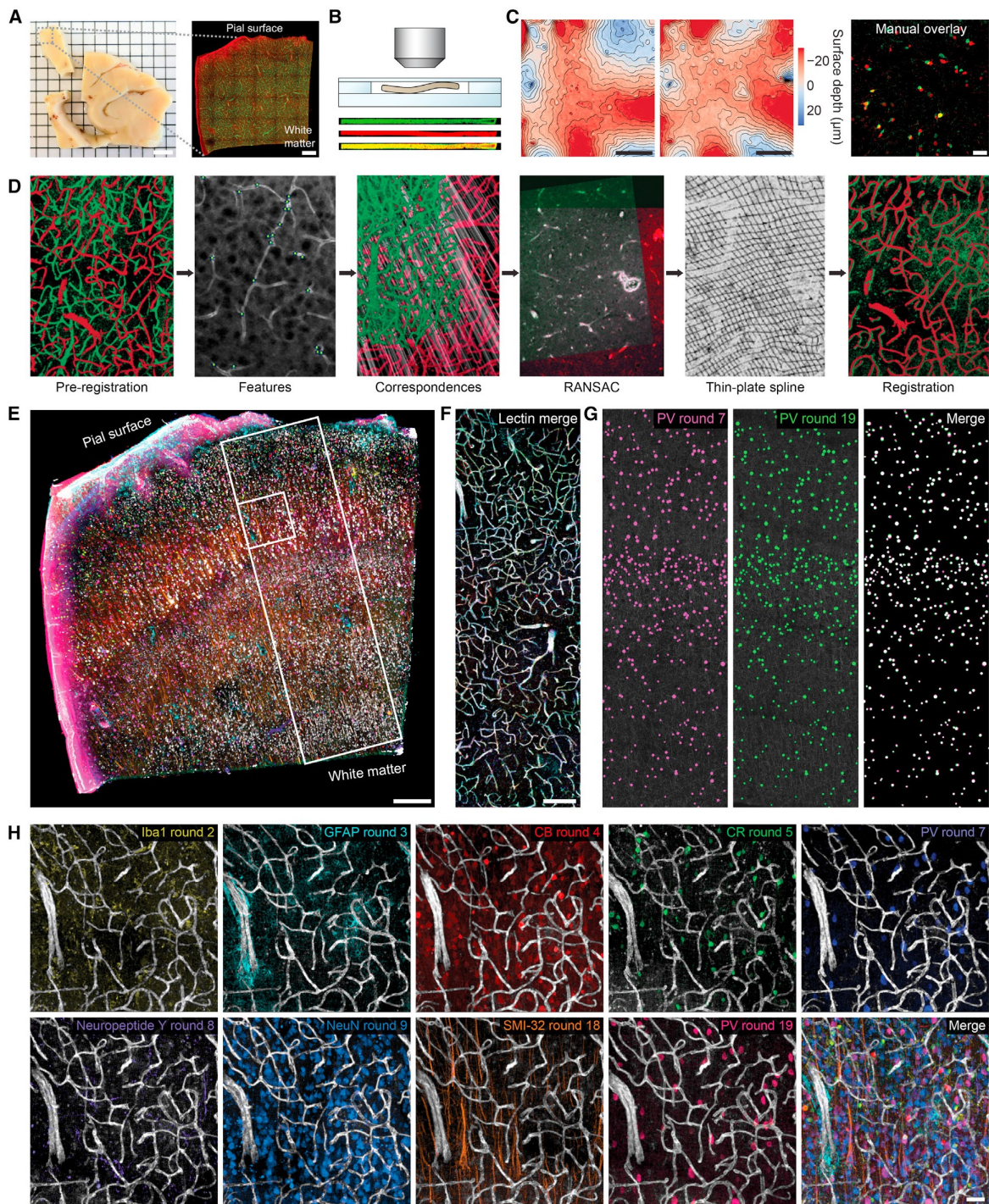


Figure 1.2: SWITCH and Co-registration Algorithms Enable Highly Multiplexed Imaging at Single-Cell Resolution.

(A) The left image shows formalin-fixed postmortem human brain tissue (visual association cortex, Brodmann area 18). The right image shows a 100- μ m section of this brain tissue after SWITCH processing. Scale bars, 5 mm (left), 300 μ m (right). (B) Natural warping of the sample during imaging was enabled by mounting within a chamber space larger than the size of the sample. Representative crosssections of the sample after several rounds of imaging are shown. Sample thickness, 100 μ m. (C) Surface contour maps showing warping of the sample between imaging rounds. Attempted manual overlay of two PV datasets shows that sample warping is too severe for single-cell registration without computational correction. Scale bars, 50 μ m. (D) A flow diagram depicting the sequence of events for automated co-registration of datasets. (E) Fully co-registered image showing an overlay of 9 rounds of immunostaining. A total of 22 rounds of staining of the same tissue was achieved. R#2 (Iba1), R#3 (GFAP), R#4 (calbindin, CB), R#5 (calretinin, CR), R#7 (PV), R#8 (Neuropeptide Y), R#9 (NeuN), R#18 (SMI-32), and R#19 (PV) were used for co-registration and subsequent quantitative analysis (see Figure 3). The boxed regions indicate the ROI's shown in panels. (F–H) Scale bar, 300 μ m. (F) Vasculature labeling from 9 rounds of staining after co-registration. Scale bar, 200 μ m. (G) PV cell counts between rounds 7 and 19. After 12 rounds of imaging, 99PV+ cells were again detected and shown to overlay after co-registration of the datasets. (H) Images of individual channels with corresponding vasculature labeling. Scale bar, 50 μ m.

repeatedly.

We were able to successfully co-register all nine datasets with successful staining (Figures 1.2E and 1.2H; Movie S1). We asked whether changes in the sample might be occurring between staining rounds. To test this, we repeated staining with anti-PV antibodies in rounds 7 and 19 and co-registered the resulting datasets. Even when separated by 12 rounds of labeling, we were able to achieve single-cell accuracy of registration with 99% agreement between the two rounds (Figure 1.2G).

We next performed joint statistical analysis of the integrated cross-talk-free dataset to extract diverse phenotypic information from human brain (Figure 1.3). We included lectin, GFAP, NeuN, SMI-32, and three calcium-binding protein channels—calbindin (CB), calretinin (CR), and PV—in the quantitative analysis. First, we used semi-automated algorithms to identify blood vessels and cells expressing the target antigens (Figures 1.3A and 1.3B) and extract their spatial (x, y, z coordinates) and morphological (e.g., cell soma size) information. Density and size profiles of NeuN-positive cells (Figures 1.3C and 1.3D) enabled us to define the cortical layers (Figure 1.3A) according to established criteria (De Sousa et al. 2010). NeuN+ density was high in cortical layers II and IV, with characteristic small cells (NeuN in Figures 1.3A, 1.3C, 1.3D, and 1.3H). Large NeuN+ neurons were concentrated in layers III and V. A portion of these were large pyramidal neurons positive for SMI-32 (Figures 3A, 3E, and 3H). CB+, CR+, and PV+ cells also showed distinct distribution patterns along the cortical axis (Figures 1.3A and 1.3D), in agreement with previous studies (Defelipe et al. 1999; Leuba et al. 1998).

We next performed unbiased combinatorial expression profiling with the six cell-type specific proteins (GFAP, NeuN, SMI-32, CB, CR, PV). Among 63 possible combinations, 16 were found (Table S2). We identified sub-populations of CB+/CR+ and CB+/PV+ cells, but no CR+/PV+ or CB+/CR+/PV+, cells (Figures 1.3F, 1.3H, and 1.3I), in

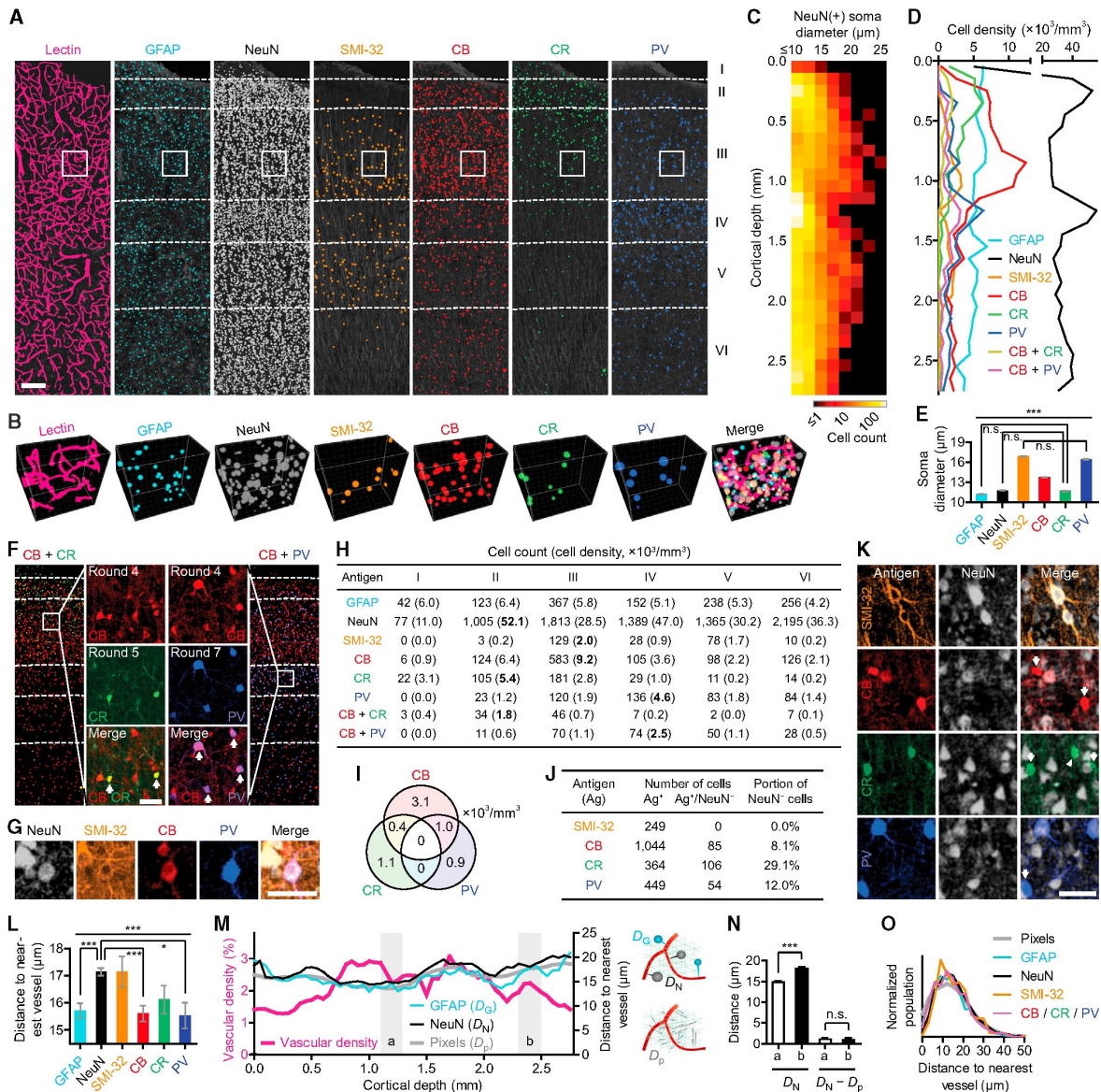


Figure 1.3: SWITCH Enables Proteomic Imaging and High-Dimensional Quantitative Phenotyping of Human Clinical Samples.

(A) ROI from Figure 1.2E showing semi-automatically detected locations and sizes of blood vessels (lectin) and diverse cell types (GFAP+, NeuN+, SMI-32+, CB+, CR+, PV+) in human visual cortex. The identified objects are overlaid on maximum intensity-projections of raw images of the corresponding channels (dark gray). Dashed lines divide cortical layers I-VI. (B) 3D rendering of the boxed region in (A) (200 μ m wide x 200 μ m high x 104 μ m deep) showing identified cells and blood vessels. (C) A heat map of the soma size distribution of NeuN+ cells, showing bimodal peaks at cortical layers III and V. (D) Density profiles of various cell types. (E) Comparison of cell sizes among different types of cells. One-way ANOVA was performed (**p < 0.001; N = 1,176, 7,835, 249, 1,044, 364 and 449 for each column). Post hoc tests were mostly p < 0.001 except for three non-significant (n.s.) cases. (F) Distribution of neurons expressing various subsets of calcium-binding proteins in the human visual cortex. Raw images in the middle columns show CB+/CR+ or CB+/PV+ neurons (arrows). (G) A representative NeuN+/SMI-32+/CB+/PV+ cell. (H) Cell counts and densities in different cortical layers. Cortical layers with the highest density for each neuronal channel are highlighted. (I) Cell densities for combinatorial co-expression of three interneuronal markers. (J) Statistics for NeuN- neurons. (K) Representative images showing NeuN-/CB+, NeuN-/CR+, and NeuN-/PV+ cells (arrows). The arrowhead indicates a CR+ cell with low NeuN immunoreactivity. (L) Comparison of cell-to-nearest vessel distances along cortical depth as measured from cell centroids to vascular boundaries. Post hoc tests following one-way ANOVA (p < 0.001; N = 935, 4,101, 210, 817, 265 and 331 for each column) were mostly n.s. except for three cases displayed. *p < 0.05. (M) Vascular density and distance-to-nearest vessel profiles of GFAP+ or NeuN+ cells along cortical depth. Mean distances from NeuN+ (D_N) and GFAP+ (D_G) cells and all extravascular pixels (D_p) are calculated and plotted. Diagrams illustrate the calculation of the three distances. (N) Cell-to-nearest vessel distances from NeuN+ cells in two regions—a (n = 570) and b (n = 445) in (M)—before (D_N) and after ($D_N - D_p$) correction. (O) Distribution profile of extravascular pixel- or cell-to-nearest vessel distances showing similar patterns. Three interneuronal markers are plotted together. Error bars are shown with mean \pm SEM. Scale bars, 200 μ m (A), 50 μ m (F, G, and K).

agreement with a previous report regarding mouse visual cortex (Gonchar et al. 2008). Interestingly, we observed that a significant portion of the CB, CR, and PV-positive neurons do not express detectable levels of NeuN, a widely used pan-neuronal marker (Figures 1.3J and 1.3K). In particular, a majority of CR+ cells showed very weak (Figure 1.3K, arrowhead) or no NeuN immunoreactivity (29.1%), whereas all SMI-32+ cells (Figures 1.3J and 1.3K) were NeuN positive. These results suggest that NeuN expression may be neuronal-type-specific in adult human visual association cortex. We also found a small number of CB+ cells and PV+ cells co-expressing SMI-32, a widely used pyramidal neuronal marker (Table S2) (Campbell & Morrison 1989). Five CB+/PV+ cells were identified as quadruple-positive (NeuN+/SMI-32+/CB+/PV+) cells (Figure 1.3G). All of the CB+ cells and PV+ cells co-expressing SMI-32 were localized in cortical layers III and IV. These results demonstrate the power of SWITCH as a tool for 3D proteomic profiling of intact biological samples at single-cell resolution.

Structural relationships between vasculature and brain cells have been a topic of interest in a broad range of basic and clinical research. Many previous studies obtained the cell-to-vessel distance from 2D images or small tissue volumes, which may hinder precise measurement of such 3D properties. Moreover, in many studies, separate measurements from different tissues needed to be compared without considering individual variabilities in local vasculature geometry. There has been no direct comparison of 3D cell-to-vessel distance among diverse cell types within the same intact tissue.

Using the proteomic imaging capability of SWITCH, for the first time, we were able to directly measure cell-to-vessel distances for six different cell types within a single intact tissue (Figures 1.3L–1.3O). As expected (McCaslin et al. 2011), GFAP+ astrocytes had a shorter mean distance than NeuN+ neurons (Figure 1.3L). CB+ and PV+ cells were also more closely localized near blood vessels than NeuN+ cells, but the difference was relatively small. Figure 3M shows that vascular density is not uniform along the cortex. However, the extravascular pixel-to-vessel distance (D_p), which we defined as a reference parameter to reflect the effect of the 3D vascular geometry (Figure 1.3M, right), did not show an inverse relationship with vascular density. This result may suggest that 3D vessel geometry is an important parameter to be considered in understanding a given vascular environment. In fact, cell-to-vessel distance profiles of many cell types closely followed the D_p profile (GFAP+, D_G , and NeuN+, D_N , shown in Figure 1.3M). In particular, when D_p was subtracted from cell-to-vessel distances (D_x) to cancel the influence of vascular geometric variation, $D_x - D_p$ turns out to be very consistent throughout cortical depth (Figure 1.3N). We further examined the distance distribution profiles for all cell types (Figure 1.3O). All profiles showed similar characteristic curves, which can be seen when objects are randomly located in a 3D space (Manzo et al. 2014). We could not observe any cell-type-specific distribution profile or bi- or multi-modal distribution pattern in this sample. Together, these data demonstrate that SWITCH can be used for high-dimensional quantitative phenotyping of human clinical samples.

1.3.4 SWITCH Enables Simple, Rapid, and Scalable Tissue-Clearing

To extend the multiplexed imaging capability of the SWITCH method to large systems, we developed a simple and rapid clearing method. We hypothesized that key steps in detergent-mediated lipid removal, such as permeation of SDS through membranes, might be strongly enhanced by increasing temperature (Keller et al. 2006), and SWITCH-processed samples may endure prolonged incubation at elevated temperatures. Indeed, thermal energy drastically increased the passive clearing speed of SWITCH-processed samples without noticeable tissue damage (Figure 1.4A). We achieved passive clearing of a whole adult mouse brain within 4 days at 80C (versus 4 weeks at 37C) (Figure 1.4C).

Upon prolonged exposure to high temperatures, however, samples developed a brownish hue (Friedman 1996), which may interfere with imaging at certain wavelengths (Figures 1.4B–1.4D and 1.4F). We found that reducing agents, such as sodium sulfite and 1-thioglycerol, effectively mitigate tissue browning during thermal clearing (Figures 1.4B–1.4D). Using thermal clearing with the reducing agents, we successfully cleared intact adult rat brains (2 weeks) as well as human (1 week) and marmoset samples (1 week), demonstrating the versatility and scalability of the method (Figures 1.4D and 1.4E).

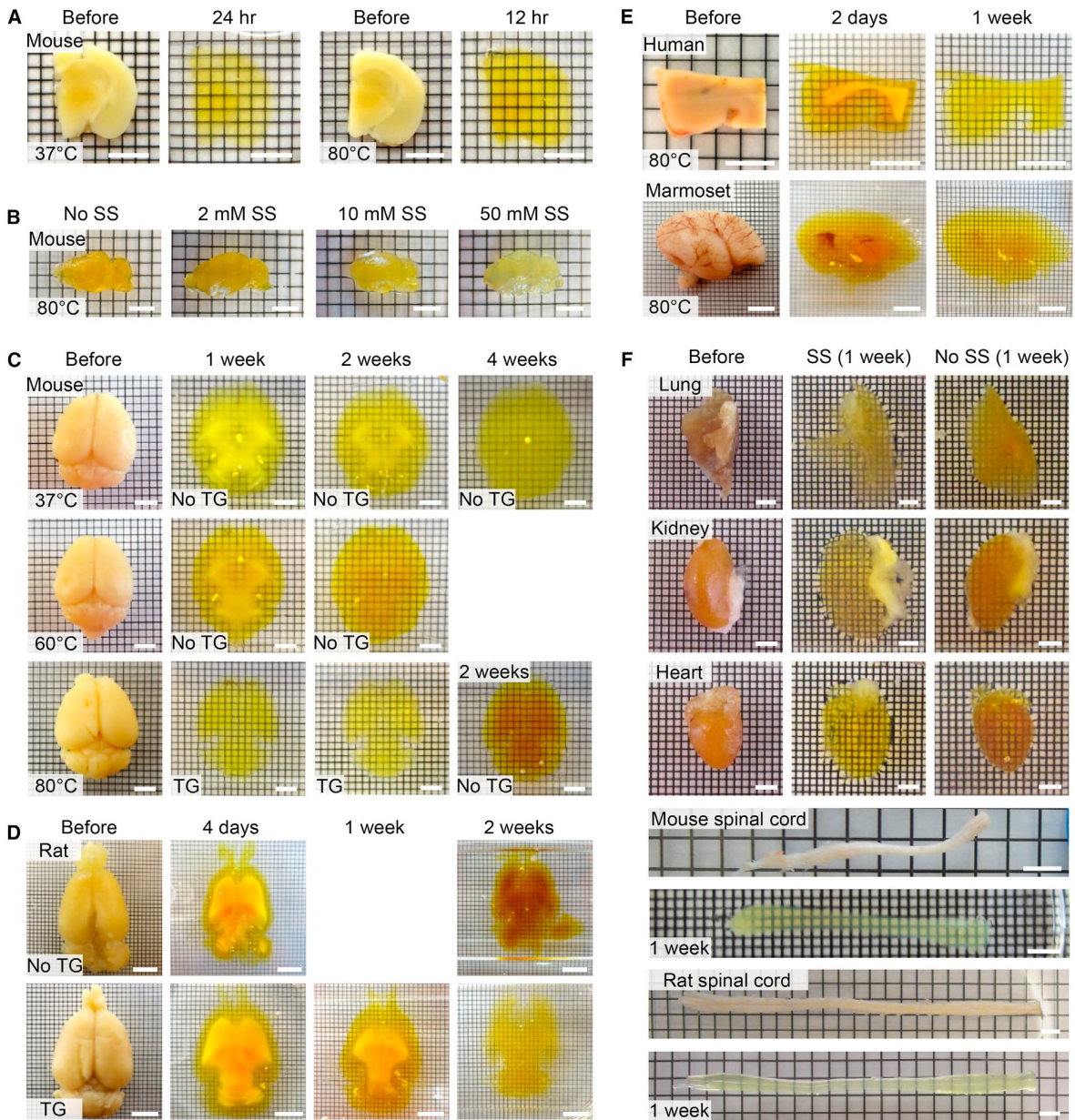


Figure 1.4: SWIITCH Enables Simple, Rapid, and Scalable Tissue Clearing. (A) Images of 1-mm coronal blocks of an adult mouse brain hemisphere before and after clearing at 37C for 24 hr or 80C for 12 hr. The lipid-extracted tissues were refractive index (RI)-matched (see SI for details). Scale bars, 3 mm. (B) Images of mouse brain hemispheres lipid-extracted at 80C for 10 days with 200 mM SDS containing 0–50 mM sodium sulfite (SS) as an anti-browning agent. Note that the tissues were not RI-matched. Scale bars, 6 mm. (C) Images of intact adult mouse brains cleared at 37C (top) and 60C (middle) and 80C (bottom) with and without 1-thioglycerol (TG). Browning in hightemperature clearing was effectively prevented by TG. Scale bars, 3 mm. (D) High-temperature (80C) clearing of whole rat brain with and without TG. Scale bars, 6 mm. (E) Clearing of human and marmoset samples at 80C. Scale bars, 6 mm. (F) Rapid clearing of various organs at 80C with and without 50 mM SS. Cleared rat spinal cord is not RI-matched. Scale bars, 3 mm.

Clearing of various rodent organs was also demonstrated with lung, kidney, heart, liver, and spinal cord (Figure 1.4F). The efficacy of sodium sulfite as an anti-browning agent was seen across all tissues.

1.3.5 SWITCH Enables Visualization and Quantitative Analysis of Entire Myelinated Fiber Tracts

We also sought to apply SWITCH to characterizing myelinated fiber pathways in the brain. Visualizing and analyzing neural fibers with high-resolution light microscopy can provide valuable insights into many studies (Thomas et al. 2014; Zuccaro & Arlotta 2013), such as validating diffusion tensor imaging (DTI) and understanding the organizing principles of brain connectivity. Furthermore, quantitative analysis of myelinated fibers in 3D may benefit clinical studies and development of novel treatments for many demyelinating diseases (Steinman 1999), such as multiple sclerosis and transverse myelitis. However, current methods for myelinated fiber visualization require either genetic labeling or a large amount of costly antibodies, limiting their utility to animal tissues or small clinical samples.

We discovered that a subset of lipids preserved in SWITCH-processed tissues (Hopwood 1972; Rozemond 1969) allows lipophilic dyes to selectively visualize lipid-rich membranes (Schlessinger et al. 1977). In particular, we found that long-chain dialkylcarbocyanines robustly stain myelinated axons (Figure 1.5A). However, when we attempted to label an intact tissue using conventional methods, we could not achieve dye penetration deeper than 100 μm because dye molecules were depleted as they rapidly associated with abundant targets in the outer layer (Figure 1.5C).

We hypothesized that SWITCH may enable rapid and uniform labeling of intact tissues by synchronizing the labeling reaction globally. We first screened a range of chemicals for controlling the binding kinetics of the lipophilic dye and discovered that 10 mM SDS effectively inhibits staining (Figure 1.5B). This result indicates that buffers containing 10 mM SDS might have a potential to be used as a “SWITCH-Off” buffer. Using an approach analogous to SWITCH-mediated GA fixation, we thought it might be possible to allow dye molecules to disperse uniformly throughout a sample in the SWITCH-Off buffer and then activate global probe-target binding with the SWITCH-On buffer (Figure 1.5D).

To test this approach, we first incubated a 1-mm-thick mouse brain block in PBST containing 10 mM SDS and lipophilic dyes for 24 hr at 37C (SWITCH-Off step). Then, we moved the tissue to PBST and incubated it for 3 hr at 37C (SWITCH-On step). The

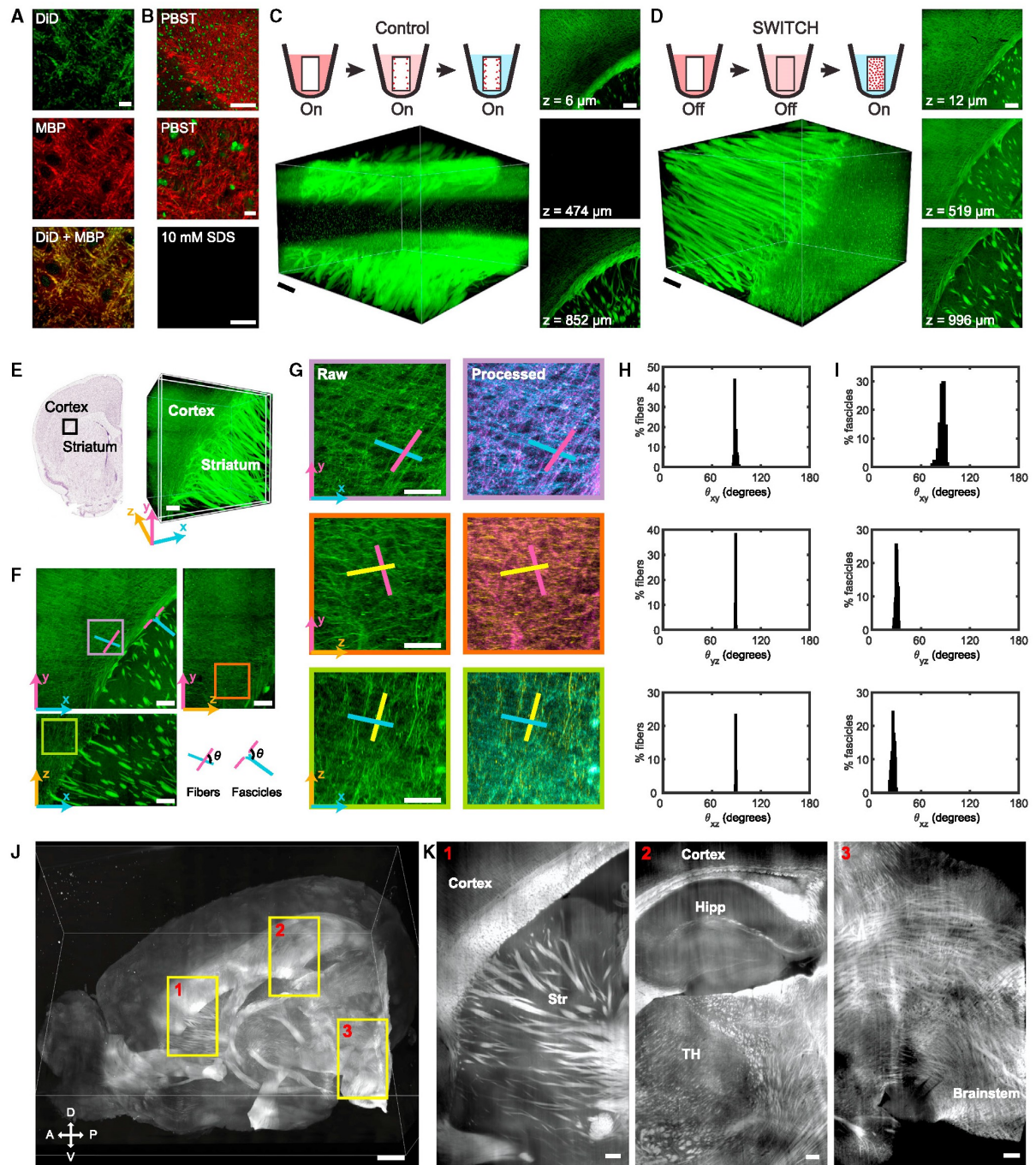


Figure 1.5: SWITCH Enables Visualization and Quantitative Analysis of Entire Myelinated Fiber Tracts.

(A) DiD and MBP staining on a SWITCH-processed mouse brain slice showing complete overlap between DiD and MBP. Scale bar, 10 μ m. (B) DiD staining with PBST or with PBS + 10 mM SDS buffer. DiD staining is completely inhibited in PBS + 10 mM SDS buffer. Green, syto16; red, DiD; scale bars, 100 μ m (top, bottom), 10 μ m (middle). (C) DiD staining of a 1-mm-thick mouse coronal block using PBST for 1.5 days at 37C. Only tissue surface is labeled. Scale bar, 200 μ m. (D) DiD staining of a 1-mm-thick mouse coronal block using SWITCH. The sample was first incubated in DiD, 10 mM SDS containing PBS buffer for 24 hr, then moved to PBST and incubated for 0.5 day at 37C. The whole sample is uniformly labeled. Scale bar, 200 μ m. (E) Volume image of a 1-mm-thick mouse brain coronal slice stained with DiD to visualize myelinated tracts acquired using a confocal microscope. The volume contains both the striatum and the cortex. Scale bar, 200 μ m. (F) Maximum intensity projection of the subvolume (illustrated in white in the volume image in (E)) shows fascicles from the striatum diverging at the corpus callosum and fibers near that area in the cortex forming a grid pattern. Scale bar, 200 μ m. (G) Enlarged images of the selected regions of interest in (F) shows the fibers in the cortex arranged in a grid pattern. Fibers are colorized based on orientation. Scale bar, 100 μ m. (H) Analysis of all the fibers in the entire volume shows that most fibers make an 89° intersection in xy and yz and an 88° intersection in xz. (I) Analysis of all the fascicles in the entire volume shows that they make an 87° turn in xy, a 26° turn in yz, and a 30° turn in xz. (J) Volume image of a mouse brain hemisphere stained with DiD to visualize myelinated tracts acquired using a custom-built light-sheet microscope. Scale bar, 1 mm. (K) Representative images showing individual fibers and fascicles in three different brain regions in (J). Str, striatum; Hipp, hippocampus; TH, thalamus. Scale bars, 200 μ m.

result was strikingly uniform labeling of all the myelinated axons within the sample (Figure 1.5D). Myelinated fibers were clearly visible throughout the depth while the control tissue showed signal only from the surface (Figure 1.5C).

We leveraged this fiber visualization capability to investigate how fibers and fascicles are organized in a mouse brain. Previous research has shown that fibers may be organized in 3D grids (Wedge et al. 2012). However, the structure of all of the individual fibers has not yet been studied at the microscopic resolutions and macroscopic scales necessary to visualize their 3D organization. To that end, we obtained a volume image of labeled myelinated fibers in a SWITCH-processed mouse brain coronal slice spanning from the cortex to the striatum (Figure 1.5E; Movies S2 and S3). This volume shows three main orientations of the fibers organized in a cubic grid: one radially projecting from the corpus callosum and two parallel to the corpus callosum. These three orientations are all orthogonal to one another (Figure 1.5F; Movie S3). The volume also shows fascicles that radiate from the striatum and diverge, almost at right angles, at the corpus callosum (Figure 1.5E; Movie S3). To quantify this finding in an unbiased manner, we determined the orientation of each of the fibers present in the volume and calculated the angles at which these fibers would intersect (Figure 1.5G). In all three dimensions, the fibers indeed oriented themselves approximately orthogonally to each other (Figure 1.5H). We used a similar approach to examine the fascicle orientations and found that they diverge almost orthogonally with respect to the corpus callosum in one of the axes (Figure 1.5I). These results are corroborated by the autocorrelation results (Figure S3 and S4). This finding was made possible by the high-resolution and large-volume visualization capability of our method. A low-resolution approach would overlook the individual fibers while a low-volume approach would be unable to capture the entire connectional anatomy.

We then tested whether this application of SWITCH could be scaled to larger tissues. We applied the SWITCH approach for labeling an intact mouse hemisphere, but with 4 days of incubation in PBST containing 10 mM SDS and lipophilic dyes (SWITCH-Off step) and 1 day in PBST (SWITCH-On step). We imaged this larger volume using a custom-built, high-speed light-sheet microscope (Tomer et al. 2012; Tomer et al. 2014) within 2 hr and observed uniform labeling of all myelinated fibers across the entire tissue (Figure 1.5J; Movie S4). As demonstrated, the SWITCH-labeling approach is scalable to organ-scale tissues. Just by scaling the incubation time with respect to the tissue size, we were able to label the whole tissue. The cost of the dye molecules used for labeling the hemisphere was less than one dollar. We also demonstrated that this approach can be used for visualizing myelinated fibers in spinal cords (Movie S5). These results show that the SWITCH-labeling method can be used to uniformly label tissues ranging from a 1-mm-thick block to an entire hemisphere for quantitative analysis.

1.3.6 SWITCH Enables Scalable and Uniform Antibody Labeling

We then asked whether SWITCH-mediated labeling could be applied to the use of antibodies. We hypothesized that SDS could again be used as an effective inhibitor of antibody-antigen binding in small concentrations. Indeed, when we assayed for antibody labeling at various concentrations of SDS, we found that 0.5 to 1.0 mM was a high enough concentration to inhibit binding for many antibodies (Figure 1.6A).

Based on the results of our binding assay, we chose PBS containing 0.5 mM SDS as a SWITCH-Off buffer and PBST as a SWITCH-On buffer. We hypothesized that, because very little antibody-antigen binding is occurring in the SWITCH-Off condition, antibodies would effectively be able to diffuse to equilibrium throughout the sample more rapidly than in PBST, in which antibodies are rapidly depleted at the surface (Figure 1.6B). To test this, we attempted to label 1-mm-thick mouse brain blocks using anti-histone H3 antibodies. We labeled one sample using a 12 hr SWITCH-Off/12 hr SWITCH-On cycle and another using a standard immunohistochemistry protocol with 12 hr of primary antibody incubation in PBST followed by a 12 hr wash. For the SWITCH-On step, antibodies were not added to PBST. The result was a large increase in penetration depth and overall signal uniformity in the SWITCH sample relative to the control (Figures 1.6B and 1.6C; Movie S6).

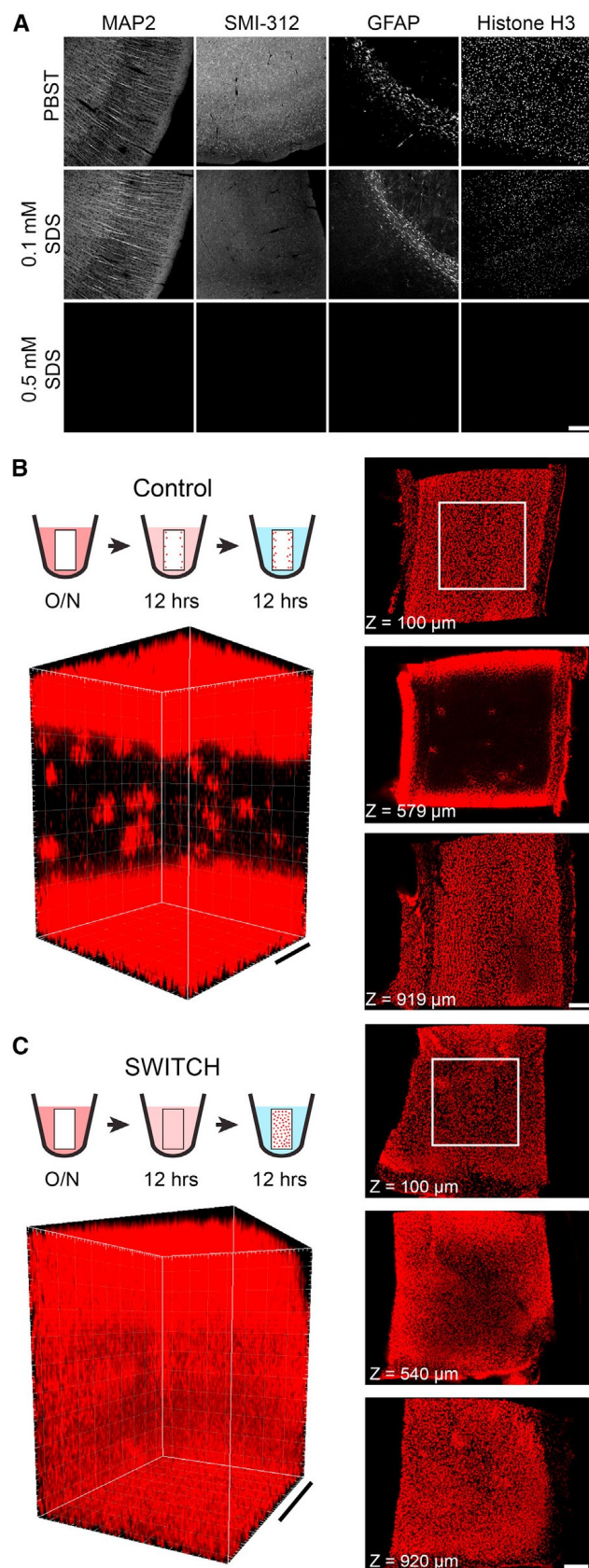


Figure 1.6: SWITCH Increases Uniformity of Antibody Labeling in Thick Tissues.

(A) Antibody staining of cleared 100- μ m mouse brain sections in PBST and various concentrations of SDS in PBS. SDS effectively inhibits antibody-antigen binding in a concentration-dependent manner. Scale bar, 200 μ m. (B and C) Histone H3 staining of 1-mm-thick mouse cerebral cortex blocks in PBST (B) and using SWITCH (C). Control sample was incubated in antibody-containing PBST for 12 hr then washed for 12 hr. SWITCH sample was incubated in antibody-containing SWITCH-Off solution for 12 hr then washed in SWITCH-On solution for 12 hr. Sections from the top, middle, and bottom of the blocks are shown. 3D renderings were generated from the ROIs shown. SWITCH sample showed vast increase in uniformity of labeling compared to control. Scale bars, 150 μ m (B, left), 200 μ m (others).

1.4 Discussion

We have developed SWITCH, a simple method that enables scalable proteomic imaging of intact systems without requiring any specialized equipment or reagents. SWITCH is complementary to many pioneering technologies, each of which has its own unique advantages. For example, matrix-assisted laser desorption ionization mass spectrometry (MALDI-MS) and laser-ablation inductively coupled plasma mass spectrometry (LA-ICP-MS) allow visualization of a large subset of proteins and other biomolecules without a priori knowledge of targets. Recent advances in imaging mass spectrometry combined with immunohistochemistry (IHC) have significantly improved resolution (Angelo et al. 2014; Giesen et al. 2014), which was limited in MALDI-MS and LA-ICP-MS. This approach remarkably demonstrated analysis of more than 100 targets at subcellular resolution.

Multiplexing strategies for IHC that rely on iterative staining and elution have been developed. Among several pioneering techniques is array tomography, which involves cutting a tissue sample into tens or hundreds of nanometer-thick sections for staining and imaging (Micheva et al. 2010). These sections can be repeatedly washed and stained for probing different proteins. This powerful method yields subcellular resolution images of a small volume of tissue with fairly high multiplexing capability. Although these advanced technologies enable new approaches in studying complex biological systems, these methods require specialized equipment and are, therefore, difficult to implement in most labs.

With the aim of developing a simple and scalable method for proteomic imaging of both large animal and human samples, we first needed to devise the SWITCH method for controlling a broad range of chemical reactions in tissue processing to achieve uniform sample treatment regardless of tissue size and type. SWITCH dynamically modulates chemical reaction kinetics to synchronize the reaction time between molecules throughout the system. This strategy enables all endogenous molecular targets in a large intact tissue to experience similar reaction conditions (time and concentration). As a result, large tissues can be uniformly processed.

The SWITCH approach takes advantage of the way certain chemicals can be reversibly and rapidly changed by simply modulating their surrounding environment. For instance,

in the GA-tissue-gelling step, we were able to decrease the rate of GA-biomolecule crosslinking by two orders of magnitude by using pH 3 buffer, because primary amine groups in endogenous biomolecules are protonated at low pH and the resulting charged amine cannot react with GA (Hopwood 1967). This pH-dependent reactivity means that after uniformly dispersing GA in a tissue at low pH, we can “switch-on” inactivated amine groups by changing the amine’s surrounding environment to a neutral-pH buffer. At neutral pH, charged amine groups are rapidly deprotonated and become reactive. In the case of human samples or animal samples that were previously PFA-fixed for a different purpose, this simple strategy enables all the endogenous biomolecules in a large intact tissue to simultaneously experience similar GA-fixation/gelling condition. PFA-fixed tissues can withstand treatment at low pH while GA molecules are introduced. In the case of non-fixed samples, we recommend that they first be fixed with PFA before exposure to acidic conditions. If perfusion is possible, it is the recommended method of sample preservation.

Uniform GA-tissue-gel formation is a crucial first step toward our goal. Fixation of large samples via traditional immersion is unlikely to uniformly preserve them because highly reactive GA molecules are depleted within the outer layers of a sample. This presents a significant problem for iterative staining-based methods that rely on the removal of imaged probes using harsh elution conditions, because non-uniform preservation results in non-uniform loss of structure and molecules throughout the process. As demonstrated, our pH-SWITCH strategy ensures exceptionally uniform preservation of biological tissues that cannot be perfused (e.g., banked human clinical samples), meeting the requirements of proteomic imaging and quantitative phenotyping.

It has been noted that fixation with GA results in an increase in broad spectrum autofluorescence. While this autofluorescence has been low enough to allow quantitative analysis, it could be problematic in visualizing targets with low copy number. We investigated the use of sodium borohydride as a method of reducing autofluorescence, but found that the tissue damage resulting from this incubation procedure offset any benefits obtained from the modest decrease in autofluorescence that we were able to observe (Figure S5).

The use of reducing agents has allowed us to eliminate the issue of tissue browning during high-temperature clearing, but we also observed that excessive use of these chemicals may cause gradual tissue weakening. This is likely due to the reduction of disulfide linkages that maintain the tertiary structure of proteins within a sample, resulting in increased protein denaturation. Protein denaturation may lead to reduced sample antigenicity, but we have not found this to be an issue when using conservative amounts of reducing agents. Additionally, due to the instability of mRNA at elevated temperatures, this method of rapid clearing is not compatible with methods that require the preservation of mRNA

(Figure S6).

Multiplexed imaging requires software to warp each experiment into a common coordinate system despite the subtle physical differences between each staining round. Variance can come in the form of rigid body changes (rotation, translation, and scale), illumination artifacts, stain quality, and tissue degradation. We observed that a feature-based algorithm gives maximum robustness across these sources of variance at the cost of increased computational requirements—a reasonable trade given the declining costs of such resources. To simplify the process, gross rigid alignments (i.e., rotating the tissue 180 degrees) are still best handled by human eye before the data are passed to the algorithm to achieve the cellular-scale registration.

SWITCH can provide a reliable way to obtain integrated high-dimensional information from intact biological samples. Using the cross-talk-free dataset, we successfully performed non-biased combinatorial expression analysis of a single human clinical tissue to unequivocally identify diverse cell-types based on their distinct protein expression patterns. Our quantitative analysis shows that CR+/PV+ cells do not exist within the examined volume of the human V2 cortex. The same finding was reported in mouse visual cortex (Gonchar et al. 2008), but such co-expression patterns among calcium-binding proteins may differ among brain regions and between individuals and species (Anelli & Heckman 2006), which, therefore, calls for more comprehensive large-scale investigation.

We observed many NeuN-negative interneurons. NeuN, a neuron-specific RNA-binding protein known as Rbfox3 protein (Kim et al. 2009), has been widely used as a pan-neuronal marker for statistical analysis of many types of mature neurons (Baleriola et al. 2014; Pickrell et al. 2015). Only a few types of neurons are exceptions, such as cerebellar Purkinje cells, olfactory bulb mitral cells, and retinal photoreceptor cells (Mullen et al. 1992). However, even though we applied strict criteria to prevent weak NeuN+ cells from being identified as NeuN- cells, substantial portions of CB+, CR+, and PV+ neurons were still NeuN- while all SMI+ neurons were NeuN+. This result is supported by a recent report that some CR+ are not NeuN+, and CR and NeuN immunoreactivities have a negative correlation in the avian brainstem (Bloom et al. 2014). Likewise, in our experiments on human visual association cortex, cells with strong immunoreactivity against calcium-binding protein markers were frequently negative or very weakly positive for NeuN. These findings, together with a series of exceptional reports such as those on NeuN+ cultured astrocytes (Darlington et al. 2008) and GFAP+ neuron-like cells (Oka et al. 2015), indicate that classical cell-type markers, particularly NeuN, may need to be used more carefully in light of their selectivity and function.

The SWITCH method has the potential to modulate a wide range of probe-target binding reactions. Probe-target interactions are governed by a multiplicity of non-covalent bonds

such as hydrogen bonds, electrostatic forces, van der Waals bonds, and hydrophobic interactions (Mian et al. 1991). These weak forces can be effectively controlled by changing the surrounding chemical environment (e.g., ionic strength, pH, chemical additive, and temperature) (Kamata et al. 1996). For instance, we discovered that the addition of SDS alone, in different concentrations, can completely inhibit lipophilic dye-target and antibody-antigen binding reactions.

The SWITCH method's unique uniform-labeling capability enables quantitative analysis of large tissues that was previously only possible for thin tissue sections. Quantitative analysis relies heavily on signal intensity and SNR. Non-uniform or heterogeneous labeling would prohibit or, even worse, bias the analysis. While post hoc image processing methods could correct for small gradients in labeling (or imaging), large gradients caused by non-uniform labeling, where the surface of the tissue is saturated while the core is mostly unlabeled, would preclude image recovery. If the labeling is heterogeneous, the resulting data would be heavily biased, and no image processing methods could salvage such data in a fair way. This is why quantitative analysis of non-uniformly labeled tissues is a great challenge. However, tissues labeled using SWITCH exhibit uniform signal intensity and SNR throughout the tissue. Such a clear dataset lends itself well to quantitative analysis.

Although SWITCH enables processing of large samples, the speed of labeling is still fundamentally limited by passive diffusion. This is not of concern for smaller samples or even single-round investigation of large samples, but multiplexed imaging of large samples becomes impractical as a result, potentially taking months or years to collect the range of desired data. Recently developed methods of stochastic electrotransport (S.-Y. Kim et al. 2015) could potentially be combined with SWITCH to facilitate these experiments.

Together with its simplicity, scalability, and broad applicability, our data suggest that SWITCH provides access to high-dimensional multi-scale information that may help to understand health and disease from molecules to cells to entire systems.

1.5 Experimental Procedures

1.5.1 Mice

Young adult male and female C57BL/6 and Thy1-eGFP-M mice were housed in a reverse 12 hr light/dark cycle with unrestricted access to food and water. All experimental protocols were approved by the MIT Institutional Animal Care and Use Committee and Division of Comparative Medicine and were in accordance with guidelines from the National Institute of NIH.

1.5.2 SWITCH-Mediated Tissue Preservation

PFA-fixed human samples were washed in a solution consisting of 50% PBS titrated to pH 3 using HCl, 25% 0.1 M HCl, and 25% 0.1 M potassium hydrogenphthalate (KHP). This wash solution was then replaced with fresh solution with the addition of 4%–10% GA. The samples were then incubated in this pH 3 solution at 4C for 2 days with gentle shaking. The solution was then replaced with PBS with the addition of 1%–4% GA and the sample was again allowed to incubate for 2 days at 4C and 2–7 hr at 37C with gentle shaking. The sample was then washed in PBS at room temperature (RT) for 1 day with gentle shaking. After washing, reactive GA within the sample was inactivated by incubation in a solution consisting of 4% glycine and 4% acetamide for 1 day at 37C with gentle shaking. Finally, the sample was washed for 1 day in PBS at RT with gentle shaking.

1.5.3 Passive Clearing with Thermal Energy

Aqueous clearing solution containing 200 mM SDS, 10 mM lithium hydroxide, 40 mM boric acid, and a variable amount of anti-browning agent (i.e., 0–50 mM sodium sulfite or 0%–0.5% w/v 1-thioglycerol) was titrated to pH 9 using sodium hydroxide before use. Samples were incubated at 60–80C until clear using Easy-Passive (EP-1001; Live Cell Instrument) or a water bath.

1.5.4 Sample Delabeling

Imaged samples were delabeled in clearing solution at 60–80C (elution condition) for 1–2 days for large samples and O/N for thin samples.

1.5.5 SWITCH-Mediated Fluorescent Labeling

Samples were incubated in SWITCH-Off solution (0.5 or 10 mM SDS in PBS) O/N with gentle shaking at 37C and transferred to a fresh volume of SWITCH-Off solution (containing molecular probes) just enough to cover the sample. Samples were incubated at 37C with gentle shaking and times were scaled with sample size. Samples were then transferred to a large volume of PBST (SWITCH-On) and incubated at 37C with gentle shaking.

1.6 Supplemental Information

Supplemental Information includes Supplemental Experimental Procedures, six figures, two tables, and six movies and can be found with this article online at <http://dx.doi.org/10.1016/j.cell.2015.11.025> as well as in the appendix.

1.7 Author Contributions

K.C. conceived the SWITCH idea. E.M., J.H.C, D.G., T.K., J.S., and K.C. designed the experiments. E.M. designed and performed multiplexed staining and imaging experiments. D.G. and H.S.S. developed and implemented the registration algorithm. T.K. performed all analysis related to the human visual cortex sample with input from K.C., M.P.F., and H.S.S. J.H.C. performed all analysis related to DiD datasets. E.M., N.B., and S.-Y.K. performed antibody compatibility testing. E.M., J.H.C, N.B., A.H., and J.S. performed testing of cross-linked protein gels with various fixatives. E.M. performed protein loss and structural preservation experiments. E.M., J.S., and N.B. designed and performed experiments relating to thermal clearing and use of anti-browning agents. E.M. and M.M. performed DiD staining experiments. E.M. and Y.-G.P. performed antibody SWITCH experiments. H.C. designed and built the light-sheet microscope, and J.H.C. developed the software. J.-Y.P. provided spinal cord samples. Y.-G.P. performed mRNA experiments. M.P.F. provided human samples. H.S.S., V.J.W., and M.P.F. provided helpful discussion regarding the manuscript. S.V. provided experimental support. E.M., J.H.C., D.G., T.K., J.S., S.-Y.K., V.J.W., and K.C. wrote the manuscript. K.C. supervised all aspects of the work.

1.8 Acknowledgments

We thank the entire Chung laboratory for support and helpful discussions. S.-Y.K. was supported by the Simons Postdoctoral Fellowship and the Life Sciences Research Foundation. K.C. was supported by Burroughs Wellcome Fund Career Awards at the Scientific Interface, the Searle Scholars Program, the Michael J. Fox Foundation, DARPA, the JPB Foundation (PIIF and PNDRF), and NIH (1-U01-NS090473-01). M.P.F. was supported in part by the Massachusetts Alzheimer Disease Research Center (5 P50 AG005134). Resources that may help enable general users to establish the methodology are freely available online. (www.chunglabresources.org).

Received: August 31, 2015

Revised: October 9, 2015

Accepted: November 10, 2015

Published: December 3, 2015

1.9 References

- Alivisatos, A.P. et al., 2013. The brain activity map. *Science*, 339(6125), pp.1284–1285.
- Anelli, R. & Heckman, C.J., 2006. The calcium binding proteins calbindin, parvalbumin, and calretinin have specific patterns of expression in the gray matter of cat spinal cord. *Journal of Neurocytology*, 34(6), pp.369–385.
- Angelo, M. et al., 2014. Multiplexed ion beam imaging of human breast tumors. *Nature Medicine*, 20(4), pp.436–442. Available at: <http://dx.doi.org/10.1038/nm.3488>.
- Baleriola, J. et al., 2014. Axonally synthesized ATF4 transmits a neurodegenerative signal across brain regions. *Cell*, 158(5), pp.1159–1172. Available at: <http://dx.doi.org/10.1016/j.cell.2014.07.001>.
- Bloom, S., Williams, A. & MacLeod, K.M., 2014. Heterogeneous calretinin expression in the avian cochlear nucleus angularis. *JARO - Journal of the Association for Research in Otolaryngology*, 15(4), pp.603–620.
- Campbell, M.J. & Morrison, J.H., 1989. Monoclonal antibody to neurofilament protein (SMI-32) labels a subpopulation of pyramidal neurons in the human and monkey neocortex. *Journal of Comparative Neurology*, 282(2), pp.191–205.
- Chung, K. & Deisseroth, K., 2013. CLARITY for mapping the nervous system. *Nature methods*, 10(6), pp.508–13. Available at: <http://www.ncbi.nlm.nih.gov/pubmed/23722210>.
- Chung, K. et al., 2013. Structural and molecular interrogation of intact biological systems. *Nature*, 497(7449), pp.332–337. Available at: <http://www.nature.com/doifinder/10.1038/nature12107>.
- Darlington, P.J. et al., 2008. Widespread immunoreactivity for neuronal nuclei in cultured human and rodent astrocytes. *Journal of Neurochemistry*, 104(5), pp.1201–1209.
- Defelipe, J. et al., 1999. Distribution and patterns of connectivity of interneurons containing calbindin, calretinin, and parvalbumin in visual areas of the occipital and temporal lobes of the macaque monkey. *Journal of Comparative Neurology*, 412(3), pp.515–526.
- De Sousa, A.A. et al., 2010. Comparative cytoarchitectural analyses of striate and extrastriate areas in hominoids. *Cerebral Cortex*, 20(4), pp.966–981.
- Friedman, M., 1996. Food browning and its prevention: An overview. *Journal of Agricultural and Food Chemistry*, 44(3).
- Giesen, C. et al., 2014. Highly multiplexed imaging of tumor tissues with subcellular

resolution by mass cytometry. *Nature Methods*, 11(4), pp.417–422.

Gonchar, Y., Wang, Q. & Burkhalter, A., 2008. Multiple distinct subtypes of GABAergic neurons in mouse visual cortex identified by triple immunostaining. *Frontiers in Neuroanatomy*, 1(3).

Hopwood, D., 1967. Some aspects of fixation with glutaraldehyde. A biochemical and histochemical comparison of the effects of formaldehyde and glutaraldehyde fixation on various enzymes and glycogen, with a note on penetration of glutaraldehyde into liver. *Journal of anatomy*, 101(Pt 1), pp.83–92. Available at: <http://www.ncbi.nlm.nih.gov/pubmed/6047703>.

Hopwood, D., 1972. Theoretical and practical aspects of glutaraldehyde fixation. *The Histochemical Journal*, 4(4), pp.267–303.

Hopwood, D., 1970. The reactions between formaldehyde, glutaraldehyde and osmium tetroxide, and their fixation effects on bovine serum albumin and on tissue blocks. *Histochemistry*, 24(1), pp.50–64.

Kamata, N. et al., 1996. Comparison of pH and ionic strength dependence of interactions between monoclonal antibodies and bovine β -lactoglobulin. *Bioscience, Biotechnology and Biochemistry*, 60(1), pp.25–29.

Kasthuri, N. et al., 2015. Saturated Reconstruction of a Volume of Neocortex. *Cell*, 162(3), pp.648–661.

Keller, S., Heerklotz, H. & Blume, A., 2006. Monitoring lipid membrane translocation of sodium dodecyl sulfate by isothermal titration calorimetry. *Journal of the American Chemical Society*, 128(4), pp.1279–1286.

Kim, K.K., Adelstein, R.S. & Kawamoto, S., 2009. Identification of neuronal nuclei (NeuN) as Fox-3, a new member of the Fox-1 gene family of splicing factors. *Journal of Biological Chemistry*, 284(45), pp.31052–31061.

Kim, S.-Y. et al., 2015. Stochastic electrotransport selectively enhances the transport of highly electromobile molecules. *Proceedings of the National Academy of Sciences*, 112(46), pp.E6274–E6283. Available at: <http://www.pnas.org/lookup/doi/10.1073/pnas.1510133112>.

Leuba, G., Kraftsik, R. & Saini, K., 1998. Quantitative distribution of parvalbumin, calretinin, and calbindin D- 28k immunoreactive neurons in the visual cortex of normal and Alzheimer cases. *Experimental Neurology*, 152(2), pp.278–291.

Manzo, C. et al., 2014. PSF decomposition of nanoscopy images via Bayesian analy-

sis unravels distinct molecular organization of the cell membrane. *Scientific Reports*, 4(April).

McCaslin, A.F.H. et al., 2011. In vivo 3D morphology of astrocyte-vasculature interactions in the somatosensory cortex: Implications for neurovascular coupling. *Journal of Cerebral Blood Flow and Metabolism*, 31(3), pp.795–806.

Mian, I.S., Bradwell, A.R. & Olson, A.J., 1991. Structure, function and properties of antibody binding sites. *Journal of Molecular Biology*, 217(1), pp.133–151.

Micheva, K.D. et al., 2010. Single-synapse analysis of a diverse synapse population: Proteomic imaging methods and markers. *Neuron*, 68(4), pp.639–653. Available at: <http://dx.doi.org/10.1016/j.neuron.2010.09.024>.

Mullen, R.J., Buck, C.R. & Smith, A.M., 1992. NeuN, a neuronal specific nuclear protein in vertebrates. *Development*, 116(1), pp.201–211.

Oka, Y., Ye, M. & Zuker, C.S., 2015. Thirst driving and suppressing signals encoded by distinct neural populations in the brain. *Nature*, 520(7547), pp.349–352.

Pickrell, A.M. et al., 2015. Endogenous Parkin Preserves Dopaminergic Substantia Nigra Neurons following Mitochondrial DNA Mutagenic Stress. *Neuron*, 87(2), pp.371–381. Available at: <http://dx.doi.org/10.1016/j.neuron.2015.06.034>.

Rah, J.C. et al., 2013. Thalamocortical input onto layer 5 pyramidal neurons measured using quantitative large-scale array tomography. *Frontiers in Neural Circuits*, 7(NOV), pp.1–16.

Renier, N. et al., 2014. iDISCO: A simple, rapid method to immunolabel large tissue samples for volume imaging. *Cell*, 159(4), pp.896–910. Available at: <http://dx.doi.org/10.1016/j.cell.2014.10.010>.

Richardson, D.S. & Lichtman, J.W., 2015. Clarifying Tissue Clearing. *Cell*, 162(2), pp.246–257.

Roozemond, C., 1969. The effect of fixation with formaldehyde and glutaraldehyde on the composition of phospholipids extractable from rat hypothalamus., 17(7).

Schlessinger, J. et al., 1977. Lateral transport of a lipid probe and labeled proteins on a cell membrane. *Science*, 195(4275), pp.307–309.

Steinman, L., 1999. Assessment of animal models for MS and demyelinating disease in the design of rational therapy. *Neuron*, 24(3), pp.511–514.

Sung, H.W. et al., 1996. Cross-linking characteristics of biological tissues fixed with

monofunctional or multifunctional epoxy compounds. *Biomaterials*, 17(14), pp.1405–1410.

Susaki, E.A. et al., 2014. Whole-brain imaging with single-cell resolution using chemical cocktails and computational analysis. *Cell*, 157(3), pp.726–739. Available at: <http://dx.doi.org/10.1016/j.cell.2014.03.042>.

Thomas, C. et al., 2014. Anatomical accuracy of brain connections derived from diffusion MRI tractography is inherently limited. *Proceedings of the National Academy of Sciences of the United States of America*, 111(46), pp.16574–16579.

Tomer, R. et al., 2012. Quantitative high-speed imaging of entire developing embryos with simultaneous multiview light-sheet microscopy. *Nature Methods*, 9(7), pp.755–763. Available at: <http://dx.doi.org/10.1038/nmeth.2062>.

Tomer, R. et al., 2014. Advanced CLARITY for rapid and high-resolution imaging of intact tissues. *Nature Protocols*, 9(7), pp.1682–1697.

Wedgeen, V.J. et al., 2012. The Geometric Structure of the Brain Fiber Pathways. *Science*, 335(March), pp.1628–1634.

Yuste, R., 2015. From the neuron doctrine to neural networks. *Nature Reviews Neuroscience*, 16(8), pp.487–497. Available at: <http://dx.doi.org/10.1038/nrn3962>.

Zuccaro, E. & Arlotta, P., 2013. The quest for myelin in the adult brain. *Nature Cell Biology*, 15(6), pp.572–575. Available at: <http://dx.doi.org/10.1038/ncb2750>.

Chapter 2

Multiplexed and scalable super-resolution imaging of three-dimensional protein localization in size-adjustable tissues

Taeyun Ku*, **Justin Swaney***, Jeong-Yoon Park*, Alexander Albanese, Evan Murray, Jae Hun Cho, Young-Gyun Park, Vamsi Mangena, Jiapei Chen, and Kwanghun Chung¹

2.1 Summary

The biology of multicellular organisms is coordinated across multiple size scales, from the subnanoscale of molecules to the macroscale, tissue-wide interconnectivity of cell populations. Here we introduce a method for super-resolution imaging of the multiscale organization of intact tissues. The method, called magnified analysis of the proteome (MAP), linearly expands entire organs fourfold while preserving their overall architecture and three-dimensional proteome organization. MAP is based on the observation that preventing crosslinking within and between endogenous proteins during hydrogel-tissue hybridization allows for natural expansion upon protein denaturation and dissociation. The expanded tissue preserves its protein content, its fine subcellular details, and its organ-scale intercellular connectivity. We use off-the-shelf antibodies for multiple rounds of immunolabeling and imaging of a tissue's magnified proteome, and our experiments demonstrate a success rate of 82% (100/122 antibodies tested). We show that specimen size can be reversibly modulated to image both inter-regional connections and fine

¹* indicates co-first authorship.

synaptic architectures in the mouse brain.

2.2 Introduction

Biological systems such as the mammalian brain consist of thousands of distinct cell types forming highly interconnected functional networks (White et al. 1986; DeFelipe 2010; Helmstaedter 2013; Craddock et al. 2013; Oh et al. 2014). Understanding how these diverse cells interact to generate system-level responses is essential for many fields of biology. Deciphering these complex interactions requires tools that can simultaneously characterize the molecular identity and fine sub-cellular architectures of individual cells as well as their system-level connectivity, because these properties together determine many cell functions. To date, technologies provide only a subset of the required multilevel information.

Proteomic imaging techniques can potentially provide multilevel information in both animals and human samples (Phizicky et al. 2003; Hanash 2004; Agato et al. 2004; Berglund et al. 2008; Uhlen et al. 2010). The proteome is an ideal substrate for the integrated analysis of functional components owing to proteins' unmatched diversity, functional roles, and distinct subcellular localization at single-molecule precision. The existing large antibody libraries (close to 100,000 antibodies), once rigorously validated, could enable the detection of more than 70% of the human proteome and corresponding cellular architectures (Uhlen, M et al 2010).

For example, multiplexed proteomic imaging techniques (e.g., array tomography and SWITCH) can provide molecular details for individual cells and may allow reconstruction of their surrounding tissue environment (Micheva & Smith 2007; Kay et al. 2013; Murray et al. 2015). Emerging intact tissue clearing approaches preserve proteins and the continuity of neural fibers, which may enable reconstruction of immunolabeled neural architectures (Dodd et al. 2007; Richardson & Lichtman 2015). Super-resolution imaging of immunolabeled thin tissue sections has been successfully used to characterize minute subcellular structures (e.g., synapses) (Rust et al. 2006; Betzig et al. 2006; Hess et al. 2006; Maglione & Sigrist 2013). In addition to conventional super-resolution approaches, Chen et al. (2015) have recently demonstrated that protease digestion of a hydrogel-tissue hybrid homogenizes its mechanical characteristics and allows approximately fourfold linear expansion of the hybrid. Using this approach, termed expansion microscopy (ExM), they demonstrated super-resolution imaging of thin tissue sections with custom-made antibody probes and diffraction-limited microscopes (Chen et al. 2015).

Despite the success of these new technologies, integrated reconstruction of the fine subcel-

lular architectures, molecular details, and intercellular connectivity of diverse cell types in large-scale biological systems remains an unmet goal in biology. For instance, the protease digestion step in ExM causes a loss of proteins, which limits the number of protein structures that can be imaged in the same sample. In addition, intercellular connectivity is largely lost in ExM as it requires tissue sectioning to allow immunolabeling of an unprocessed tissue with limited permeability. By contrast, emerging whole-tissue clearing methods preserve neural connectivity and endogenous proteins, but accurate reconstruction of neural architectures remains challenging owing to the low resolution of diffraction-limited microscopy.

Here we present MAP, a method that enables multiscale proteomic imaging of intact biological systems for combined extraction of the molecular identity, subcellular architectures, and intercellular connectivity of diverse cell types within a single tissue. MAP preserves both the three-dimensional (3D) proteome content and organization and the organ-wide cellular connectivity within an intact tissue-hydrogel hybrid, while rendering it reversibly size-adjustable up to four- to fivefold for multiresolution imaging.

2.3 Results

2.3.1 Organ-scale tissue expansion without loss of proteins

The key to MAP is to prevent intra- and interprotein crosslinking during the hydrogel-tissue hybridization step (Chung & Deisseroth 2013), and then to dissociate and denature proteins to allow natural expansion of the hybrid (Fig. 2.1a). We hypothesized that a high concentration of acrylamide monomers might effectively prevent protein crosslinking by quenching reactive methylols formed by the protein-formaldehyde reaction. If the acrylamide monomer concentration is low, the reactive methylols would react with amide groups within the same protein or adjacent proteins to form methylene bridges (Fig. 2.1a, left column) (Puchtler & Meloan 1985). Such intra- and interprotein crosslinking would prevent dissociation of protein complexes and limit subsequent tissue expansion (Sung et al. 1996). With increased acrylamide concentration (Fig. 2.1a, right column), methylols might preferentially react with excess acrylamide monomers, effectively reducing interprotein crosslinking while maximally tethering individual proteins to an expandable hydrogel mesh. Dissociation and denaturation of protein complexes with heat and anionic surfactant then facilitates natural expansion of the hydrogel-tissue hybrid while preserving overall spatial organization of the proteome.

To test our hypothesis, we first measured the effect of acrylamide concentration on tissue

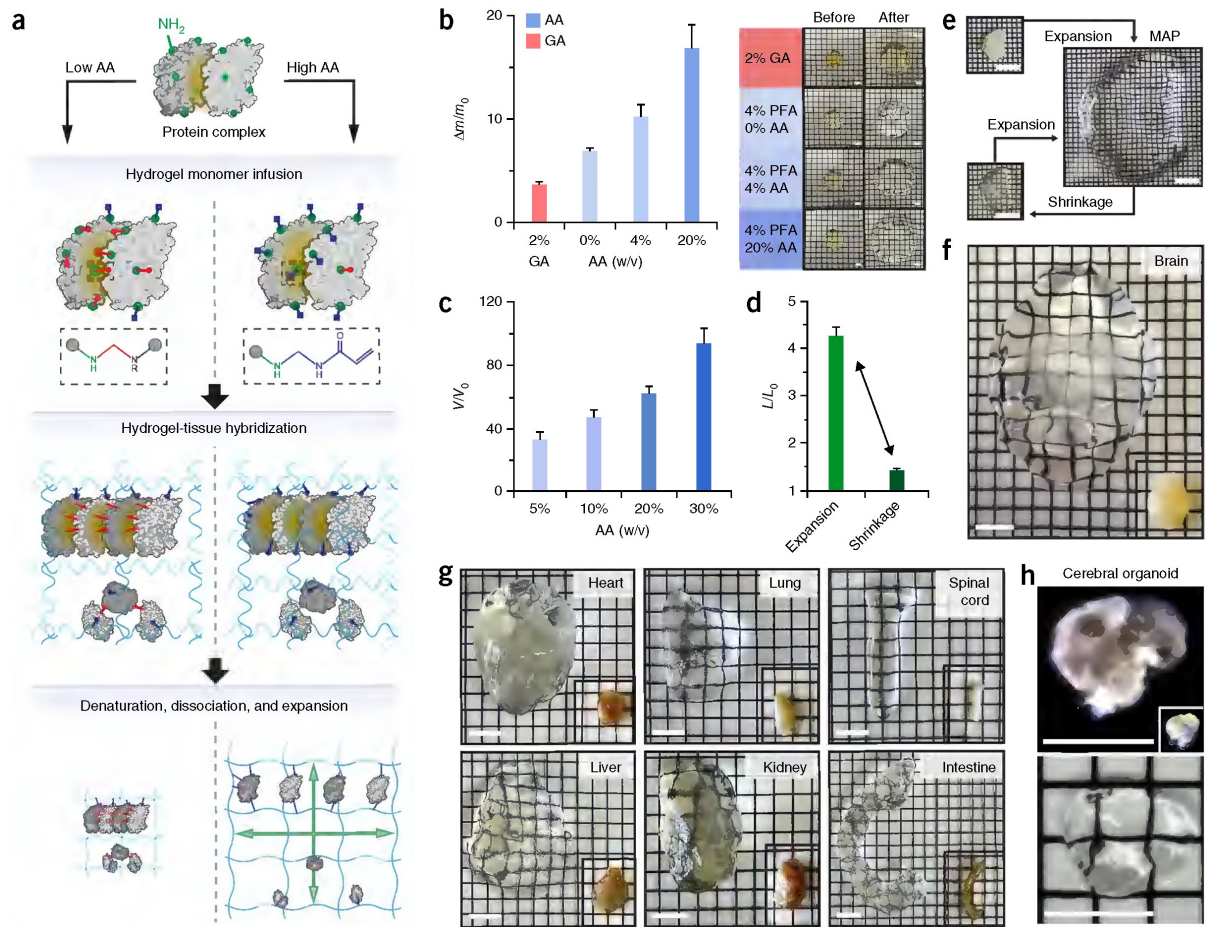


Figure 2.1: Magnified and accessible 3D proteome library of whole intact organs. (a) Comparison of hydrogel-tissue hybridization chemistry, subsequent protein denaturation, and hybrid expansion between low (left column) and high (right column) concentrations of acrylamide (AA; blue) infusion. High-concentration AA prevents intra- and interprotein crosslinking during the hydrogel-tissue hybridization step by quenching reactive methylols formed from amine residues (green) reacting with formaldehyde (red). Dissociation and denaturation of non-crosslinked protein complexes allows natural expansion of the hybrid. In low-concentration AA (left column), the reactive methylols react with available amine or amide groups within the same protein or adjacent proteins and form methylene bridges (red line). Such intra- and interprotein crosslinking prevents complete denaturation and dissociation of the proteins, and thereby limits subsequent tissue expansion. (b) Expansion after denaturation of BSA tissue phantom post-fixed in several AA concentrations. Representative images of tissue phantoms before and after expansion are shown. One-way ANOVA was performed (**P < 0.001). Error bars show s.d. (n = 3). Scale bars, 5 mm. (c) Expansion of 1-mm-thick coronal mouse brain slices perfused with several AA concentrations. One-way ANOVA was performed (P < 0.001). V₀, volume before expansion; V, volume after expansion. Error bars show mean ± s.d. (n = 6). (d) Average diameter of 1-mm-thick slices relative to the initial diameter after expansion and subsequent shrinkage. Slices were allowed 24 h for both expansion and shrinkage (n = 6). L₀, mean length of original brain; L, mean length after expansion and shrinkage. (e) Representative photos showing expansion and shrinkage of a 1-mm-thick coronal block. Starting from the top left, the original brain section, the expanded state, and the shrunken state are shown. (f,g) MAP applied to a whole mouse brain and other organs. The entire process from perfusion to full expansion took 7 d. Compared with the original organ size (pictures at right bottom corner), the final expansion of the brain showed a more than fourfold increase in length. (h) MAP applied to cerebral organoid. Top, darkfield images; bottom, brightfield image. Scale bars (e–h), 10 mm.

expansion. We prepared albumin-containing tissue phantoms and post-fixed them in 4% paraformaldehyde (PFA) with different concentrations (0–20%) of acrylamide. We incubated the tissue phantoms in detergent solution at 95 °C for 1 h to denature and disrupt protein aggregates. As expected, phantoms fixed in higher concentrations of acrylamide showed higher degrees of expansion in water (Fig. 2.1b). We observed a similar trend in mouse brain tissues that were perfused with different concentrations of acrylamide, polymerized, denatured, and expanded (Fig. 2.1c). Thus, we used high concentrations of acrylamide in order to maximize expansion during MAP in all subsequent experiments.

Using this approach, we achieved a fourfold linear expansion of a whole mouse brain within 7 d without protease treatment (Fig. 2.1f). Tissue expansion was reversible and tunable using buffers with different salt concentrations and osmolarities (Fig. 2.1d,e). This method is applicable to other organs including heart, lung, spinal cord, liver, intestine, and kidney, and also cerebral organoids (Fig. 2.1g,h and Supplementary Fig. 1).

2.3.2 Preservation of multiscale architectures

We next asked whether MAP retains multiscale structural information and enables super-resolution imaging with diffraction-limited microscopes. To estimate the amount of distortion incurred from expansion, we imaged gel-embedded cultured cells before and after MAP processing (Fig. 2.2a). At the subcellular scale, MAP expansion improved visualization of microtubules and allowed imaging of single tubular structures (Fig. 2.2b,c). The estimated distortion error (root-mean-square error, RMSE) was less than 3% of measured length at both the subcellular scale (Fig. 2.2d) and the multicellular scale (Fig. 2.2g). The degree of gel expansion was not a function of cell density, as indicated by the consistent local expansion within differently populated cell clusters (Fig. 2.2e,f).

To test whether MAP preserves multiscale tissue architectures, we imaged a 100- μ m-thick mouse brain block labeled with lectin before and after MAP (Fig. 2.2h). The distortion analysis showed less than 4% error (Fig. 2.2i), which was at most a twofold increase, compared to the inevitable distortion from sample mounting for imaging (Fig. 2.2i, remounting). Both the intra-vascular space with low protein concentration and the extra-vascular space with high protein concentration showed similar degrees of expansion (Fig. 2.2h, insets), suggesting that the effect of protein concentration and cell density on gel expansion is minimal. Diffraction-limited microscopy revealed fine 3D details of immunolabeled cells such as cytoskeletal filament structures (Fig. 2.2j,k,m) and better-resolved axonal fibers (Fig. 2.2l) after the MAP process. These results together indicate that MAP preserved multiscale structural information of biological samples and enabled super-resolution imaging with diffraction-limited microscopes, achieving ~60-nm lateral

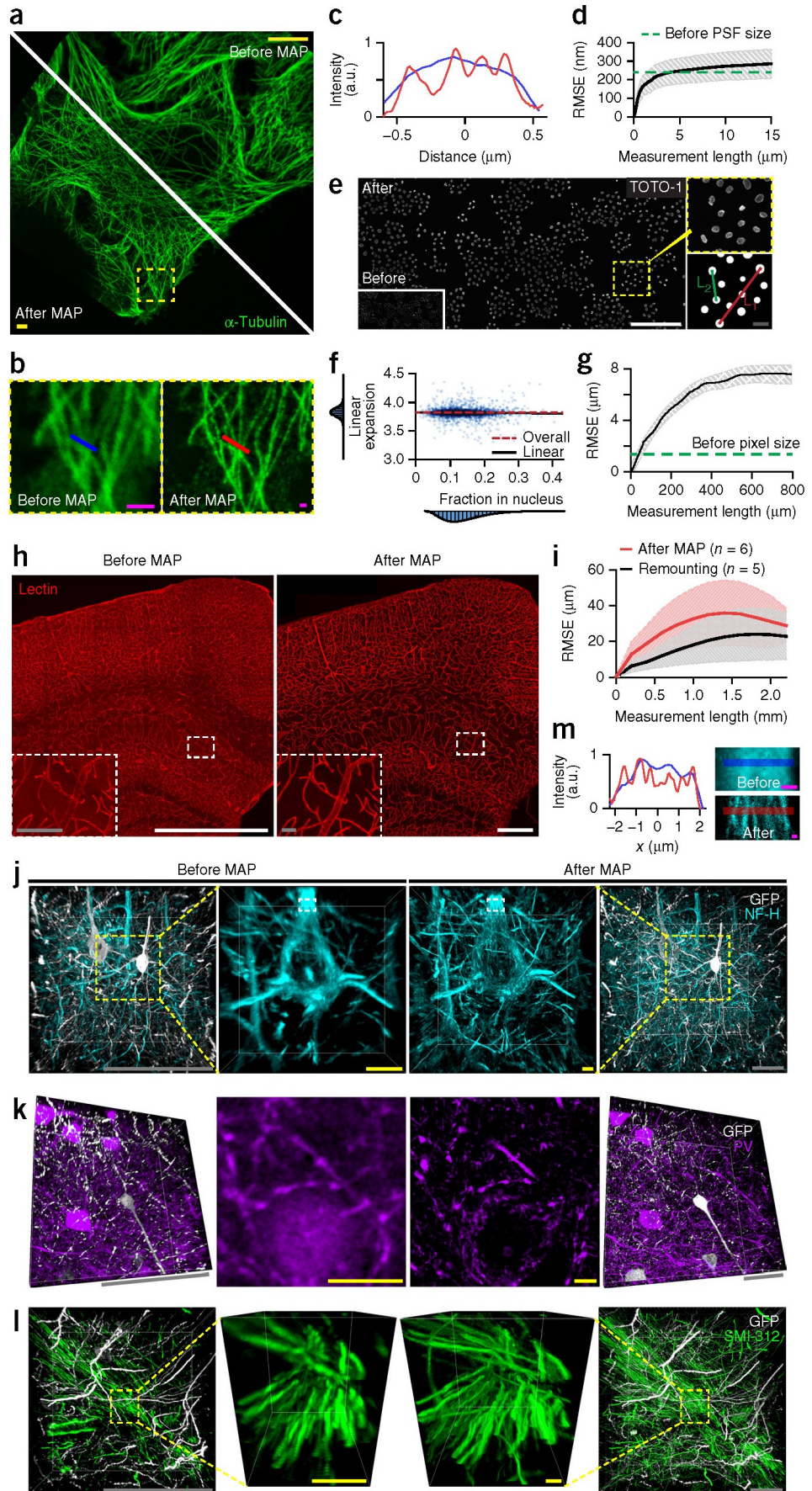


Figure 2.2: Comparison of multiscale architectures before and after MAP processing.

(a) HeLa cells stained for alpha-tubulin and imaged before and after MAP processing. (b) Fine tubulin structures imaged before and after expansion, respectively. (c) Intensity profiles along the paths indicated in b based on the pre-expansion size. (d) Root-mean-squared measurement error (RMSE) of tubulin images before and after MAP (black line, mean; filled area, s.d.; n = 4 samples). (e) Morphological image processing of gel-embedded HeLa cells before and after MAP processing. TOTO-1 was used to label nucleic acids. L1 and L2 represent the connecting line segments between two randomly chosen nuclei. (f) Local pairwise expansion ratios versus the fraction of the connecting line segment inside of nuclei (black line, overall expansion ratio (3.82); red dashed line, standard linear regression; $m = 0.04 \pm 0.02$, $b = 3.83 \pm 0.01$). (g) RMSE of TOTO-1 images before and after MAP, same as in d (n = 4 samples). (h) 100- m-thick mouse brain slice showing blood vessels stained with lectin before and after MAP processing. (i) RMSE of lectin images same as in d. Errors measured after MAP processing (n = 6 samples) are compared with errors measured between two rounds of embedding and imaging of the sample before MAP (n = 5 samples). (j-l) 100- m-thick mouse brain slices stained with anti-GFP antibodies and three other antibodies before and after MAP processing. Magnified 3D-rendered images in middle columns show the same structures imaged with the same microscopic resolution near optical sampling limit. Magnified 2D images showing parvalbumin (PV) ultrastructure in middle panels in k were taken from other samples. NF-H, neurofilament heavy unit. (m) Intensity plot (left) along the lines in zoom-in single sections (right) of the insets in j. The length scale is in terms of distance before MAP. Images were obtained using a 10 \times , 0.3 NA dry objective (e) and a 63 \times , 1.30 NA glycerol-immersion objective (a and b) with single-photon (1p) excitation by 488, 568, and 594 nm, and a 20 \times , 0.95 NA water-immersion objective (h and j-m) at the same resolution below optical sampling limit with either 1p excitation by 488 and 594 nm or 2p excitation by 780 nm. Scale bars, 1 mm (white; e and h), 100 m (gray; inset in e, and j-l), 10 m (yellow; a, and insets in j-l), and 1 m (magenta; b and m).

resolution.

2.3.3 Labeling proteome with conventional antibodies

We next asked if MAP preserves the 3D proteome composition and organization, and enables super-resolution imaging of fine subcellular architectures using commercially available antibodies. Antibody targets were selected from a wide range of antigens including membrane proteins, cytoplasmic proteins, nuclear proteins, neurofilament proteins, and synaptic proteins to survey the overall proteomic landscape (Fig. 2.3 and Supplementary Table 1). To validate the antibodies, we tested whether antibody staining of MAP-processed tissues shows comparable structures to PFA-fixed tissues, and antibodies from different host species targeting the same protein, if available, provide concordant images (Supplementary Figs. 2 and 3). We found that 100 of 122 antibodies were compatible with MAP-processed samples, and 43 of 51 target molecules were successfully visualized (Fig. 2.3, Supplementary Table 1, and Supplementary Figs. 2 and 3). This high success rate indicates that loss of epitopes by protein denaturation was minimal. Moreover, some antibodies (e.g., calbindin and calretinin) showed negative staining when different antibodies targeting the same endogenous protein showed strong signal (Fig. 2.3b and Supplementary Table 1). This result demonstrates that MAP preserves the tissue proteome with minimal loss of specific epitopes and that the library can be effectively probed using off-the-shelf antibodies without any modification.

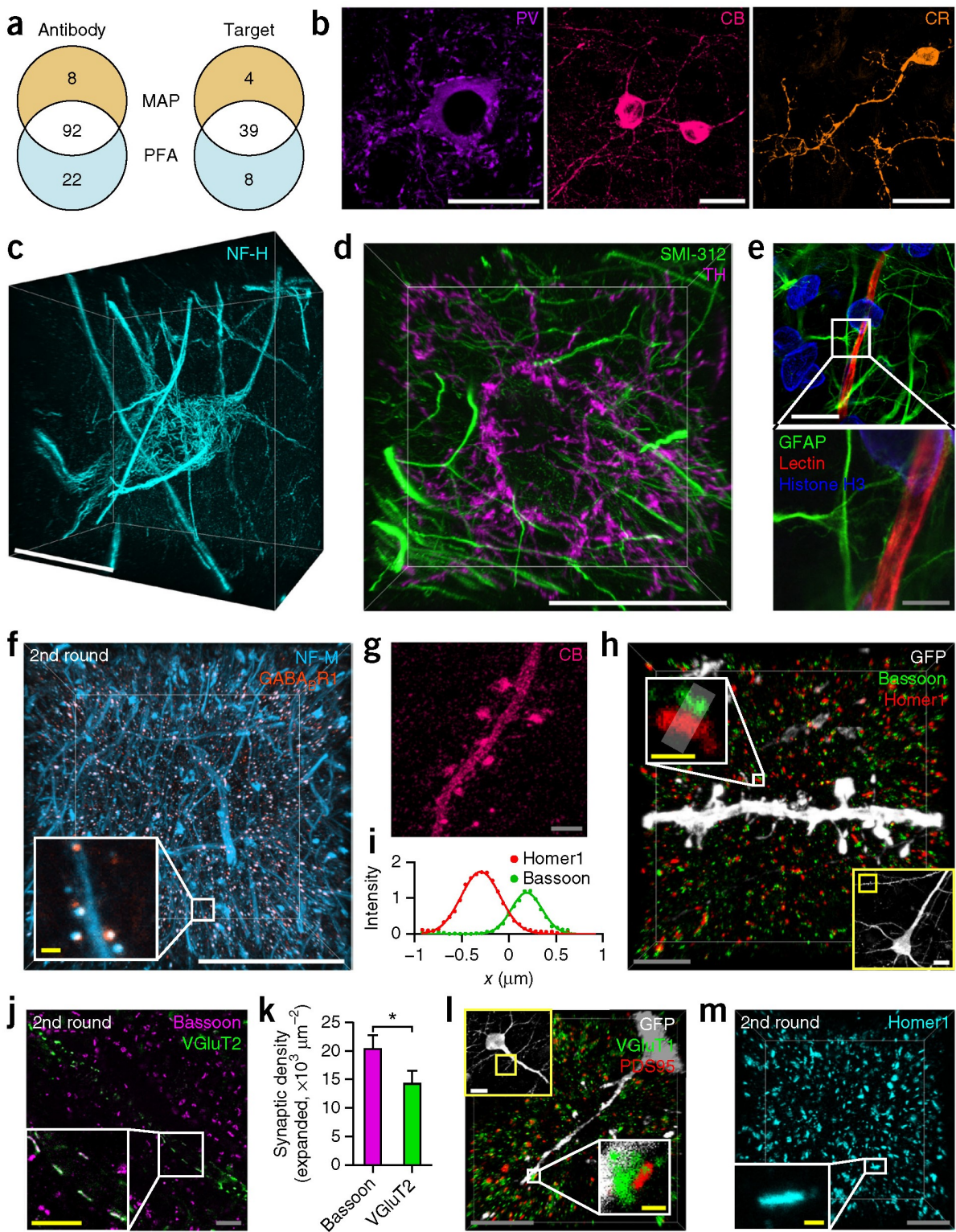


Figure 2.3: Super-resolution imaging showing the 3D proteome library and subcellular details of MAP-processed intact tissue.

(a) A total of 122 antibodies were tested on MAP-processed mouse brain sections and PFA-fixed control tissues (Supplementary Table 1). One hundred of 122 antibodies were compatible with MAP, and 43 of 51 target molecules were successfully labeled. (b) Representative images showing morphological details of parvalbumin (PV)-, calbindin (CB)-, and calretinin (CR)-positive cortical neurons. (c,d) 3D rendering of fine cytoskeletal structures visualized by neurofilament protein staining: NF-H in a cortical neuron (c), and SMI-312, a pan-axonal marker, and tyrosine hydroxylase (TH) in a subcortical neuron (d). (e) Structural relationship between astrocytes and capillaries visualized with glial fibrillary acidic protein (GFAP), lectin, and histone H3 in a subcortical region. (f) 3D rendering of a cortical sample stained with neurofilament medium unit (NF-M) and GABAB receptor subunit-1 antibodies. The inset shows synaptic neurofilaments co-localized with the gabaergic post-synaptic proteins. (g) Maximum intensity projection image showing dendritic spines visualized with a cell-type-specific marker, CB. (h) Synaptic structure resolved with a pre-synaptic marker, bassoon, and a post-synaptic marker, homer1, in a cortical region. Yellow box shows a GFP-positive neuron whose dendrite was imaged. The inset (white box) highlights the elliptical structures of pre- and post-synaptic proteins distributed at a synaptic junction. (i) Intensity plot along the axis of the synapse in h (rectangular region, expanded) showing the separation between pre- and post-synaptic distribution profiles. The lines represent the Gaussian curve fitting. (j,l,m) Additional synaptic markers successfully visualizing molecular synapses in MAP-processed tissues. (j) A glutamatergic pre-synaptic marker (VGluT2) co-localized with bassoon in a cortical region (inset). (k) Comparison of the number of synapses between bassoon and VGluT2 in j ($n = 3$ images). A two-tailed paired t test was performed (* $P < 0.05$). Error bars show mean \pm s.e.m. (l) The distribution of glutamatergic pre- (VGluT1) and post-synaptic (PSD95) markers in a cortical region. (m) 3D rendering showing the distribution of homer1 clusters in a subcortical region. The images in f, j, and m were obtained from samples stained in a second round. The images were obtained with a 25 \times , 0.95 NA water-immersion objective (b), a 40 \times , 1.25 NA oil-immersion objective (e), and a 63 \times , 1.30 NA glycerol-immersion objective (c, d, f–h, j, l, and m) with 1p excitation (488, 568, 594, and 647 nm). Scale bars, 50 μ m (white; b–f and low magnification images in h and l), 10 μ m (gray; inset in e, and h, j, l, and m), and 1 μ m (yellow; insets in f, h, j, l, and m).

2.3.4 Super-resolution imaging of 3D subcellular architectures

Preservation of both nanoscopic structures and the proteome in MAP enables super-resolution imaging of a broad range of fine subcellular architectures. Antibodies targeting filament proteins successfully visualized details of the cytoskeletal networks of various cell types (Fig. 2.3c–e and Supplementary Videos 1–4). No apparent filament fragmentations were observed in the magnified tissues. Labeling of glial fibrillary acidic protein (GFAP) enabled visualization the fine foot-process structures surrounding blood vessels (Fig. 2.3e and Supplementary Video 3) (Kosaka & Hama 1986; Khakh & Sofroniew 2015). Neurofilament medium subunit (NF-M) enabled visualization of both processes and synapses (Yuan et al. 2015), a subset of which co-localized with the postsynaptic marker, GABA B R1 (the C-terminal domain of the GABA B receptor subunit-1) (Fig. 2.3f and Supplementary Video 4). Labeling of calcium-binding proteins (parvalbumin, calbindin, and calretinin) robustly enabled visualization of morphological details of positive cells (Fig. 2.3b). A small subset of calbindin-positive fibers showed expression of calbindin in their dendritic spines (Fig. 2.3g). Many synaptic protein markers were compatible with MAP (Fig. 2.3f,h,j,l,m and Supplementary Table 1). Staining of synaptic proteins clearly visualized distinct and well-separated elliptical disk-shaped clusters of pre- and post-synaptic proteins (Fig. 2.3h,l,m and Supplementary Video 5), enabling their quantitative analysis (Fig. 2.3k).

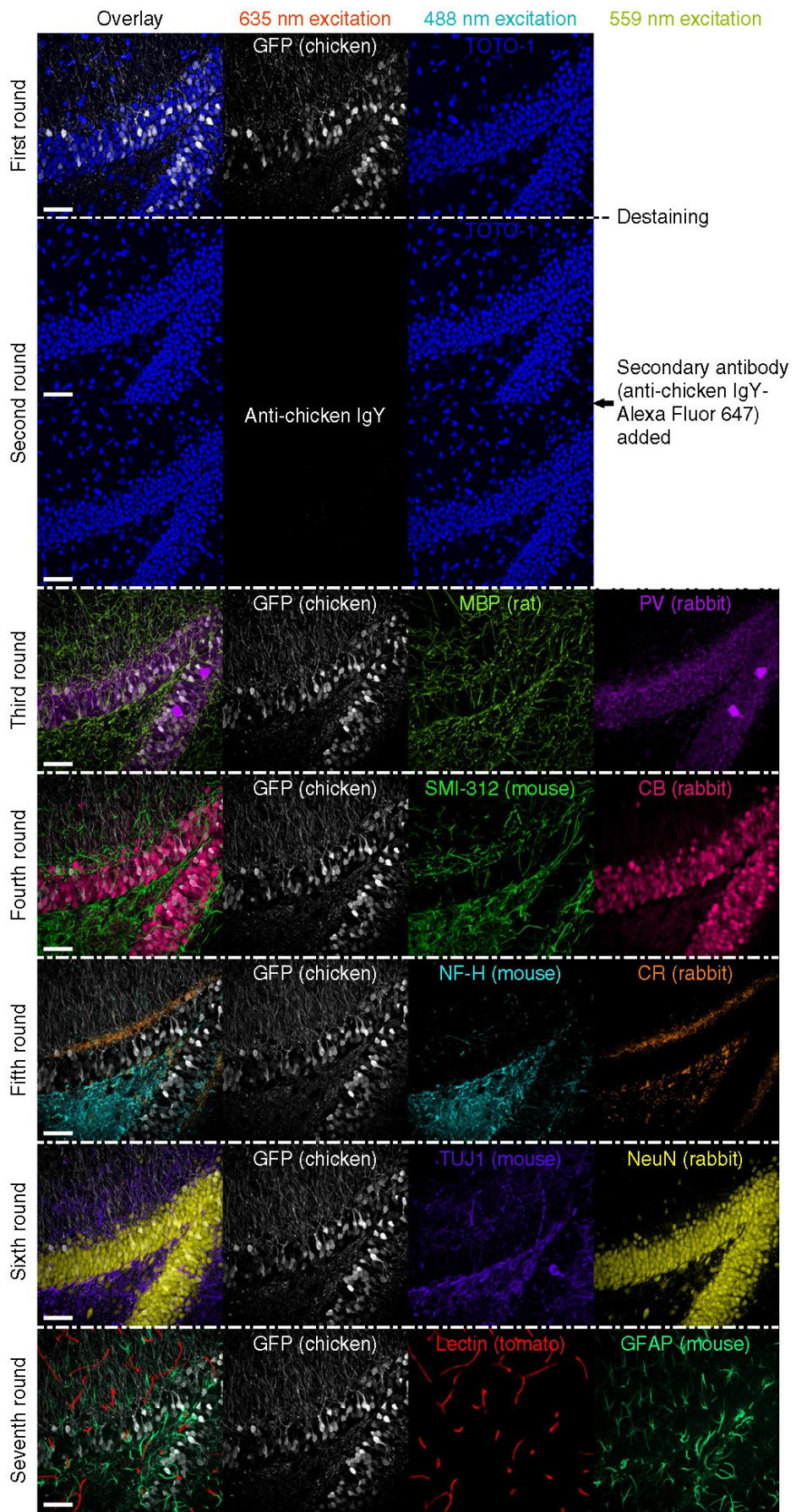


Figure 2.4: Multiplexed staining of MAP-processed tissue.

Repeated staining and destaining of a MAP-processed tissue. A 100- m-thick mouse brain slice including an anterior hippocampal region was used. The tissue in a PBS solution with 0.1 intensity projection of a 64- m thickness. Maximum intensity projection images are displayed. Host species of primary antibodies are shown in the parentheses. Break lines indicate destaining. GFP was stained and imaged at 635-nm excitation channel to show consistent labeling of the same antigen. 488- and 559-nm channels were used to show multiplexed labeling of diverse antigens and complete elution of imaged antibodies used in previous rounds. The same imaging and post-processing conditions were used for 635-nm channel images throughout the first and second rounds. MBP, myelin basic protein; TUJ1, neuron-specific class III beta-tubulin. Scale bars, 200 m.

2.3.5 Highly multiplexed immunolabeling

Another potential advantage of the MAP technology is that it enables highly multiplexed labeling and imaging of the magnified 3D proteome within a single tissue. We successfully performed seven rounds of immunostaining of a MAP-processed 100- m-thick mouse brain tissue with no obvious signs of tissue damage (Fig. 2.4). Outstanding mechanical stability of the MAP-processed sample enabled repeated manual handling of the tissue with tools that are widely used in biology laboratories. The images after destaining of the imaged anti-GFP antibody (first round) and after solely adding secondary antibodies targeting the eluted anti-GFP antibody (second round) showed little signal, suggesting that the destaining process effectively eliminates antibodies. For the following five rounds of labeling, we continued to use anti-GFP as a landmark in addition to two other antibodies for each round. The consistent GFP signals show that the same antigen can be repeatedly labeled without loss of antigenicity. Successful visualization of ten other targets demonstrated that MAP facilitated exploration of diverse proteins, structures, and cell types within a single tissue.

2.3.6 MAPing neural projections

We next explored the potential utility of MAP for mapping inter-areal neural connectivity. If MAP could preserve continuity of neural fibers within magnified, intact brain tissue along with its 3D proteome, highly specific antibodies would enable visualization of a subset of neural projections connecting different brain regions. The sparse labeling and enhanced spatial resolution offered by MAP may allow more accurate reconstruction of the labeled projections. In addition, highly multiplexed proteomic imaging may enable reconstruction of many different cell types with integrated molecular and fine morphological details in a single tissue.

To explore this possibility, we first asked if the continuity of neural processes is preserved within a magnified sample. We expanded a 0.5-mm-thick Thy1-eGFP mouse brain coronal block and then imaged GFP-labeled neurons and their projections (Feng et al. 2000). MAP preserved the continuity of the GFP-expressing projections spanning a large tissue

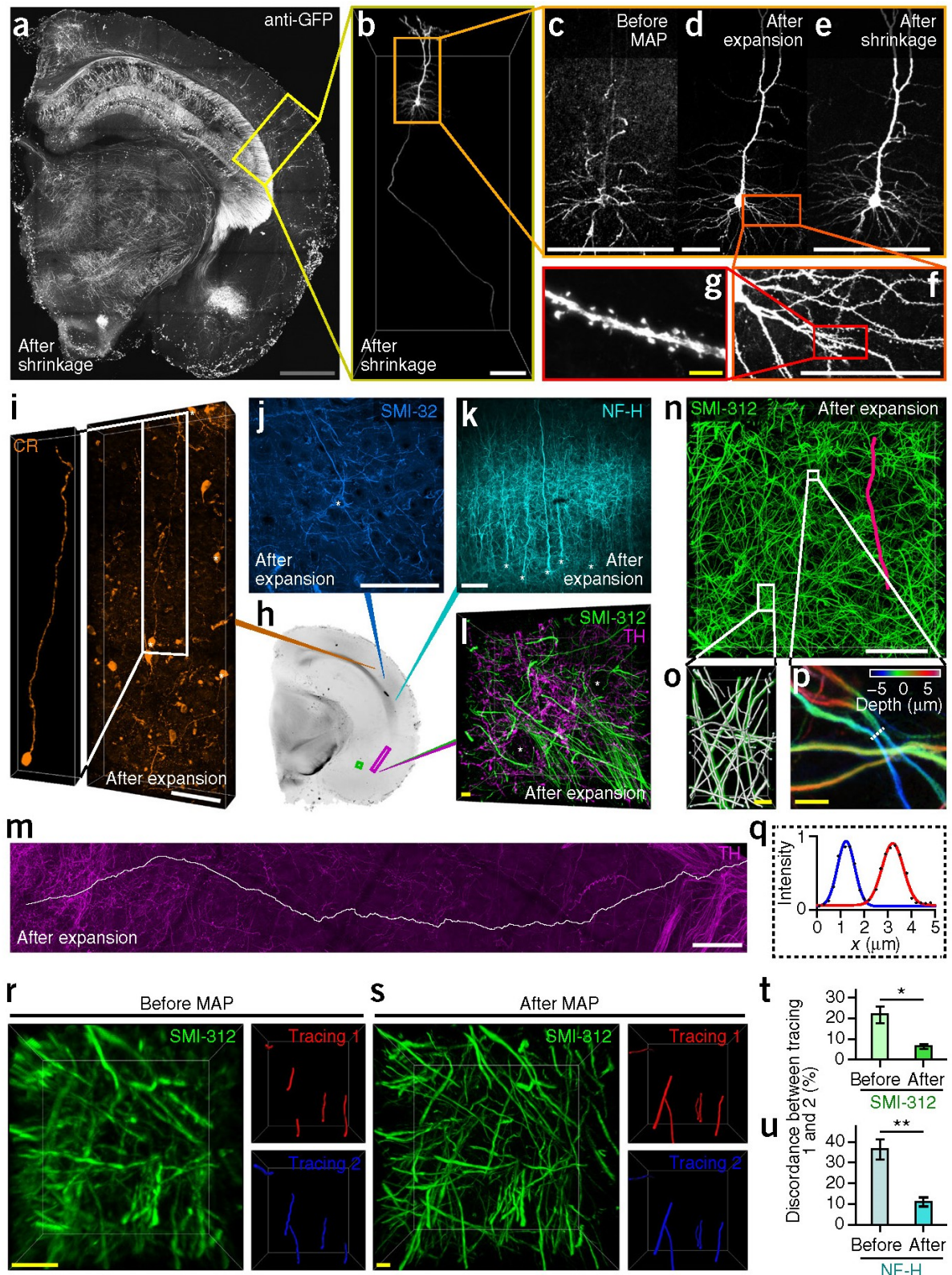


Figure 2.5: Intercellular connectivity and its reconstruction at single-fiber resolution in MAP-processed tissue.

(a–g) Connectivity and morphology of cells are preserved in the MAP-processed tissue. (a) A 500- m-thick slice of a mouse brain hemisphere stained with anti-GFP antibody and imaged after expansion and shrinkage. (b) The entire neuronal territory and axon fiber of a cortical pyramidal neuron included within the yellow-boxed region in the left panel. The volume was 3D reconstructed with background removal. (c–e) Images of the same neuron in b obtained with a 10 \times , 0.3 NA objective (c,d) and a 10 \times , 0.6 NA objective (e), showing its morphological details before MAP, after MAP expansion, and after MAP shrinkage. (f,g) Fine subcellular structures preserved and resolved in the expansion states: dendritic network (f) and dendritic spines (g). (h–l) Neuronal fibers and cell body (asterisks) morphology visualized using various markers (CR, SMI-32, NF-H, SMI-312, and TH) in different cortical (i–k) and subcortical (l) regions of a 1-mm-thick hemisphere slice (h). The inset in i shows the isolated neuronal cell body and its axon with background removal. (m) Long-range tracing (white line, longer than 3 mm) of an inter-regional TH neurofilament within the magenta box in h. (n) Subvolume within a square region in h (green box) containing dense SMI-312-positive fibers. The red line shows a tracing result across the volume. (o) One of the densest subregions in the left inset in n visualizing all individual fibers resolved and traced. (p) A dense region in the right inset in n showing closely crossing fibers. Depth-color coding of the fibers clearly shows good separation along the z-axis. (q) The intensities of the two fibers closely located in a similar plane in p are plotted and fitted to Gaussian curves to show their clear separation. (r,s) Comparison of manual tracing results of a 100- m-thick hippocampal sample stained with SMI-312 before (r) and after (s) MAP processing. Apparently detectable fibers were traced by two individuals. Discordant traces are selectively displayed for before MAP image (r), and the same traces, which resulted in concordant tracing after expansion, are shown for after MAP image (s). (t,u) Comparison of discordance ratios between manual tracing results before and after MAP processing. Two markers (SMI-312 and NF-H) were used with four regions of interest for each marker. Two-tailed paired t tests were performed (**P < 0.01, *P < 0.05). Error bars show mean \pm s.e.m. Images were obtained using a 10 \times , 0.6 NA CLARITY-optimized objective (a–c, e), a 10 \times , 0.3 NA water-immersion objective (d), a 20 \times , 0.95 NA water-immersion objective (m), a 63 \times , 1.30 NA glycerol-immersion objective (l and n–p), and a 25 \times , 0.95 NA water-immersion objective (f, g, i–k, r, and s) with 1p excitation by 488, 568, and 594 nm. Scale bars, 1 mm (gray; a), 200 m (white; b–f, i–k, m, n), and 10 m (yellow; g, l, o, and p, r, and s).

volume (Fig. 2.5a–f) as well as their fine morphological details (e.g., dendritic spines) (Fig. 2.5g). Immunolabeling of various cytoplasmic proteins including neurofilament proteins (e.g., NF-H and SMI-32), calcium-binding proteins, and metabolic enzymes (e.g., tyrosine hydroxylase) confirmed that MAP preserved the continuity of neural fibers of various cell types (Fig. 2.5h–n and Supplementary Videos 6–8). The preserved continuity enabled detection of single fibers selected in the immunostained tissue volumes (Fig. 2.5m–q and Supplementary Videos 7 and 8).

To test if MAP enables more accurate tracing of densely packed fibers, we imaged neurofilament-stained samples before and after MAP processing using a high numerical aperture (NA; 0.95) water-immersion objective. Two individuals not involved in image acquisition traced fibers within the sample volume (Fig. 2.5r,s). When we compared the concordance between the two tracing results, the discordant rate was significantly lower after MAP (Fig. 2.5t,u; SMI-312, n = 4, P = 0.020; NF-H, n = 4, P = 0.010), even though MAP enabled the tracers to detect more fibers (total numbers of traced fibers were 160 before MAP and 214 after MAP). This result demonstrates that MAP indeed enabled more accurate reconstruction of immunolabeled neural fibers.

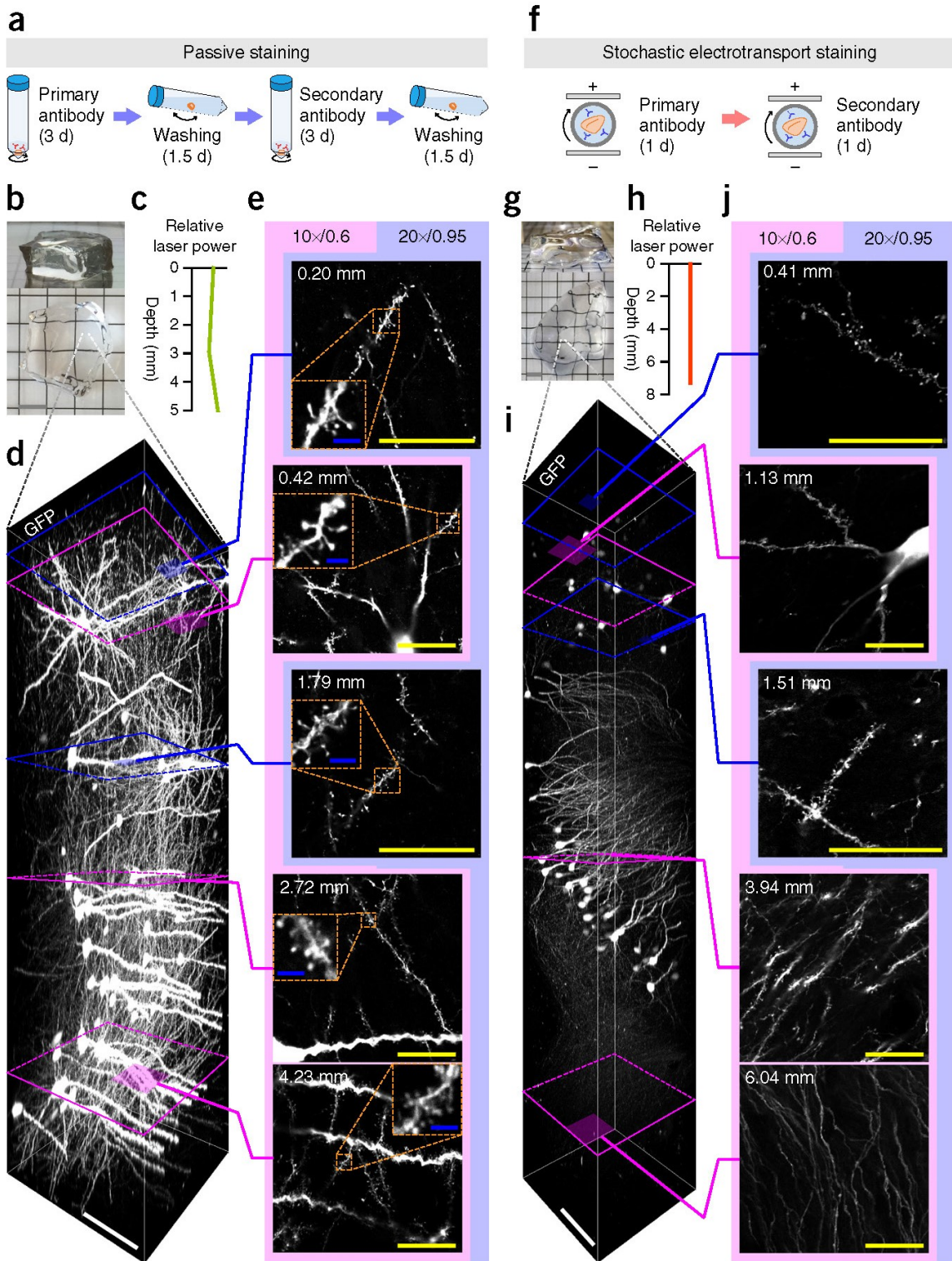


Figure 2.6: Immunolabeling and imaging of thick MAP-processed tissues.

(a–e) Passive staining of a 1-mm-thick (5 mm after expansion) dorsolateral mouse brain slice with anti-GFP antibodies. (a) The tissue was incubated for 3 d with primary antibody and 3 d with secondary antibody, and expanded in DI water. (f–j) Stochastic electrotransport²⁸ staining of a 2-mm-thick (8 mm after expansion) mouse hemisphere slice with anti-GFP antibodies. (f) The tissue was stained for 1 d with both primary and secondary antibodies. (b,g) Lateral (top panels) and top (bottom panels) views of the sample. White boxes indicate the regions of interest for z-stack images. The cortical (b) and hippocampal (g) regions were chosen at least 2.5- and 4-mm far from the lateral tissue boundary, respectively, to exclude the chance of dominant staining by lateral diffusion at a middle section. (c,h) Laser power used along depth to obtain a z-stack image. (d,i) Longitudinal tile-scan images along z-axis with 1p excitation and a 10 \times , 0.6 NA, 8-mm WD objective. (e,j) Sectional images at different depths either with a 10 \times , 0.6 NA, 8-mm WD (magenta) or a 20 \times , 0.95 NA, 2-mm WD (blue) objectives. The same image acquisition parameters were used for sectional images with each objective. Insets in e are zoom-in images showing dendritic spines. Scale bars, 5 mm (gray; b and g), 500 μ m (white; d and i), 100 μ m (yellow; e and j), and 10 μ m (blue; insets in e).

2.3.7 Immunolabeling and imaging of mm-thick tissues

Reconstruction of individual neurons requires labeling and imaging of thick brain tissues because nerve fibers can extend across a large volume. To test whether MAP is applicable to large-scale brain tissues, we expanded a 1-mm-thick mouse brain block (5-mm thick after expansion, Fig. 2.6b) and passively stained it with anti-GFP antibody (Fig. 2.6a). We then imaged the sample using both a high NA (0.95), short working distance (WD) (2 mm) water-immersion objective and a low NA (0.6), long WD (8 mm) CLARITY objective. Both objectives showed fine dendritic spines of GFP-expressing neurons throughout the entire volume (Fig. 2.6e). Imaging of the sample did not require depth-dependent modulation of the laser power, indicating that staining was uniform and that signal attenuation by light scattering was negligible (Fig. 2.6c,d). MAP is also compatible with stochastic electrotransport (S.-Y. Kim et al. 2015), a method that enables rapid tissue labeling. Using stochastic electrotransport, we were able to label an 8-mm-thick expanded tissue uniformly within only 2 d (Fig. 2.6f–j). The sample was highly transparent. We were able to image the 8-mm-thick sample successfully with the same laser power up to the working distance of the objective (Fig. 2.6h).

2.4 Discussion

As a step toward organ-scale reconstruction of diverse cell types and their surrounding environment and to advance the study of complex system-level interactions, we developed a simple and scalable method that enables preservation, reversible expansion, and imaging of the 3D proteome organization within an intact tissue. We discovered that the protein content of a whole organ can be preserved and magnified by preventing intra- and interprotein crosslinking, then denaturing and dissociating the protein complexes to allow natural expansion of hydrogel-tissue hybrids. The expanded hybrids secure both fine

subcellular architectures and organ-scale cellular connectivity. These multiscale properties can be directly imaged by using off-the-shelf antibodies to label the structures' constituent proteins. The high success rate that we achieved with commercial antibodies might be because synthetic peptides or denatured protein fragments are commonly used for conventional antibody production (Uhlen & Ponten 2005). An existing large antibody library, once validated, can be used without any modification. This technique is easy to implement, and it does not require any special equipment or chemicals.

MAP enables repeated interrogation of the same expanded specimen. This is possible because the preserved epitopes, which have already reached complete denaturation by harsh treatment (95 °C, 200 mM sodium dodecyl sulfate (SDS)) for expansion, do not undergo any substantial modification during the milder antibody elution step (70 °C, 200 mM SDS). We performed seven rounds of staining of the same tissue without any signs of tissue damage. However, the practical limit of this approach must be carefully examined.

MAP has the potential to enable scalable super-resolution imaging of large-scale samples. Unlike other methods, thick tissues can be labeled on a practical time scale because antibody-labeling occurs after complete lipid removal and tissue permeabilization. The great transparency of the MAP-processed samples allows high-resolution imaging of the physically expanded tissue with minimal loss of resolution. Currently, 1.0 NA, 2.5-mm WD water-immersion objectives are best suited for MAP. Although the 1.0 NA, 8-mm WD CLARITY objective has the longest WD, it does not provide high-quality images because it is optimized for immersion media with a high refractive index (RI). Further development of high-NA, long-WD water objectives or the development of high-RI immersion media that are compatible with MAP would extend the utility of MAP. Another challenge in the MAP approach is the dilution of fluorescent signals that accompanies physical volumetric expansion. Fourfold linear expansion decreases signal density by 64-fold. Therefore, much higher laser power is required, which in turn causes photobleaching. Future studies will need to explore the compatibility of signal amplification techniques with MAP.

The reversible modulation of physical sample size that is attained with MAP enables multiscale proteomic imaging of a single tissue to capture both system-scale properties and fine local details in a practical way. For example, following sample shrinkage, global projection patterns of labeled neurons may be imaged using high-speed microscopy techniques and long WD objectives (e.g., 25 \times , 1.0 NA, 8-mm WD objective, currently available) (Tomer et al. 2014). After imaging, the same tissue can be expanded for super-resolution imaging of regions of interest. The expanded tissue may need to be sliced before imaging to meet the objective's WD limit. A microscope with a built-in vibrating-blade microtome could also be used for whole-mount imaging to avoid loss of connectivity information (Ragan et al. 2012; Economo et al. 2016; Albanese & Chung 2016). This

approach may allow us to drastically reduce the imaging time and costs associated with data storage and handling of expanded samples.

The advantages of MAP (Supplementary Table 2) may allow combined extraction of rich molecular details, minute subcellular architectures, and cellular connectivity from diverse cell types within a single tissue. Together with its simplicity and broad applicability, MAP may complement existing methods and enable new approaches in the study of complex biological systems.

2.5 Methods

Methods and any associated references are available in the online version of the paper.

Note: Any Supplementary Information and Source Data files are available in the online version of the paper.

2.6 Acknowledgements

The authors thank the entire Chung laboratory for support and helpful discussions. K.C. was supported by Burroughs Wellcome Fund Career Awards at the Scientific Interface, the Searle Scholars Program, Packard award in Science and Engineering, JPB Foundation (PIIF and PNDRF) and NIH (1-U01-NS090473-01). Resources that may help enable general users to establish the methodology are freely available online (<http://www.chunglabresources.org>). K.C. is a co-founder of LifeCanvas Technologies, a startup that aims to help the research community adopt technologies developed by the Chung Laboratory.

2.7 Author Contributions

T.K., J.S., J.-Y.P., and K.C. designed the experiments and wrote the paper with input from other authors. T.K. stained and imaged mouse samples. J.S. performed the gel and cell experiments. T.K. and J.S. analyzed the data. J.-Y.P. prepared mouse tissues. J.-Y.P. and V.M. processed mouse MAP samples. A.A. performed the cell and organoid experiments. E.M., Y.-G.P., and T.K. performed the antibody validation test. J.H.C. performed stochastic electrotransport staining. Y.-G.P. and T.K. obtained synaptic images. J.-Y.P., V.M., T.K., and J.S. performed tracing. J.C. performed the gel experiment.

K.C. supervised all aspects of the work.

2.8 Competing Financial Interests

The authors declare competing financial interests: details are available in the online version of the paper.

2.9 Methods

2.9.1 BSA hydrogel denaturation and expansion

Stock solutions of 40% BSA, 40% acrylamide (AA), 32% paraformaldehyde (PFA), and 1% VA-044 were made and kept on ice throughout the experiment. A 10-mL solution of 4% BSA, 4% AA, 4% PFA, 0.1% bis-acrylamide (BA), and 0.1% VA-044 was made in phosphate-buffered saline (PBS). The solution was polymerized under vacuum at 37 °C for 2 h, and the resulting albumin-containing tissue phantom was sectioned. Individual tissue phantom sections were washed in excess PBS with shaking for 12 h. After washing, four phantoms were placed in 10 mL of each of the following PBS solutions for 4 h at 37 °C: 2% glutaraldehyde (GA), 4% PFA, 4% AA with 4% PFA, and 20% AA with 4% PFA. Tissue phantoms were washed similarly, massed, photographed, and then incubated in a 200 mM SDS solution with 50 mM sodium sulfite for 1 h at 95 °C. Phantoms were washed again and incubated in deionized (DI) water for 12 h. After expansion, phantoms were massed and photographed.

2.9.2 General MAP protocol

- i. Perfusion and hydrogel embedding. Thy1-eGFP-M mice (6–8 weeks old, male and female) were housed in a reverse 12-h light/dark cycle with unrestricted access to food and water. All experimental protocols were approved by the MIT Institutional Animal Care and Use Committee and the Division of Comparative Medicine and were in accordance with guidelines from the US National Institutes of Health. After anesthesia, the mice were first washed transcardially with a mixture of 2–5% AA, 0–0.05% BA, 0–0.8% sodium acrylate (SA), and PBS, followed by perfusion with a mixture of 4% PFA, 30% AA, 0.05–0.1% BA, 10% SA, 0.1% VA-044 or V-50, and PBS. The perfusion solution could be slightly turbid. Upper transparent solution was used after centrifugation during 3 min with 1,000g. All solution was protected

from light and kept on ice before perfusion. Control samples were perfused first with PBS and then with 4% PFA and PBS. The brain and other organs (heart, lung, liver, intestine, kidney, and spinal cord) were harvested and incubated in 20–40 mL of the same fixative solution at 4 °C for 2–3 d and then for 1–3 d at room temperature (RT) with gentle shaking to ensure uniform chemical diffusion and reaction throughout the sample. Following the diffusion and fixation steps, hydrogel-tissue hybridization was performed *in situ* by incubating the tissues using Easy-Gel (LifeCanvas Technologies) with nitrogen gas at 45 °C for 2 h.

- ii. Tissue denaturation. Hydrogel-embedded tissues were incubated overnight in a solution of 200 mM SDS, 200 mM NaCl, and 50 mM Tris in DI water (pH titrated to 9.0) at 37 °C with gentle shaking. The samples were then incubated at 70 °C for 0–50 h and 95 °C for 1–24 h depending on their size using EasyClear (LifeCanvas Technologies). Whole organs were incubated for 24–48 h at 70 °C followed by 12–24 h at 95 °C. 1-mm-thick brain slices were incubated for 5 h at 70 °C and then at 95 °C for 1 h.
- iii. Expansion. Denatured tissues were incubated in 40–100 mL DI water at RT for 12–48 h with gentle shaking. During DI water incubation, the solution was changed every 3–5 h.

2.9.3 Expansion according to various AA and SA concentrations

After anesthesia, mice were washed transcardially with 4% AA, 0.05% BA, 0.8% SA, 0.1% VA-044, and PBS and then with 4% PFA, 0.05% BA, 0.1% VA-044, one of four AA and SA combinations (5% AA + 0.8% SA, 10% AA + 1.7% SA, 20% AA + 3.3% SA, and 30% AA + 5% SA) in PBS. Tissues were incubated in 20 mL of the same fixative solution at 4 °C for 2 d and 5 h at RT with gentle shaking. After hydrogel-tissue hybridization the samples were incubated in denaturation solution at 70 °C for 5 h and 95 °C for 1 h with gentle shaking. Denatured tissues were incubated in 40 mL DI water at RT for 12 h with gentle shaking. During DI water incubation, the solution was changed every 3–5 h. Fiji (National Institutes of Health) was used to measure the size of the expanded samples (Schindelin et al. 2012).

2.9.4 Shrinkage and RI matching

A customized RI matching solution was made by dissolving 50 g diatrizoic acid, 40 g N-methyl-d-glucamine, and 55 g iodixanol per 100 mL PBS (Kim, S.-Y. et al. 2015). The RI was targeted to 1.47. This solution was used for both shrinkage and imaging.

Depending on sample size, samples were incubated in 1–10 mL solution at RT for 2–24 h with gentle shaking. The solution was changed every 1–12 h. For imaging tissues before MAP processing, samples were incubated in 1–10 mL of this solution without PBS at RT with gentle shaking for 2–5 h before imaging.

2.9.5 MAP processing of cerebral organoid

Cerebral organoids were made from stem cells following a previously described protocol (Lancaster & Knoblich 2014). Organoids were initially fixed in 4% PFA for 15 min, incubated in a mixture of 4% PFA, 30% AA, 0.1% BA, 10% SA, 0.1% V-50, and PBS for 24 h at 4 °C, followed by 24 h, at RT. Hydrogel embedding, tissue denaturation, and expansion were processed similarly to “General MAP protocol.”

2.9.6 Cultured cell experiment

For tubulin imaging in HeLa cells, 8-mm round glass coverslips were coated in 0.1% gelatin in ultrapure water (Millipore). Coverslips were placed in a 48-well plate and seeded with 50,000 HeLa cells overnight. To obtain comparable images before and after MAP processing, cells were washed, fixed with 3% PFA + 0.1% GA in PBS for 10 min, and switched to a solution of 4% PFA, 30% AA in PBS for 8 h at 37 °C. Cells were then placed in 0.1% sodium borohydride for 7 min at RT then incubated in 100 mM glycine for 10 min at RT. Cells were washed and stained with anti-tubulin (Abcam, ab6160), Alexa Fluor 594-conjugated secondary (Abcam, ab150152) antibodies and TOTO-1 (Thermo Fisher Scientific). Cells were mounted in 2,2 -thiodiethanol (Sigma) and imaged with a 63×, 1.3 NA glycerol-immersion objective with the Leica microscope system. Cells were washed extensively and embedded into a MAP hybrid polymer by addition of 20 L of Cell-MAP solution (20% AA, 7% SA, 0.1% BA, 0.5% TEMED, 0.5% ammonium persulfate in PBS). Ammonium persulfate was added last from a freshly prepared 5% stock solution. Cell-MAP solution was quickly added to the coverslip and left to polymerize for 4–5 min. Gels were peeled off the coverslip using forceps, washed extensively and denatured for 30 min in denaturation buffer at 95 °C. Cell-MAP gels were washed extensively, restained with anti-tubulin antibody and TOTO-1 and reimaged.

2.9.7 Immunostaining of brain tissue

For typical staining, MAP-processed 100- to 500- m-thick mouse brain coronal slices were incubated with primary antibodies (typical dilution, 1:100) in PBS with 1% (wt/vol)

Triton X-100 (PBST) at 37 °C for 8–16 h, followed by washing at 37 °C for 1–2 h in PBST three times. The tissue was then incubated with secondary antibodies (typical dilution, 1:100) in PBST at 37 °C for 6–16 h, followed by washing at 37 °C for 1–2 h in PBST three times. For antibody validation of a given antibody, 100- m-thick PFA-fixed control and MAP-processed samples were stained with the same titer of primary and, if necessary, secondary antibodies overnight in PBST. See Supplementary Table 1 for the list of antibodies used. To destain for multiplexed labeling, samples were incubated in a denaturation solution 6–16 h at 70 °C, and washed with PBST at 37 °C for 1–2 h three times.

2.9.8 Mounting and imaging

Samples were mounted on a slide glass. Blu-Tack adhesive was applied on the Petri dish or the slide glass, and samples were covered with a glass-bottom Willco dish. The space between the bottom material and the Willco dish around the sample was filled with either shrinkage solution or DI water according to the sample immersion medium. Large expanded samples were additionally placed on a 120-mm-diameter Petri dish, and the dish was filled with DI water. Expanded or shrunk samples were stabilized for at least 1 h before imaging. Samples were imaged with either the Olympus FV1200MPE microscope system or the Leica TCS SP8 microscope system. A 10×, 0.6 NA CLARITY-optimized objective (XLPLN10XSVMP; 8.0-mm WD) was used with the Olympus system to obtain wide-field images of shrunk samples and z-stack images of large samples. The images of MAP-processed samples were obtained with a 10×, 0.3 NA water-immersion objective, a 20×, 0.95 NA water-immersion objective, and a 40×, 1.25 NA oil-immersion objective with the Olympus system, or a 10×, 0.3 NA water-immersion objective, a 25×, 0.95 NA water-immersion objective, and 63×, 1.30 NA glycerol-immersion objective with the Leica system. Single-photon confocal laser scanning imaging was performed with 405-, 488-, 559-, and 635-nm lasers (Olympus) or a white-light laser (Leica). Mai Tai DeepSee (Spectra-Physics) was used for multi-photon excitation with 780-nm wavelength. The images were visualized and analyzed with Fiji or Imaris (Bitplane).

2.9.9 Large tissue staining

1- and 2-mm-thick mouse brain coronal slices were prepared by “General MAP protocol,” and expanded. A 1-mm-thick slice was chopped to about 3 mm × 3 mm × 1 mm (dimensions before MAP). The sample was stained passively with Alexa Fluor 594-conjugated rabbit anti-GFP antibody (Life Technologies, A21312) for 3 d and Alexa Fluor 594-conjugated donkey anti-rabbit IgG antibody (Abcam, ab150072) for 3 d. 20

L of antibody was used in 500 L PBST, and was washed with 40 mL PBST for 1.5 d (three times in total) for each antibody. We used stochastic electrotransport 28 to stain a 2-mm-thick slice with Alexa Fluor 647-conjugated rabbit anti-GFP antibody (Life Technologies, A31852) and Alexa Fluor 647-conjugated donkey anti-rabbit IgG antibody (Abcam, ab181347). For each antibody, we first electrotransported stochastically a solution containing 20 L of antibody in 4 mL of 0.6 M N-cyclohexyl-3-aminopropanesulfonic acid (CAPS), 0.2 M Tris, 100 mM NaCl, 20 mM SDS, 1% BSA with an electrophoresis buffer containing 0.3 M CAPS, 0.2 M Tris, 20 mM SDS, 30% sorbitol for 21 h. It was then electrotransported stochastically in a solution containing 4 mL of 0.3 M CAPS, 0.2 M Tris, 20 mM SDS, 30% sorbitol, 1% BSA, and 1% Triton X-100 with an electrophoresis buffer containing 0.04 M Tris, 0.01 M phosphate, 30% sorbitol for 8 h. These two steps complete the stochastic electrotransport labeling. The stained sample was expanded in a solution containing 0.01% (wt/vol) heparin sodium porcine mucosa (Sigma, SRE0027) and 1% Triton X-100 in DI water, and then imaged.

2.9.10 Cell distortion analysis

Before and after MAP processing tubulin images were first registered using a scaled-rotation transformation in Fiji. Non-rigid invertible B-spline registration was performed with an 8×8 control point grid in bUnwarpJ. Vectors of different length were subjected to the resulting nonlinear transformation, and the input-output difference norm was sorted based on the input vector length and then averaged by root-mean-square. For morphological image processing of nuclei, TOTO-1 images before and after MAP-processing were first registered using a scaled-rotation transformation in Fiji. The registered images were segmented by thresholding and converted to circular particles with equivalent average radii calculated from the “Analyze Particles” function in Fiji. Matched pairs of cells from the before and after images were randomly chosen, and the expansion ratio was calculated from the ratio of the connecting line segment lengths. The fraction in nuclei was obtained by summing the intensity profile along the connecting line segment and averaging the sums from the before and after binary masks.

2.9.11 Tissue distortion analysis

After anesthesia, mice were first washed transcardially with 2% AA in PBS followed by perfusion with 4% PFA and 30% AA in PBS. Thy1-eGFP-M mouse brains were harvested and incubated in 20 mL of the same fixative solution at 4 °C overnight and at 37 °C for 3 h. Brains were sectioned to 100- m-thick coronal slices with a vibrating microtome. Slices were stained and imaged to obtain “before MAP” images, and then incubated in

a solution containing 4% PFA, 30% AA, 0.1% BA, 10% SA, and 0.1% V-50 in PBS at RT for 8 h. Hydrogel-tissue hybridization was performed *in situ* by incubating the tissues with nitrogen gas at 45 °C for 2 h. Hydrogel-embedded tissues were incubated in denaturation solution at 37 °C for 1 h and 95 °C for 0.5–1 h. Samples were then stained with the same markers and imaged to obtain “after MAP” images.

To quantify distortion errors, regions of ~3 mm × 2.5 mm in size that included cortex and hippocampus were stained with DyLight 594-conjugated lectin (Vector Laboratories, DL-1177) before (8 L in 200 L PBST for up to 8 samples) and after (2 L in 200 L PBST for each sample) MAP processing. Samples were incubated in RI matching solution after staining and mounted and imaged before MAP processing. Five samples were repeated for incubation, mounting and imaging to measure mounting errors. After MAP processing, six samples were stained, expanded in DI water, and imaged. Keypoints of the vasculature in volumetric images were detected and matched between two image sets with a MATLAB code implementing the 3D Harris Corner Detector and 3D SIFT algorithm as described previously (Murray et al. 2015). Using custom-built graphical user interface software developed with Delphi XE4 (Embarcadero Technologies), redundant keypoints closely located to each other and keypoints at tissue margins were removed. Tissue sizes were estimated by the area defined by a convex hull encompassing all keypoints, and the expansion ratio was calculated as the ratio between two squared roots of the areas. The correspondence information was used to generate a regularly spaced deformation mesh using a 3D thin plate spline code written by Yang (<http://www.mathworks.com/matlabcentral/fileexchange/37576-3d-thin-plate-spline-warping-function>). Lengths between each pair of grid points were calculated in both pre-MAP and post-MAP images, considering the expansion ratio. The difference between the two lengths was measured as a distortion error. After averaging the squared errors for each measurement length, the square root of the averages was collected from the samples to obtain statistical values of error.

2.9.12 Neurofilament tracing

Tracing of individual neurons was performed using either Fiji or Imaris. For manual tracing of a long tyrosine hydroxylase fiber, a representative fiber was chosen during confocal imaging acquisition and traced by moving the motorized stage and adjusting the z-level. During the tracing, ambiguous crossovers were resolved by obtaining high-magnification subvolume images. After tile-scanning, the target fiber was re-identified from the image volume using Fiji and marked to be displayed in a two-dimensional plane. For the semi-automatic tracing of SMI-312 fibers in a dense region, the entire 800 m × 800 m × 150 m (expanded) data set was loaded along with a filament tool into a

‘Surpass’ instance using Imaris. An autopath calculation was performed using a single starting point as indicated in Supplementary Video 8. The fiber endpoint was designated by selecting the portion of the fiber exiting the imaged volume. The fiber representation was changed to a cone representation to visualize the filament diameter as well as the tracing path. The tracing fidelity was confirmed by inspection. To trace multiple fibers in a dense region, the full data set was cropped to the region indicated in Figure 2.50 using the ‘3D crop’ tool, and similar autopath calculations were performed for each fiber. For traceability comparison between before and after MAP, we imaged the same tissues before and after MAP processing at the same resolution near the optical sampling limit with the Leica system and a $25\times$, 0.95 NA water-immersion objective. Two individuals not involved in imaging acquisition performed manual tracing using autodepth assistance in Imaris, and discordance ratios between manual tracing results before and after MAP processing were calculated.

2.9.13 Synaptic and fiber intensity profiles

The regions of interest were imported into Fiji. Lines were drawn perpendicular to the synaptic junction or near the fibers of interest and intensity profiles were obtained with adjusting the line width. For synaptic intensity profiles, two Gaussian distributions were fit to the distinct peaks by simultaneous minimization of the sum of squared residuals. Synaptic densities for bassoon and VGluT2 were calculated from three non-overlapping xy-images ($235\text{ }\mu\text{m} \times 235\text{ }\mu\text{m}$) of expanded samples. The images were segmented by thresholding, and individual synaptic structures for each channel were counted using the “Analyze Particles” function in Fiji. The synaptic densities were calculated based on the frame area, and the s.d. was calculated from the three replicates.

2.10 References

- Agato, C., Uhlén, M. & Hober, S., 2004. Genome-based proteomics. *Electrophoresis*, 25(9), pp.1280–1288.
- Albanese, A. & Chung, K., 2016. Whole-brain imaging reaches new heights (and lengths). *eLife*, 5, pp.1–3.
- Berglund, L. et al., 2008. A gene-centric human protein atlas for expression profiles based on antibodies. *Molecular and Cellular Proteomics*, 7(10), pp.2019–2027.
- Betzig, E. et al., 2006. Imaging intracellular fluorescent proteins at nanometer resolution. *Science*, 313(5793), pp.1642–1645.
- Chen, K.H. et al., 2015. Spatially resolved, highly multiplexed RNA profiling in single cells. *Science*, 348(6233), pp.1360–1363.
- Chung, K. & Deisseroth, K., 2013. CLARITY for mapping the nervous system. *Nature methods*, 10(6), pp.508–13. Available at: <http://www.ncbi.nlm.nih.gov/pubmed/23722210>.
- Craddock, R.C. et al., 2013. Imaging human connectomes at the macroscale. *Nature Methods*, 10(6), pp.524–539.
- DeFelipe, J., 2010. From the connectome to the synaptome: An epic love story. *Science*, 330(6008), pp.1198–1201.
- Dodt, H.U. et al., 2007. Ultramicroscopy: Three-dimensional visualization of neuronal networks in the whole mouse brain. *Nature Methods*, 4(4), pp.331–336.
- Economou, M.N. et al., 2016. A platform for brain-wide imaging and reconstruction of individual neurons. *eLife*, 5(JANUARY2016), pp.1–22.
- Feng, G. et al., 2000. Imaging Neuronal Subsets Neurotechnique. *Neuron*, 28, pp.41–51.
- Hanash, S., 2004. HUPO initiatives relevant to clinical proteomics. *Molecular and Cellular Proteomics*, 3(4), pp.298–301.
- Helmstaedter, M., 2013. Cellular-resolution connectomics: Challenges of dense neural circuit reconstruction. *Nature Methods*, 10(6), pp.501–507.
- Hess, S.T., Girirajan, T.P.K. & Mason, M.D., 2006. Ultra-high resolution imaging by fluorescence photoactivation localization microscopy. *Biophysical Journal*, 91(11), pp.4258–4272. Available at: <http://dx.doi.org/10.1529/biophysj.106.091116>.
- Kay, K.R. et al., 2013. Studying synapses in human brain with array tomography and

electron microscopy. *Nature Protocols*, 8(7), pp.1366–1380. Available at: <http://dx.doi.org/10.1038/nprot.2013.078>.

Khakh, B.S. & Sofroniew, M.V., 2015. Diversity of astrocyte functions and phenotypes in neural circuits. *Nature Neuroscience*, 18(7), pp.942–952.

Kim, S.-Y. et al., 2015. Stochastic electrotransport selectively enhances the transport of highly electromobile molecules. *Proceedings of the National Academy of Sciences*, 112(46), pp.E6274–E6283. Available at: <http://www.pnas.org/lookup/doi/10.1073/pnas.1510133112>.

Kosaka, T. & Hama, K., 1986. Three-dimensional structure of astrocytes in the rat dentate gyrus. *Journal of Comparative Neurology*, 249(2), pp.242–260.

Lancaster, M.A. & Knoblich, J.A., 2014. Generation of cerebral organoids from human pluripotent stem cells. *Nature Protocols*, 9(10), pp.2329–2340.

Maglione, M. & Sigrist, S.J., 2013. Seeing the forest tree by tree: Super-resolution light microscopy meets the neurosciences. *Nature Neuroscience*, 16(7), pp.790–797. Available at: <http://dx.doi.org/10.1038/nn.3403>.

Micheva, K.D. & Smith, S.J., 2007. Array Tomography: A New Tool for Imaging the Molecular Architecture and Ultrastructure of Neural Circuits. *Neuron*, 55(1), pp.25–36.

Murray, E. et al., 2015. Simple, Scalable Proteomic Imaging for High-Dimensional Profiling of Intact Systems. *Cell*, 163(6), pp.1500–1514. Available at: <http://dx.doi.org/10.1016/j.cell.2015.11.025>.

Oh, S.W. et al., 2014. A mesoscale connectome of the mouse brain. *Nature*, 508(7495), pp.207–214. Available at: <http://dx.doi.org/10.1038/nature13186>.

Phizicky, E. et al., 2003. Protein analysis on a proteomic scale. *Nature*, 422(6928), pp.208–215.

Puchtler, H. & Meloan, S.N., 1985. On the chemistry of formaldehyde fixation and its effects on immunohistochemical reactions. *Histochemistry*, 82(3), pp.201–204.

Ragan, T. et al., 2012. Serial two-photon tomography for automated ex vivo mouse brain imaging. *Nature Methods*, 9(3), pp.255–258.

Richardson, D.S. & Lichtman, J.W., 2015. Clarifying Tissue Clearing. *Cell*, 162(2), pp.246–257.

Rust, M.J., Bates, M. & Zhuang, X., 2006. Sub-diffraction-limit imaging by stochastic optical reconstruction microscopy (STORM). *Springer Series in Chemical Physics*, 7(10),

p.2006.

Schindelin, J. et al., 2012. Fiji: An open-source platform for biological-image analysis. *Nature Methods*, 9(7), pp.676–682.

Sung, H.W. et al., 1996. Cross-linking characteristics of biological tissues fixed with monofunctional or multifunctional epoxy compounds. *Biomaterials*, 17(14), pp.1405–1410.

Tomer, R. et al., 2014. Advanced CLARITY for rapid and high-resolution imaging of intact tissues. *Nature Protocols*, 9(7), pp.1682–1697.

Uhlen, M. et al., 2010. Towards a knowledge-based Human Protein Atlas. *Nature Biotechnology*, 28(12), pp.1248–1250.

Uhlen, M. & Ponten, F., 2005. Antibody-based proteomics for human tissue profiling. *Molecular and Cellular Proteomics*, 4(4), pp.384–393.

White, J.G. et al., 1986. The structure of the nervous system of the nematode *Caenorhabditis Elegans*. *Phil. Trans. R. Soc. Lond.*, 340, pp.1–340.

Yuan, A. et al., 2015. Neurofilament subunits are integral components of synapses and modulate neurotransmission and behavior in vivo. *Molecular Psychiatry*, 20(8), pp.986–994.

Chapter 3

Ultrafast immunostaining of organ-scale tissues for scalable proteomic phenotyping

Dae Hee Yun*, Young-Gyun Park*, Jae Hun Cho*, Lee Kamentsky, Nicholas B. Evans, Alex Albanese, Katherine Xie, **Justin Swaney**, Chang Ho Sohn, Yuxuan Tian, Qiangge Zhang, Gabi Drummond, Webster Guan, Nicholas DiNapoli, Heejin Choi, Hae-Yoon Jung, Luzdary Ruelas, Guoping Feng, Kwanghun Chung¹

3.1 Abstract

Studying the function and dysfunction of complex biological systems necessitates comprehensive understanding of individual cells. Advancements in three-dimensional (3D) tissue processing and imaging modalities have enabled rapid visualization and phenotyping of cells in their spatial context. However, system-wide interrogation of individual cells within large intact tissue remains challenging, low throughput, and error-prone owing to the lack of robust labeling technologies. Here we introduce a rapid, versatile, and scalable method, eFLASH, that enables complete and uniform labeling of organ-scale tissue within one day. eFLASH dynamically modulates chemical transport and reaction kinetics to establish system-wide uniform labeling conditions throughout the day-long labeling period. This unique approach enables the same protocol to be compatible with a wide range of tissue types and probes, enabling combinatorial molecular phenotyping across different organs and species. We applied eFLASH to generate quantitative maps of various cell types in mouse brains. We also demonstrated multidimensional cell profiling in a mar-

¹* indicates co-first authorship.

moset brain block. We envision that eFLASH will spur holistic phenotyping of emerging animal models and disease models to help assess their functions and dysfunctions.

3.2 Introduction

System-wide analysis of cell types is essential for understanding how complex cellular interactions give rise to various functions. Extensive efforts have been made towards characterizing cells, particularly in the brain, through various lenses (e.g., genomics, transcriptomics, proteomics, connectomics) and have established invaluable databases with new insights (Sharma et al. 2015; Hawrylycz et al. 2012; Miller et al. 2014; Wang et al. 2018; Chen et al. 2015; Habib et al. 2016). Among these approaches, proteomic imaging has distinct advantages. Mapping spatial distribution of proteins, the major functional substrate with distinct subcellular localization at single molecule precision, can provide rich molecular, functional, as well as morphological details of cells. Furthermore, visualizing endogenous proteins with highly specific antibodies does not require genetic manipulation or invasive *in vivo* surgery, and thus it is applicable to any species or tissue type including non-human primates and human clinical samples (Belle et al. 2017).

When combined with intact organ transformation and clearing techniques, proteomic phenotyping can provide multiscale information, ranging from brain-wide cell distribution patterns to molecular and morphological details of individual cells without information loss caused by subsampling or 2D analysis (Chung & Deisseroth 2013; Renier et al. 2014; Luo et al. 2018). However, scaling immunolabeling to large-scale tissues and higher species remains a major challenge in biology. Passive transport of large macromolecules such as antibodies into intact tissues can take weeks to months (Chung et al. 2013). Antibody penetration can be further delayed or even blocked by target proteins with high expression levels, causing probe depletion and incomplete staining. Using excessive amounts of antibodies can improve probe penetration, but it becomes prohibitively expensive and thus unscalable. In conventional passive labeling approaches, experimental parameters for labeling (e.g., incubation time, probe amount) are highly dependent on sample properties (e.g., tissue type, size, shape) and target protein properties (e.g., expression level, distribution patterns), which are widely different between applications. Therefore, each experiment requires laborious, costly, and time-consuming optimization. The outcome of passive labeling is in many cases highly uneven with saturated labeling of outer regions and weak or no labeling of the core. Such non-uniform and incomplete labeling can prohibit automated analysis and cause systematic error. These challenges together have limited the power of 3D proteomic phenotyping to small tissues or a small number of established applications.

Here we present an integrated pipeline for holistic, rapid, scalable proteomic phenotyping of intact organs. To establish the pipeline, we developed an ultrafast and versatile immunolabeling technology, termed eFLASH (electrophoretically driven Fast Labeling using Affinity Sweeping in Hydrogel), which enables complete and uniform labeling of various types of tissues (mouse brain and intestine, human iPSC-derived cerebral organoid, and marmoset brain block) using a wide selection of antibodies (targeting structural, molecular, and neuronal activity markers) with a universal 1-day protocol. Combined with intact tissue processing and analysis techniques, we performed organ-wide quantification of various proteins at cellular resolution in mouse brains. We further demonstrated the power of 3D protein-based cell phenotyping by characterizing neural sub-types based on their 3D location, protein expression level, cell body size, and dendritic morphology in a fully integrated manner.

3.3 Results

3.3.1 eFLASH mechanism

Our organ-wide molecular phenotyping framework consists of four major components: (1) intact tissue preservation via SHIELD, (2) volumetric labeling with eFLASH, (3) light-sheet imaging, and (4) automated 3D image analysis (Fig. 3.1a). The pipeline begins with robust preservation of biological tissue with SHIELD, which is a polyepoxide-based tissue fixation method that protects biomolecules and tissue architecture (Park et al. 2019). After rapid delipidation of the SHIELD-preserved tissues using stochastic electrotransport (SE) (S.-Y. Kim et al. 2015), we immunolabel the intact tissues using eFLASH within just one day. The labeled samples are rapidly imaged at high-resolution using an axially swept light-sheet microscope. Finally, we analyze the resulting volumetric datasets via a suite of automated 3D image analysis algorithms to map various cell types within the tissue volume. Altogether, the pipeline enables extraction of organ-scale, single-cell-resolution data from a fresh sample within just 12 days (Fig. 3.1a).

eFLASH allows uniform immunolabeling of organ-scale tissues within a day by gradually shifting probe-target binding conditions from unfavorable to favorable while accelerating probe penetration using stochastic electrotransport (Fig. 3.1b). We discovered that bile salts, such as sodium deoxycholate (NaDC), can be used to control the labeling affinity for various antibodies in a concentration and pH dependent manner (Fig. 3.1c-d; Supplementary Fig. 1). A wide range of probes showed weak binding at high concentrations of NaDC and basic pH, but strong binding at low concentration of NaDC and neutral pH. These results indicate that labeling conditions can be gradually shifted from unfavorable

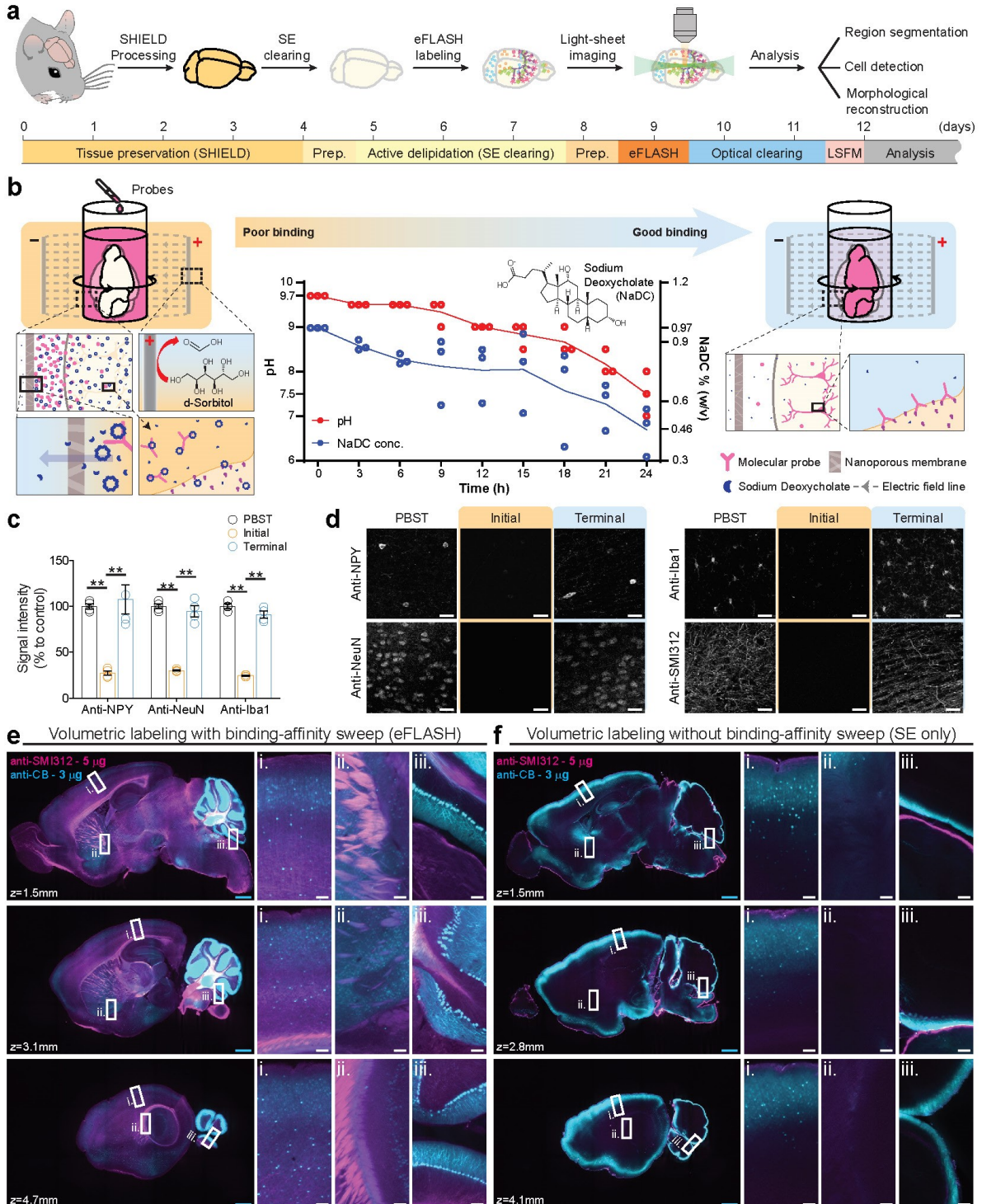


Figure 3.1: eFLASH enables rapid, uniform, and cost-efficient labeling of organ-scale tissues. (a) High-throughput pipeline for organ-wide molecular mapping at single cell resolution. The pipeline can generate high-resolution and multidimensional data from mouse brains within 12 days. SE, stochastic electrotransport; Prep, preparation; LSFM, light-sheet fluorescence microscopy. (b) eFLASH. The pH and sodium deoxycholate (NaDC) concentration of the labeling solution are gradually reduced to sweep the molecular probes' binding affinity from unfavorable to favorable in the context of SE. Electrocatalytic oxidation of d-sorbitol on the anode surface generates acidic components that lower pH. NaDC concentration of the labeling solution is reduced by the concentration gradient through the nanoporous membrane. $N = 3$ independent experiments. Individual data points and mean. (c) Comparison of immunostaining signal among PBST control, initial (unfavorable binding condition) and terminal (favorable binding condition) eFLASH buffers. $N = 4$ tissue samples. Mean \pm s.e.m.. Unpaired T-test, $^{***}P < 0.01$. Scale bar = 50 μ m. (d) Representative images used in (c).

(e-f) Comparison of antibody penetration and uniformity of staining between eFLASH and SE only. Optical sections of mouse hemispheres at different depths are shown. The same amounts of antibodies were used for both experiments. Z-depth indicates the distance of optical sections from the mid-sagittal planes. Display ranges of images are 200-5,000 (cyan) and 100-500 (magenta) except e-i: 200-3,000 (cyan); e-iii: 200/10,000 (cyan) and 100/1,000 (magenta); f-i: 200/10,000 (cyan); f-iii: 200/20,000 (cyan) and 100/1,000 (magenta). Scale bars = 1 mm (cyan) or 100 μ m (white).

to favorable by simultaneously sweeping pH (basic to neutral) and NaDC concentration (high to low).

To achieve a gradual pH sweep in an automated manner, we took advantage of electrochemical reactions that naturally occur under SE. Electrocatalytic oxidation of D-sorbitol produces acidic byproducts such as formic acid (Proen  a et al. 1997). By adding D-sorbitol to a pH 9.5 buffer and letting it decompose by electro-oxidation under SE, we were able to gradually sweep pH from 9.5 to 7.5 over the course of one day (Fig. 3.1b, Supplementary Fig. 2).

Concentration of NaDC within the labeling solution was also swept in an automated manner using the concentration gradient established across a nanoporous membrane (Fig. 3.1b). The membrane, which separates the labeling solution and the outer solution, ensures that both molecular probes and large NaDC micelles remain within the labeling solution; however, it is permeable to NaDC monomers, small NaDC aggregates, and the rest of the buffer components. The initial concentration of 1% (w/v) NaDC within the labeling solution slowly decreases as the monomers travel down the concentration gradient to the outer solution, which contains 0.2% (w/v) of NaDC (Fig. 3.1b). We confirmed that the terminal buffer after pH and NaDC concentration shift allows strong antibody staining (Fig. 3.1c-d).

This progressive change in binding condition enables the probes to first penetrate deep into the tissue without being depleted and then increasingly bind to targets globally as the buffer composition gradually changes. This approach ensures uniform labeling of entire volumes regardless of the density and distribution pattern of the targets, specific binding kinetics of various antibodies, and the amount of antibody used. With eFLASH, even when using a minute amount of antibody for labeling highly dense targets (3 μ g of antibody for calbindin and 5 μ g of antibody for pan-axonal marker SMI312), high-quality uniform labeling could be achieved in a mouse brain hemisphere (Fig. 3.1e); however, without affinity-sweep, the small amount of antibody was quickly depleted on the surface before the core of the tissue could be labeled despite the increased transport speed provided by SE (Fig. 3.1f, Supplementary Video 1). These results indicate that eFLASH enables rapid, complete, and uniform immunolabeling of organ-scale tissues without the use of excessive amounts of molecular probes.

3.3.2 Universal applicability of eFLASH

The affinity sweeping mechanism in eFLASH renders the technique insensitive to tissue type, size, or geometry. eFLASH is also insensitive to probe types because the sweeping range is wide enough to modulate binding affinities of many antibodies and other commonly used molecular probes. Therefore, the same operational parameters of eFLASH can be used for many applications without laborious and costly optimization. We found that a single protocol with the same parameters (e.g. voltage, pH, running time, chemical concentrations) is capable of uniformly labeling cerebral organoid, mouse intestine, mouse brain hemisphere, as well as marmoset brain block with various combinations of antibodies, allowing visualization of multiple proteins within a single sample (Fig. 3.2a-d, Supplementary video 2-3).

The same 1-day protocol was compatible with a wide range of antibodies harboring different binding affinities and target densities (Fig. 3.2e). eFLASH successfully labeled targets for various cell types (PV, CB, CR, NPY, SST, TH, TPH2, ChAT, NeuN, GFAP, Iba1), neuronal structure (SMI-312), and a neuronal activity marker (cFos) in intact mouse hemispheres (Fig. 3.2e, Supplementary video 4-5). The same eFLASH protocol was also compatible with lectin and Syto16, which are chemical probes that label blood vessels and nuclei, respectively. Together, these results suggest that eFLASH is a universal platform compatible with a wide range of tissue-types and molecular probes.

3.3.3 A quantitative, brain-wide cell type mapping with eFLASH

eFLASH, combined with light-sheet microscopy, enables true volumetric quantification of protein expression at cellular resolution. eFLASH-stained mouse brain hemispheres were rapidly imaged using an axially swept light-sheet microscope at near-isometric resolution of $1.8 \mu\text{m} \times 1.8 \mu\text{m} \times 2 \mu\text{m}$ within 45 minutes per channel. Because the sample was processed and imaged as a whole without sectioning, the resulting volumetric data is an exhaustive representation of the sample that does not suffer from sampling errors and does not require interpolation or extrapolation to acquire brain-wide or region-specific cell counts. In addition, the multiplexed labeling capability of eFLASH allows analysis of cells co-expressing multiple proteins of interest with relative ease and flexibility compared to genetic labeling approaches. Currently, labeling up to four distinct targets is possible through transgenic labeling approaches (Gaire et al. 2018); however, developing transgenic mouse lines for each new combination of targets can be time consuming (Liu 2013).

To demonstrate the value of holistic labeling with eFLASH, we established an image

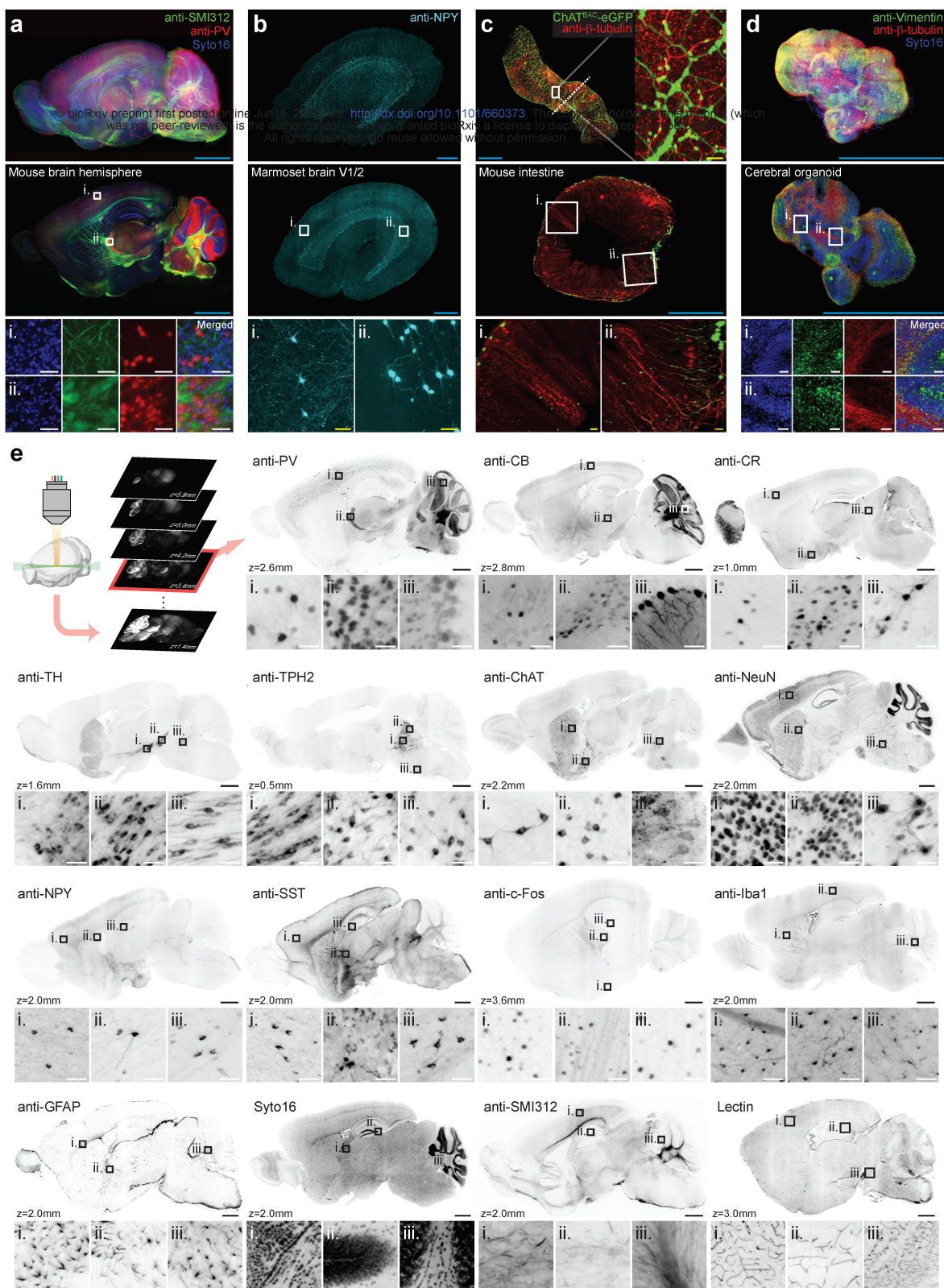


Figure 3.2: Single eFLASH protocol enables complete and uniform staining of various tissue types with a wide range of molecular probes.

(a-d) Different types of tissue labeled with eFLASH. Full volume renderings (top row) and optical sections (middle and bottom row). Scale bars = 2 mm (cyan), 200 μ m (yellow), and 50 μ m (white). (a) An adult mouse brain hemisphere labeled with syto16 (blue), anti-SMI312 antibody (green), and anti-PV antibody (red). (b) A marmoset visual cortical block labeled with anti-NPY antibody (cyan). (c) ChATBAC-eGFP mouse intestine labeled with anti- β -tubulin (red). (d) Cerebral organoid labeled with syto16 (blue), anti-Vimentin antibody (green), and anti- β -tubulin antibody (red). (e) Optical sections from whole adult mouse hemispheres labeled with indicated antibodies or molecular probes. Z-depth indicates the distance of the optical sections from mid-sagittal planes. PV, parvalbumin; CB, calbindin; CR, calretinin; TH, tyrosine hydroxylase; TPH2, tryptophan hydroxylase 2; ChAT, choline acetyltransferase; NeuN, neuronal nuclear antigen; NPY, neuropeptide Y; SST, somatostatin; Iba1, ionized calcium binding adaptor molecule 1. Scale bars = 1 mm (black) and 50 μ m (white).

analysis pipeline for atlas alignment, brain region segmentation, and cell detection for generating a quantitative map of various proteins. Volumetric images were automatically aligned to an atlas (Oh et al. 2014) by linear and non-linear transformations based on Elastix (Klein et al. 2010) then manually refined (Swaney et al. 2019). Each aligned 3D image volume was indexed to approximately 580 brain regions with 7 hierarchies. Brain-wide quantification of immunolabeled cells was accomplished using machine learning algorithms that were trained to identify features of individual cell-types (Supplementary Fig. 3). Specifically, Random Forest (Breiman 2001) was applied after blob detection and principal component analysis (PCA). Detection performance was validated against manual ground-truth annotations of relevant brain regions that are known to express each cell type. Our cell detection pipeline achieved an f-score of higher than 90% for cortical regions and over 80% for subcortical brain regions for all tested cell-type markers. Using this pipeline, we were able to construct quantitative mouse brain atlases for multiple cell type defining makers, including CR, NPY, SST, TH, TPH2, and PV (Fig. 3.3a-c, Supplementary video 6).

The probe-insensitive nature of eFLASH enables co-labeling of multiple cell-types with any combinations. We performed simultaneous labeling of neuropeptide Y and somatostatin which are known to be co-expressed in a subset of GABAergic interneurons (Fu & Pol 2007; Figueredo-Cardenas et al. 1996; Hendry et al. 1984) and of Tyrosine Hydroxylase and Tryptophan Hydroxylase 2 which are cell-type-specific markers for dopaminergic and serotonergic neurons, respectively, that are not generally known to overlap. In the case of NPY and SST, we mapped NPY+/SST-, NPY-/SST+, and NPY+/SST+ cells (Fig. 3.3d-f). We found the highest density of NPY+ cells at layer 2 or 3 of the cerebral cortices (Fig. 3.3c), whereas SST+ cells showed the highest density at layer 4 or 5 in majority of the cortices (Rudy et al. 2011) (Fig. 3.3c) Interestingly, the highest density of cells that were co-positive for NPY and SST was seen in layer 5 or 6 (Fig. 3.3f). In a brain-wide average, $16 \pm 4\%$ of NPY and $7 \pm 5\%$ of SST-expressing cortical cells were identified NPY+ / SST+ co-positive. In the case of TH and TPH2, we checked every TH+ and TPH2+ cells detected throughout the brain hemisphere and found that no cells

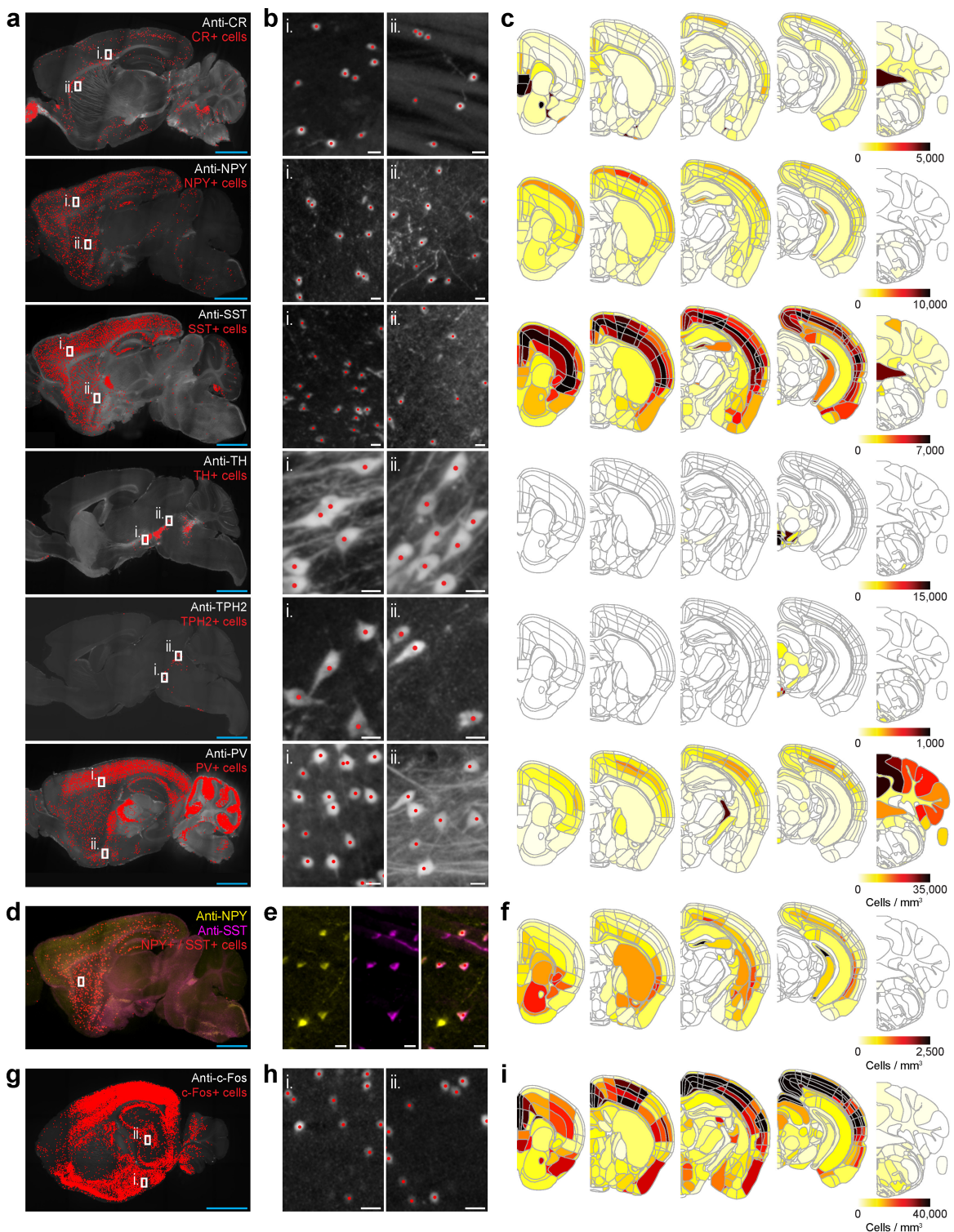


Figure 3.3: Quantitative brain-wide cell type mapping.

(a) Optical section images of whole mouse hemisphere datasets. Adult mouse hemispheres were eFLASH-labeled with indicated antibodies and imaged. Automatically detected cells are marked with red dots. (b) Zoom-in views of a. (c) Representative images of 3D brain-wide cell type density heatmaps. See Supplementary video 6 for PV detection and heat map. (d) An optical section image of a whole mouse hemisphere colabeled with anti-NPY antibody (yellow) and anti-SST antibody (magenta). NPY and SST copositive cells are marked with red dots. (e) Zoom-in views of d. (f) Representative images of the 3D heatmap of the co-positive cells. (g) An optical section of a whole mouse hemisphere labeled with anti-c-Fos antibody. The mouse experienced contextual fear conditioning 90 minutes before sacrifice. (h) Zoom-in views of g. (i) Representative images of the 3D heatmap of c-Fos+ cells. Scale bars = 2 mm (cyan) and 20 μ m (white).

were positive for both markers.

Finally, in addition to labeling cell-type defining proteins, brain-wide labeling of Immediate Early Genes (IEGs) such as c-Fos has been demonstrated as a powerful proxy for measuring neuronal activation (Renier et al. 2016; Yongsoo Kim et al. 2015). We stained the brain of a mouse that experienced contextual fear conditioning 90 minutes before sacrifice with anti-cFos antibody and mapped its distribution (Fig. 3.3g-i). Examination of the dataset showed robust anti-c-Fos signal in hippocampus and amygdala areas, which are known to show increased activity upon contextual fear conditioning (Cho et al. 2017). Combined, these results suggest that eFLASH-mediated immunolabeling can facilitate brain-wide quantification of protein expression at a cellular level in a high throughput and flexible manner.

3.3.4 Brain-wide comparison of genetic and protein-based cell type labeling

Expression of genetically encoded fluorescent proteins have revolutionized biological labeling and imaging (Giepmans et al. 2006), and ongoing developments in transgenic methodology offer powerful ways to study organ-wide gene expression (Gong et al. 2003; Kim et al. 2017; Zhang et al. 2017). However, the level of fluorescent protein expression is linked to transcription activity rather than the level of expression of mRNA or proteins, requiring careful and nuanced interpretation of data (Huang et al. 2014). Additionally, several studies have reported on the importance of post-transcriptional processes that can often cause the quantities of mRNA and proteins to correlate poorly (Vogel & Marcotte 2012), emphasizing the need for protein expression analysis.

Discrepancy between transgenic labeling and immunohistochemical labeling is widely recognized, and there is a constant concerted effort to improve upon existing transgenic mouse lines for common targets (Tallini et al. 2006; Li et al. 2017; Madisen et al. 2010). To compare genetic labeling and eFLASH-mediated cell-type phenotyping approaches, we utilized transgenic mouse lines with two widely used transgene approaches: Cre-LoxP

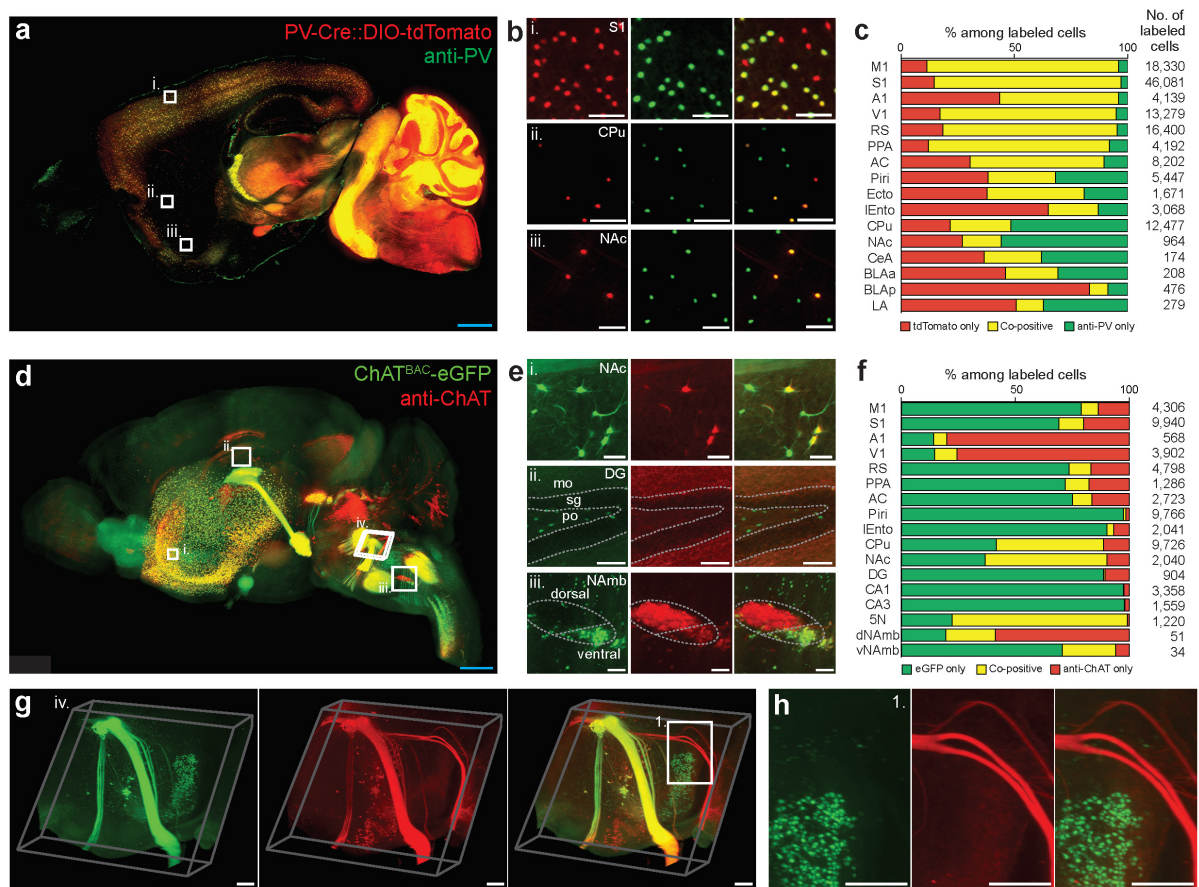


Figure 3.4: Brain-wide comparison of genetic cell-type labeling and eFLASH-driven protein-based cell type labeling. (a) An optical section of a 3D dataset from a PV-Cre and DIO-tdTomato dual transgenic mouse hemisphere stained with anti-PV antibody. (b) Zoom-in images of a. (c) A percentage plot for tdTomato-only (red), anti-PV-only (green), and tdTomato and anti-PV copositive cells (yellow) among all the labeled cells in individual representative brain regions. (d) A 3D rendering of a ChATBAC-eGFP mouse brain stained with anti-ChAT antibody. (e) Zoom-in views of d. (f) A percentage plot for eGFP-only (green), anti-ChAT-only (red), and eGFP and anti-ChAT co-positive cells (yellow) among all the labeled cells in individual representative brain regions. (g) Zoom-in view of d. (h) Zoom-in view of g. M1, primary motor cortex; S1, primary somatosensory cortex; A1, primary auditory cortex; V1, primary visual cortex; RSA, retrosplenial cortex; PPA, posterior parietal association cortex; AC, anterior cingulate cortex; Piri, piriform cortex; Ecto, entorhinal cortex; lEnto, lateral entorhinal cortex; CPu, caudoputamen; NAc, nucleus accumbens; CeA, central amygdala; BLAa, basolateral amygdala, anterior part; BLAp, basolateral amygdala, posterior part; LA, lateral amygdala; DG, dentate gyrus; mo, dentate gyrus, molecular layer; sg, dentate gyrus, granule cell layer; po, dentate gyrus, polymorph layer; CA1, hippocampal CA1; CA3, hippocampal CA3; 5N, motor nucleus of trigeminal; dNAmB, nucleus ambiguus, dorsal part; vNAmB, nucleus ambiguus, ventral part. Scale bars = 1 mm (blue), 200 µm (white).

and BAC transgene (Muzumdar et al. 2006); Livet et al. (2007); Valjent et al. (2009)]. First, we eFLASH-stained a hemisphere of a PV-Cre::DIO-tdTomato double transgenic mouse with anti-PV antibody (Fig. 3.4a). We performed the brain-wide quantitative analysis on tdTomato and anti-PV signals, and revealed substantial discrepancies between two labeling approaches, where the level of mismatch was highly heterogeneous among brain regions (Fig. 3.4b-c, Supplementary video 7). For example, in contrast to faithful tdTomato labeling of PV+ neurons in primary motor and primary somatosensory cortices (88% and 85% of tdTomato+ cells were also PV+), a substantial portion of tdTomato cells showed undetectable amounts of PV protein in some cortical (e.g., 56% and 75% in the case of piriform and lateral entorhinal cortex) and subcortical (45% in caudate putamen; 62% in nucleus accumbens) areas. Furthermore, we found PV+ populations were not covered by the genetic labeling. For example, 66% and 77% of PV+ cells do not express tdTomato in CPu and NAc, respectively (Fig. 3.4b-c).

Next, we compared genetic and protein-based labeling of choline acetyltransferase (ChAT). eGFP expression via BAC transgene was highly divergent from the ChAT+ immunoreactivity pattern (Fig. 3.4d-h, Supplementary video 8). For example, only 9% and 14% of eGFP+ cells were also ChAT+ in M1 and S1 cortex. In the hippocampal CA1 and CA3, only 0.2% and 0.3% of eGFP+ cells showed detectable levels of ChAT immunoreactivity. Further, large populations of ChAT+ cells without eGFP expression were evident, especially in primary auditory and visual cortices (93%, 89%) (Fig. 3.4f). These discrepancies were heterogeneous even within the same brain region. Most ChAT+ cells were also eGFP+ in Nucleus ambiguus ventral part (80%), however, in its dorsal counterpart, only 26% of ChAT+ cells were colocalized with eGFP+ (Fig. 3.4e-iii). 3D visualization of the hemisphere also revealed labeling mismatch between fiber bundles. In the brain stem, we found a fiber bundle composed of ChAT+ axons without eGFP signals (Fig. 3.4g,h). These results suggest that eFLASH enables brain-wide analysis of transgenic labeling patterns and their validation by allowing simultaneous visualization of genetically expressed fluorescent proteins and immunolabeling signal within the same sample.

3.3.5 Multidimensional single-cell analysis of marmoset visual cortex

Common marmoset (*Callithrix jacchus*), a small New World primate, has emerged as a powerful model for neuroscience research (Miller et al. 2016). Their rapid reproduction cycles and compatibility with existing genetic engineering tools renders them a promising model for studying various brain disorders. Holistic cell-level phenotyping of the marmoset brain, however, remains challenging owing to the limited quality and availability of transgenic lines, significantly higher cost and larger brain size compared to rodent

models.

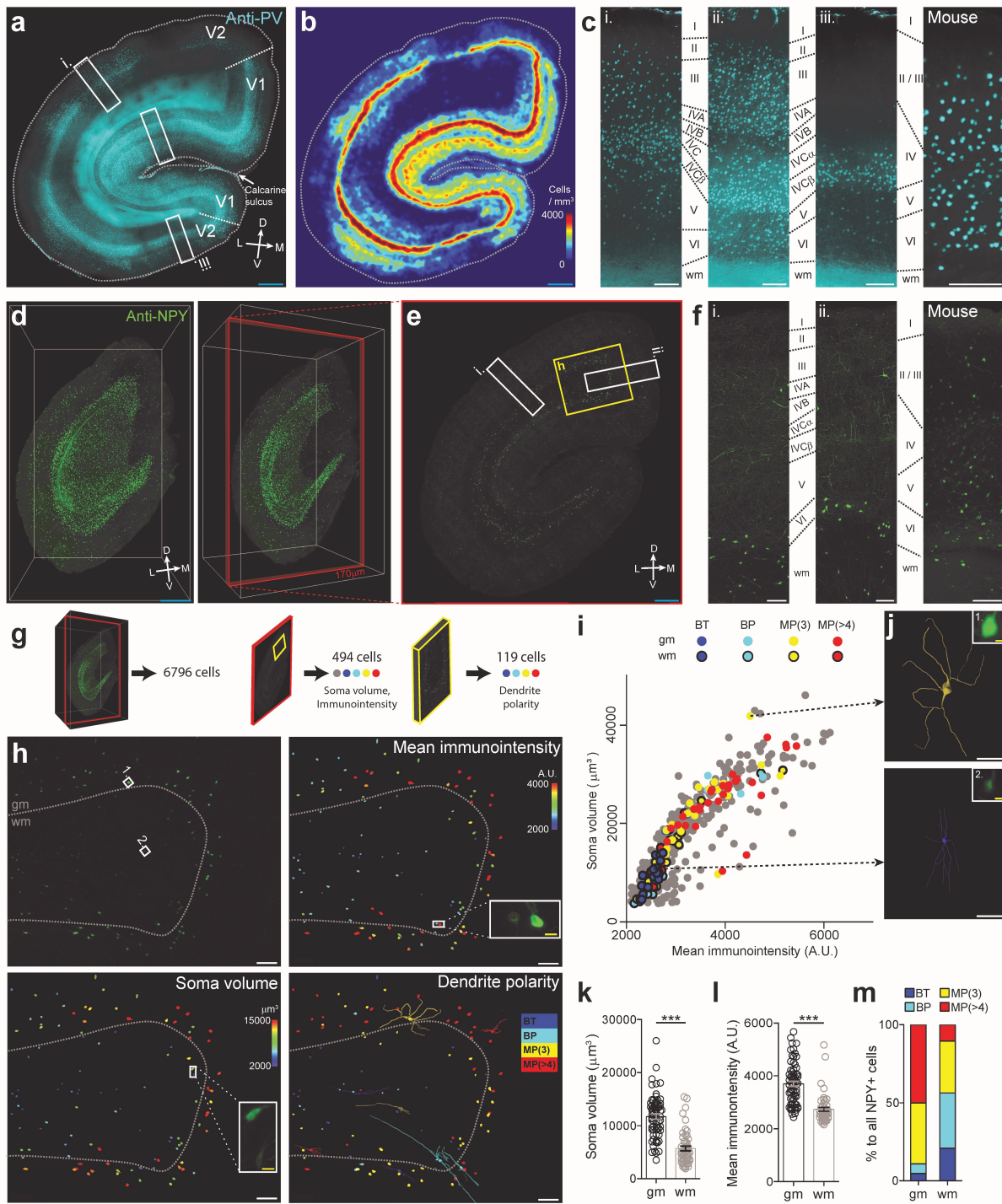


Figure 3.5: Multidimensional analysis of an eFLASH-stained marmoset brain block at single cell resolution.

Protein-based cellular phenotyping using eFLASH and SHIELD can be advantageous for higher model systems, including primates, where genetic manipulation remains challenging (He & Huang 2018; Izpisua Belmonte et al. 2015). Moreover, the multiplexing capability of this approach allows simultaneous mapping of various molecular and cell-type markers within the same brain tissue, which not only increases the dimensionality

(a) A marmoset visual cortical tissue (5 mm x 5 mm x 8 mm) was eFLASH-stained with anti-PV antibody. An optical section of the 3D block image is shown. D, dorsal; V, ventral; L, lateral; M, medial. (b) PV+ cell density analysis shown as heat map. See Supplementary video 9 for volumetric heat map. (c) Inter-layer distribution of PV+ cell in marmoset (i-iii) and mouse visual cortex (right). wm, white matter. Zoomed regions indicated on panel a. (d) The same marmoset brain block was destained then re-stained with anti-NPY antibody with eFLASH. 3D volume renderings from two different perspectives. (e) A coronal optical section from the 3D data in d. (f) Inter-layer distribution of NPY+ cells in marmoset (i-ii) and mouse visual cortex (right). Zoomed regions indicated on panel e. (g) 6796 cells were detected in the 3D volume. Soma volume and mean immunointensity analysis was performed on 494 cells within the selected 170 μm -thick optical section (red). Dendrite polarity analysis was performed on 119 cells within the indicated volume (yellow). (h) An intensity projection image of a cortical fold region indicated on panel e (upper left). All cells within this volume were analyzed for their soma volume (lower left), mean immunointensity (upper right), and dendrite polarity with dendrite traces shown for 8 representative neurons (lower right). gm, gray matter; A.U., arbitrary unit; BT, bitufted cell; BP, bipolar cell; MP (3), multipolar cell with 3 primary dendrites; MP (>4), multipolar cell with 4 or more primary dendrites. (i) Annotated NPY+ cells plotted based on their mean immunointensity and soma volume. Total cells plotted, N = 494. (j) 3D reconstruction of dendrites of gray (upper) and white matter NPY+ cell (lower) in h. Insets indicate soma image of each cell. (k-l) Soma volume (k) and mean immunointensity (l) of gray and white matter NPY+ cells in h. N = 67 and 52 for gray and white matter cells, respectively. (m) Percentages of NPY+ cells categorized by their dendrite polarity. Mann-Whitney test, P < 0.05, P < 0.01, P < 0.005. Mean \pm s.e.m.. Scale bars = 1 mm (blue), 200 μm (white), 20 μm (yellow).

of integrated phenotypic analysis, but also decreases the number of animals required for a study and consequently the cost.

To test this idea, we applied eFLASH and SHIELD to characterize cells in an intact marmoset brain block of visual cortex (5 mm x 5 mm x 8 mm). First, we eFLASH-stained the SHIELD-preserved sample with anti-PV antibody. From the holistic visualization and detection of PV+ cells in the sample (Fig. 3.5a), we found that the inter-layer distribution of PV+ cell is heterogeneous among parts of the visual cortex. The density of PV+ cells was higher in the area facing the calcarine sulcus compared to the other area of the visual cortical block (1770.3 ± 56.4 vs 979.0 ± 33.4 cells per mm^3 , unpaired T-test, $P < 0.0005$, $N = 4$ of 120 μm -thick optical sections) (Fig. 3.5b-c, Supplementary video 9). We also observed that several cortical areas were devoid of PV+ neurons (Fig. 3.5a-c). Furthermore, we observed that inter-layer distribution patterns of PV+ cells differed between mouse and marmoset visual cortex (Fig. 3.5c). After mapping PV+ cells, we destained the same marmoset brain block and re-stained it with anti-NPY antibody using eFLASH. We found that NPY+ cells are mostly localized in layer 6 and white matter of the marmoset visual cortex, which was in contrast with mouse visual cortex that showed a more uniform NPY+ cell distribution across the cortical layers (Fig. 3.5d-f).

Immunostaining can provide access to cellular morphology without genetic labeling or dye injections because many proteins are distributed or transported to cytoplasm and subcellular compartments. Using eFLASH-mediated volume-wide immunolabeling, we may be able to characterize both morphological and molecular details of individual cells throughout intact tissue volumes. To demonstrate this possibility, we performed deep

analysis of individual NPY+ cells in a cortical fold sub-volume. From the automatically detected 6796 NPY+ cells in the volume, we quantified the soma volume and mean immunointensity of 494 cells, and dendrite polarity of 119 cells (Fig. 3.5g-i). Analysis of dendritic morphology of individual NPY+ cells led us to classify the cells into separate categories based on previously established descriptions of GABAergic interneurons: bitufted, bipolar or multipolar (Ascoli et al. 2008) (Fig 3.5h, Supplementary Fig 4.) Compared to NPY+ cells in white matter, NPY+ cells in gray matter have soma with larger volume and higher mean fluorescent signal intensity (Fig. 3.5k-l), suggesting higher intracellular concentration of NPY protein (Chung et al. 2011; Watanabe et al. 1996). We also found that most gray matter NPY+ cells are multipolar cells, whereas most NPY+ cells in white matter were bitufted or bipolar cells (Fig. 3.5h,j,m; Supplementary video 10). Together, these results demonstrate that complete and uniform immunolabeling of large-scale intact tissues with eFLASH enables high-dimensional phenotyping of individual cells even on model animals with limited access to genetic tools.

3.4 Discussion

In this study, we developed a rapid, versatile, and scalable immunolabeling technology, eFLASH, that enables complete and uniform immunolabeling of organ-scale tissues within one day for protein-based high dimensional cellular phenotyping. The universal 1-day protocol based on the gradual sweeping of probe-target binding affinity allows labeling of various markers simultaneously for disparate tissue types. Combined with the volumetric imaging and analysis pipeline, eFLASH enables 3D visualization and multi-dimensional phenotyping of molecular markers in large intact tissues with single-cell-resolution.

eFLASH is rationally designed to address the main challenge in scaling molecular labeling to organ-scale samples: the drastic mismatch between probe diffusion time scale and probe-target reaction time scale. Probe-target binding reaction is orders of magnitude faster than probe diffusion. The diffusion timescale increases quadratically with the thickness of the sample, whereas probes rapidly bind to targets as soon as they encounter. If the density of the target molecule is high, which is the case for many of protein targets, probes cannot penetrate deeper into the tissue until they saturate all target molecules in their path. This means that uniform and complete labeling of intact tissue is not possible without using a large amount of probes, reducing the tissue size, or reducing the density of antigens.

Transport of electromobile molecules such as antibodies can be expedited using stochastic electrotransport. However, the probe transport time scale in SE is still much longer than the reaction time scale. Applying a higher electric field can further increase trans-

port speed, but Joule heating can cause tissue damage. Therefore, it is imperative to modulate both the rate of reaction and transport simultaneously. Switching off the binding reaction allows transport of antibodies into the core of the tissue without depletion (Murray et al. 2015). Once probes reach the core of the sample, the binding reaction can be switched back on by changing the surrounding chemical environment (pH, detergent concentration). Discrete modulation of kinetics by such step-wise change, however, inevitably forms concentration gradients of chemicals (e.g., pH and NaDC) and probes inside the tissue, which causes uneven labeling. We addressed this challenge in eFLASH by slowly and gradually changing the concentration of the chemicals to ensure that the reaction condition is uniform tissue-wide throughout the day-long labeling period.

eFLASH is a robust process that offers considerable experimental flexibility. Repeated staining of the same tissue is possible with eFLASH, allowing multiple interrogations of precious samples as demonstrated with the marmoset brain block (Fig. 3.5). eFLASH can also be used to immunolabel the organs of transgenic mice expressing fluorescent proteins, allowing simultaneous visualization of both genetic labeling and immunolabeling signals (Fig. 3.2c, Fig. 3.4). This suggests that eFLASH can be utilized for comprehensive immunohistological validation of genetic labeling, amplification of genetically labeled signal using anti-fluorescent protein antibodies, and multiplexed proteomic analysis of genetically labeled cells in intact tissues.

Recently, tissue-clearing techniques and volume imaging methods have been applied to whole organ samples to demonstrate the potential of 3D phenotyping with single-cell resolution (Murakami et al. 2018; Yang et al. 2014). Many of these studies utilized genetic labeling which provides both uniform and high signal-to-noise ratio suitable for computational analysis. However, genetic labeling is relatively inflexible when it comes to target selection, as new transgenic mouse or protocol is required for each target or each combination of targets. With eFLASH, the choice of targets and the combinations of targets is based simply on the availability of compatible molecular probes. Additionally, eFLASH performs direct immunohistological labeling of target proteins present in the tissue, allowing for simplified interpretation of resulting data. As powerful as it is, Cre-LoxP transgenesis is known to suffer from false-positive (e.g., transgene-independent CRE expression, CRE-independent recombination) and false-negative labeling (e.g., CRE mosaicism) (Heffner et al. 2012). We observed that there was a discrepancy between fluorescent protein signal and antibody labeling signal in PV-Cre:DIO-tdTomato double-transgenic mouse brain labeled with anti-PV antibody (Fig. 3.4), Reversible tissue and temporal specific control systems, (such as a tetracycline response system), and BAC transgenesis resolved some of these issues, but not all. For example, discrepancies between genetic and protein-based labeling in BAC transgenic mouse lines were observed in both previous (Von Engelhardt et al. 2007) and present studies (Fig. 3.4), and it

has been suggested that expression of BAC transgene can be affected by the presence of other transcription factors, microRNAs, or control regions of gene fragments (Matthaei 2007). We anticipate that protein-based mapping enabled by eFLASH can complement the cutting-edge genetic labeling approaches (e.g., viral labeling) for anatomical, molecular, and functional mapping of neural circuits.

Furthermore, eFLASH can facilitate studies of animal models with limited access to genetic labeling methodologies. The Common Marmoset is an emerging primate model for social behaviors with many experimental advantages (Okano & Mitra 2015; Kaiser & Feng 2015), and thus much effort has been undertaken to construct marmoset brain atlases in diverse modalities (Lin et al. 2019; Woodward et al. 2018; Liu et al. 2018). Unfortunately, numerous hurdles remain in translating existing genetic labeling approaches for rodents to marmosets. For example, germline genetic manipulation for generating transgenic primates is still difficult and expensive (Jennings et al. 2016), and long gestation and maturation period of primates as well as ethical concerns make each primate sample highly precious. Viral labeling approaches have shown the most promise; however, clear limitations exist since most enhancer elements are not defined and viral vectors have limited capacity to include large gene elements. Moreover, achieving systemic coverage of the entire brain with viral labeling also remains challenging (Matsuzaki et al. 2018). We anticipate that the scalability and flexibility of eFLASH will aid organ-wide phenotyping efforts on such model animals.

We envision that the versatility and high throughput capabilities of eFLASH will benefit numerous studies requiring system-wide yet highly detailed views of biological tissues, especially for exploratory studies comparing healthy and diseased animals or of model animals with limited access to genetic labeling strategies. Application of eFLASH will synergize greatly with advancements in biological imaging, molecular binder technologies, and computational frameworks for big data analysis (Fürth et al. 2018). Holistic, rapid, and unbiased approaches enabled by such synergistic technological advances will ultimately aid in providing a broader perspective in the study of complex biological systems.

3.5 Acknowledgements

The authors thank the entire Chung laboratory for support and discussions. We acknowledge N. Peat for contribution to chemical screening for buffer development. K.C. was supported by the Burroughs Wellcome Fund Career Awards at the Scientific Interface, Searle Scholars Program, Packard award in Science and Engineering, NARSAD Young Investigator Award, and the McKnight Foundation Technology Award. This work was supported by the JPB Foundation (PIIF and PNDRF), the NCsoft Cultural Foun-

dation, the Institute for Basic Science IBS-R026-D1, and the NIH (1-DP2-ES027992, U01MH117072).

3.6 Author Contributions

D.H.Y., Y.-G.P., J.H.C. and K.C. designed the experiments and wrote the paper with input from other authors. D.H.Y., J.H.C., and K.C. designed eFLASH protocols and systems. D.H.Y. and J.H.C. performed the volumetric labeling experiments with N.D.'s help. Y.-G.P. aided the development of the eFLASH technology by performing passive staining experiments for screening antibodies and buffers, and imaging eFLASH-labeled samples. Y.-G.P. led SHIELD-processing of all tissue samples with K.X.'s help. G.F. and K.C. initiated the marmoset brain mapping project. G.F. provided the marmoset and Q.Z. perfused the marmoset. L.K. and J.S. developed the computational pipeline with Y.-G.P., D.H.Y., W.G., and K.C.'s input. N.B.E. and Y.-G.P. performed light-sheet imaging with H.C.'s help. D.H.Y. performed active delipidation of mouse and marmoset samples with N.D.'s help. D.H.Y. performed the buffer characterization in Figure 3.1. A.A. provided and imaged the SHIELD processed cerebral organoid for Figure 2. Y.-G.P. and L.K. performed brain-wide cell-type mapping in Figure 3.3 with D.H.Y. and K.X.'s help. Y.-G.P. performed co- positivity analysis for Figure 3.4 and the multi-dimensional analysis of marmoset datasets in Figure 3.5. C.H.S. aided in antibody and fluorescent dye screening for the project. G.D. and Y.X. helped with initial manuscript preparation. Y.X., H.-Y.J., and L.R. aided in detergent and buffer screening and characterization.

3.7 Competing Interests

K.C. and D.H.Y. are co-inventors on a patent application owned by MIT covering the eFLASH technology. K.C. and J.H.C. are co-inventors on patents owned by MIT covering the SWITCH and SE technology.

3.8 Methods

3.8.1 Mice

Young adult (2-4 month) C57BL/6 mice were housed in a 12 hr light/dark cycle with unrestricted access to food and water. All experimental protocols were approved by the

MIT Institutional Animal Care and Use Committee and the Division of Comparative Medicine and were in accordance with guidelines from the National Institute of Health. The following transgenic lines were used for this study: Thy1::GFP M-line, Thy1::YFP H-line, ChAT BAC-eGFP (Jackson Stock No. 007902), PV-Cre / loxP-tdTomato (Jackson Stock No. 017320 and 007914), and Fos-CreER T2 / DIO-tdTomato (Jackson Stock No. 021882, 007914).

3.8.2 Marmoset

All animal experiments were approved by the Institutional Animal Care and Use Committee of Massachusetts Institute of Technology and were performed under the guidelines from the National Institute of Health. Adult common marmosets (2-4 years old) were housed in AAALAC-accredited facilities. The housing room was maintained at 74.0 ± 2.0 °F (23.3 ± 1.1 °C), in the relative humidity of $50 \pm 20\%$, and in a 12 hr light/dark cycle. The animals were housed in dedicated cages with enrichment devices and had unrestricted access to food and water.

For histological examinations, the animals were deeply sedated by intramuscular injection of Ketamine (20-40 mg/kg) or Alfaxalone (5-10 mg/kg), followed by intravenous injection of sodium pentobarbital (10-30 mg/kg). When pedal withdrawal reflex was eliminated and/or respiratory rate was diminished, animals were perfused transcardially with 0.5 ml 1000 IU/ml heparin and 100-200 ml cold PBS by gravity. Then the descending aorta of the animals was clamped, and a peristaltic pump was used to infuse another 200-300 ml ice-cold SHIELD perfusion solution (10%(w/v) GE38 and 4% PFA(w/v) in PBS). Brains were removed from the skulls and SHIELD-processed.

3.8.3 Organoids

Organoids were grown according to the protocol by Lancaster et al. (2014), with the addition of dual SMAD inhibition between d6 and d9 to increase neural differentiation as previously described (Mellios et al. 2018). Organoids were grown from iPSC cells (System Biosciences, #SC101A-1). After Matrigel droplet embedding, organoids were transferred to 60 mm suspension culture dishes (Corning, #430589) and placed on shaker at 75 rpm on day 16. The organoids were SHIELD-processed at day 35 (see the section “SHIELD processing”).

3.8.4 Contextual fear conditioning

Contextual fear conditioning (CFC) was conducted using a chamber with an animal shocker (Habitest, Coulbourn, MA). After 300 s exploration in the chamber, mice were shocked (0.75 mA, 2 s) and maintained in the chamber 5 minutes more. Mice were sacrificed 60 minutes after the behavioral test was ended.

3.8.5 Sodium Deoxycholate (NaDC) Concentration Measurement

Concentration of surfactants can be measured by the degree of solubilization of hydrophobic organic dyes. Above the critical micelle concentration, the amount of solubilized dye increases linearly with the increase in surfactant concentration (Tehrani-Bagha & Holmberg 2013). Degree of solubilization was measured based on light absorption using a microplate reader at 505 nm. Sufficient Orange OT dye (Sigma, 344664, powder) was added to fully saturate 200-proof ethanol at RT. 200 μ l of saturated solution was added to each of the wells in 96-well plate and allowed to fully evaporate to deposit Orange OT dye to the well surface. 100 μ l of eFLASH buffer collected at various time points were added to the prepared wells and left on an orbital shaker overnight. The well plate was centrifuged at 2000g for 10 minutes (Multifuge X1R, ThermoFisher). 50 μ l from each well was collected and added to a black 96-well plate with glass bottom for measurement using a microplate reader (EnSpire Multimode Plate Reader, PerkinElmer). NaDC concentration was calculated based on a standard curve generated using the method described above from solutions with known concentrations of NaDC (Supplementary Figure 2).

3.8.6 SHIELD Processing

Preservation of mouse brain hemispheres were carried out according to the previously published SHIELD protocol. Mice were transcardially perfused with ice-cold PBS and then with the SHIELD perfusion solution. Dissected brains or organs were incubated in the same perfusion solution at 4 °C for 48 h. Tissues were then transferred to the SHIELD-OFF solution (1X PBS containing 10% (w/v) P3PE) and incubated at 4 °C for 24 h. In the case of brain hemisphere processing, a whole brain was split into hemispheres before being incubated in the SHIELD-OFF solution. Following the SHIELD-OFF step, the organs were placed in the SHIELD-ON solution (0.1 M sodium carbonate buffer at pH 10) and incubated at 37 °C for 24 h.

Marmoset brains perfused with ice-cold PBS and then with SHIELD perfusion solution were incubated in the same perfusion solution at 4 °C for 48 h. The brain was hemisected,

transferred to the SHIELD-OFF solution, and incubated at 4 °C for 24 h. Following the SHIELD-OFF step, the hemispheres were placed in the SHIELD-ON solution and incubated at 37 °C for 24 h. Afterwards the hemispheres were transferred to PBS for washing.

Organoids were fixed in 1X PBS with 4% (w/v) PFA at RT for 30 minutes and subsequently incubated in SHIELD-OFF solution at 4°C for 48h. Samples were then incubated in SHIELD-ON solution at 37°C overnight before washing with PBS with 0.02% sodium azide at RT for at least 24 h.

3.8.7 Passive Clearing (Delipidation)

SHIELD-processed samples were delipidated before labeling or imaging. Passive delipidation was done by incubating tissues in the clearing buffer (300 mM SDS, 10 mM sodium borate, 100 mM sodium sulfite, pH 9.0). Thin slices between 100 µm and 200 µm thickness were cleared at 45 °C clearing buffer for 2-3 hrs. Mouse brain hemispheres were cleared at 45 °C for 10-14 days. Organoids were cleared at 55 °C for 36 hrs.

3.8.8 Active Clearing (Stochastic Electrotransport)

SHIELD-processed samples can also be cleared rapidly using stochastic electrotransport (SmartClear Pro, LifeCanvas Technologies). Mouse brain hemispheres were cleared at 45 °C for 3-4 days. The marmoset brain hemisphere was cut coronally into 4 blocks of 8 mm-thickness using a microtome and the blocks were cleared at 45 °C for 2 weeks.

3.8.9 Antibody Delabeling

Imaged SHIELD tissue was first equilibrated with the clearing buffer (200 mM SDS, pH 9.5) at 37 °C overnight. Afterwards the sample was moved to a separate falcon tube with 50 mL of clearing buffer that was preheated to 80 °C and kept on a heated shaker maintained at 80 °C for 1 h. Afterwards, the solution was exchanged with fresh clearing buffer at RT and the sample was incubated on an orbital shaker at 37 °C overnight. The sample was washed using PBS with multiple solution exchanges for one day to thoroughly wash out SDS.

3.8.10 Passive Immunohistochemistry

Immunohistochemistry was performed on 100 μm - or 200 μm -thick mouse or marmoset brain tissue sections. Staining was performed on 24 or 48 well plates with primary antibodies (per recommended dilution from each vendors) and with dye-conjugated Fc-specific Fab fragments (3:1 molar ratio between Fab fragments and the primary antibody, Jackson Immunoresearch) for 1 day at RT in PBS with 0.1% Triton-X100. Similar protocols were used to characterize antibody binding performance in several different buffers: PBS with 0.1% NaDC, PBS with 1% NaDC, eFLASH initial buffer (240 mM Tris, 160 mM CAPS, 20% w/v D-sorbitol, 0.9% w/v NaDC, pH 9.6), and eFLASH terminal buffer (buffer retrieved from the eFLASH staining device after 24 h, pH 7.4).

3.8.11 eFLASH Protocol

Volumetric immunolabeling with eFLASH was carried out with a device described in Kim et al. (2015). Experiments were carried out with two buffers. The main buffer (240 mM Tris, 160 mM CAPS, 20% (w/v) D-sorbitol, 0.2% (w/v) NaDC) is a circulation solution that allows conduction of electricity. The sample buffer (240 mM Tris, 160 mM CAPS, 20% (w/v) D-sorbitol, 0.9% (w/v) NaDC) is used to fill the sample cup along with the tissue and antibodies. 300 mL of a booster buffer (20% w/v D-sorbitol, 60 mM Boric Acid) was added to the main buffer at 20 h after the start of the experiment to achieve the desired pH in the sample cup at 24 h.

300-500 mL of the main buffer was loaded into the staining device and 2-5 mL of the sample buffer was loaded into the sample cup. The tissue sample was placed in a nylon mesh then placed into the sample cup. Primary antibodies (antibody information and optimized quantity for each target, Supplementary Table 1) and secondary antibodies were added to the sample cup. Dye-conjugated Fc-specific Fab fragments were used for all experiments (2:1 molar ratio to the primary antibody, Jackson immunoresearch). The machine was operated for 24 h at 90 V with maximum current limited to 500 mA. Temperature control was set to maintain 25 °C. Sample cup stir bar rotation was set to 850 rpm and sample cup rotation speed was set to 0.01 rpm.

3.8.12 Dye Conjugation of Secondary Antibodies

For the far-red channel, secondary antibodies conjugated with SeTau647 were used for most labeling experiments as they provide superior photo-stability when compared to commercially available dyes (Podgorski et al. 2012). SeTau-647-NHS was purchased from

SETA BioMedicals and 10 μ l 10 mM aliquots were prepared using DMSO (anhydrous, ZerO2®, 99.9%, Sigma). SeTau-647-NHS were reacted with non-conjugated Fc- specific Fab fragments at 10:1 ratio (Jackson Immunoresearch) for 1 h at RT. Afterwards, the solution was purified using Zeba Spin Desalting Columns (7k MWCO, ThermoFisher Scientific) 2 to 3 times until the desalting column ran clean. The concentration of the resulting solution was measured using DC TM Protein Assay (Bio-Rad) before use.

3.8.13 Refractive Index Matching

Optical clearing of delipidated samples was achieved using Protos-based immersion medium. For samples thicker than 1 mm, optical clearing was done in a step-wise manner. Labeled samples were first incubated in half-step solution (50/50 mix of 2X PBS and Protos-based immersion medium) at 37 °C overnight. Afterwards, the samples were moved to the pure immersion medium and incubated at 37 °C overnight.

3.8.14 Fixation of Labeled Samples

For antibodies that are not stable in Protos-based immersion medium, the eFLASH-labeled samples were fixed with 4% (w/v) PFA to prevent dissociation of bound antibodies. eFLASH-labeled samples in the terminal labeling buffer were washed in 1X PBS with 0.02% (w/v) sodium azide at RT for at least 6 h to wash out Tris in the sample. Samples were then moved to freshly prepared 4% (w/v) PFA solution in 1X PBS, and placed on an orbital shaker at RT overnight. Samples were then washed with 1X PBS with 0.02% (w/v) sodium azide at RT with multiple solution exchanges for at least 6 h.

3.8.15 Light-sheet Imaging and Post-processing

Rapid volumetric imaging was performed with an axially swept light-sheet microscope (SmartSPIM, Lifecanvas Technologies, MA) equipped with three lasers (488 nm, 561 nm, 642 nm). The scanning was fine-tuned for each sample by finely adjusting the position of the illumination objectives to ensure optimal optical sectioning. Focus compensation was programmed as a function of depth for each laser line to account for slight focal variations through imaging depth. All light-sheet imaging was done with either of the following objective lenses: 3.6x objective (custom Lifecanvas design, 0.2 NA 12 mm WD lateral resolution 1.8 μ m in XY), 10x objective (Olympus XLPLN10XSVMP, 0.6 NA, 8 mm WD, lateral resolution 0.66 μ m in XY). Acquired data was post-processed with algorithms described in Swaney et al. (2019). A complete table of imaging modalities and

conditions for every data included in this paper can be found in Supplementary table 2.

3.8.16 Cell Detection

Detection of cells is accomplished by blob detection, followed by dimensionality reduction and classification. Blobs are detected by computing the difference of Gaussians followed by identification of voxels that are the maximum of their neighbors within a chosen radius. 31x31 pixel patches are then extracted in the X/Y, X/Z and Y/Z planes. The rasters of these patches are concatenated and the three resulting 961-element vectors are concatenated to create a 2883-feature vector. All patches of putative cell centers within the volume are collected and PCA is performed to reduce the dimensionality of the vector to 48 components. Each of these components are composed of 2883 elements which are multiplied with the 2883-feature vector per patch to produce 48 numerical features. The vector of each component can be visualized as three 31x31 planes (see Supplementary Figure 3) to allow interpretation of the magnitude of the component. The 48 numerical features are then used to train a random forest classifier using iterative user-supervised training. Finally, the classifier is applied to all patches in the volume to classify each local maximum as a positive cell detection or negative artifact detection.

3.8.17 Atlas Alignment

Atlas alignments of mouse brain hemispheres labeled with eFLASH to the Allen brain reference atlas, CCF V3 (Dong 2008), were carried out using the hybrid automated atlas alignment method described in Swaney et al. (2019), which combines Elastix (Klein et al. 2010) and manual refinement tools to improve alignment accuracy.

3.8.18 Brain Region Segmentation

Detected cell coordinates were transformed from the original coordinate space to the reference coordinate after atlas alignment. The alignment was used to construct a three-dimensional radial basis function using thin-plate splines to map points in the original coordinate space to the reference coordinate space. The point locations in the reference space were then matched against the Allen Brain Mouse Atlas reference (Lein et al. 2007) segmentation to yield counts per brain region. These counts were then used to color the regions in the Allen Brain Mouse Atlas coronal SVG image files. Calculations and visualizations were done using the Nugget python package (Swaney et al. 2019).

3.8.19 Manual Image Analysis

Imaris (Bitplane, Switzerland) was used for soma segmentation, analysis, and neurite tracing in Figure 3.5g-m. Dendrite polarity of NPY+ cells were assessed manually (Puškaš et al. 2005). Fluorescence quantification was done using ImageJ.

3.8.20 Code Availability

The custom code used in this study is available from the corresponding author upon reasonable request.

3.8.21 Data Availability

The data supporting the findings of this study are available from the corresponding author upon reasonable request.

3.9 References

- Ascoli, G.A. et al., 2008. Petilla terminology: Nomenclature of features of GABAergic interneurons of the cerebral cortex. *Nature Reviews Neuroscience*, 9(7), pp.557–568.
- Belle, M. et al., 2017. Tridimensional Visualization and Analysis of Early Human Development. *Cell*, 169(1), pp.161–173.e12.
- Breiman, L., 2001. Random Forest. *Machine Learning*, 45(1), pp.5–32.
- Chen, K.H. et al., 2015. Spatially resolved, highly multiplexed RNA profiling in single cells. *Science*, 348(6233), pp.1360–1363.
- Cho, J.H., Rendall, S.D. & Gray, J.M., 2017. Brain-wide maps of Fos expression during fear learning and recall. *Learning and Memory*, 24(4), pp.169–181.
- Chung, K. & Deisseroth, K., 2013. CLARITY for mapping the nervous system. *Nature methods*, 10(6), pp.508–13. Available at: <http://www.ncbi.nlm.nih.gov/pubmed/23722210>.
- Chung, K. et al., 2011. A microfluidic array for large-scale ordering and orientation of embryos. *Nature Methods*, 8(2), pp.171–176.
- Chung, K. et al., 2013. Structural and molecular interrogation of intact biological systems. *Nature*, 497(7449), pp.332–337. Available at: <http://www.nature.com/doifinder/10.1038/nature12107>.
- Dong, H.W., 2008. *The Allen reference atlas: A digital color brain atlas of the C57Bl/6J male mouse.*, Hoboken, NJ, US: John Wiley & Sons Inc.
- Figueroedo-Cardenas, G. et al., 1996. Colocalization of somatostatin, neuropeptide Y, neuronal nitric oxide synthase and NADPH-diaphorase in striatal interneurons in rats. *Brain Research*, 735(2), pp.317–324.
- Fu, L.Y. & Pol, A.N. van den, 2007. GABA excitation in mouse hilar neuropeptide Y neurons. *Journal of Physiology*, 579(2), pp.445–464.
- Fürth, D. et al., 2018. An interactive framework for whole-brain maps at cellular resolution. *Nature Neuroscience*, 21(1), pp.139–153.
- Gaire, J. et al., 2018. PrismPlus: A mouse line expressing distinct fluorophores in four different brain cell types. *Scientific Reports*, 8(1), pp.1–11.
- Giepmans, B.N.G. et al., 2006. The fluorescent toolbox for assessing protein location and function. *Science*, 312(5771), pp.217–224.

- Gong, S. et al., 2003. A gene expression atlas of the central nervous system based on bacterial artificial chromosomes. *Nature*, 425(6961), pp.917–925.
- Habib, N. et al., 2016. Div-Seq: Single-nucleus RNA-Seq reveals dynamics of rare adult newborn neurons. *Science*, 353(6302), pp.925–928.
- Hawrylycz, M.J. et al., 2012. An anatomically comprehensive atlas of the adult human brain transcriptome. *Nature*, 489(7416), pp.391–399.
- He, M. & Huang, Z.J., 2018. Genetic approaches to access cell types in mammalian nervous systems. *Current Opinion in Neurobiology*, 50, pp.109–118. Available at: <https://doi.org/10.1016/j.conb.2018.02.003>.
- Heffner, C.S. et al., 2012. Supporting conditional mouse mutagenesis with a comprehensive cre characterization resource. *Nature Communications*, 3.
- Hendry, S.H.C., Jones, E.G. & Emson, P.C., 1984. Morphology, distribution, and synaptic relations of somatostatin- and neuropeptide Y-immunoreactive neurons in rat and monkey neocortex. *Journal of Neuroscience*, 4(10), pp.2497–2517.
- Huang, Z.J. et al., 2014. Genetic labeling of neurons in mouse brain. *Cold Spring Harbor Protocols*, 2014(2), pp.150–160.
- Izpisua Belmonte, J.C. et al., 2015. Brains, Genes, and Primates. *Neuron*, 86(3), pp.617–631. Available at: <http://dx.doi.org/10.1016/j.neuron.2015.03.021>.
- Jennings, C.G. et al., 2016. Opportunities and challenges in modeling human brain disorders in transgenic primates. *Nature Neuroscience*, 19(9), pp.1123–1130.
- Kaiser, T. & Feng, G., 2015. Modeling psychiatric disorders for developing effective treatments. *Nature Medicine*, 21(9), pp.979–988. Available at: <http://dx.doi.org/10.1038/nm.3935>.
- Kim, S.-Y. et al., 2015. Stochastic electrotransport selectively enhances the transport of highly electromobile molecules. *Proceedings of the National Academy of Sciences*, 112(46), pp.E6274–E6283. Available at: <http://www.pnas.org/lookup/doi/10.1073/pnas.1510133112>.
- Kim, Y. et al., 2015. Mapping social behavior-induced brain activation at cellular resolution in the mouse. *Cell Reports*, 10(2), pp.292–305. Available at: <http://dx.doi.org/10.1016/j.celrep.2014.12.014>.
- Kim, Y. et al., 2017. Brain-wide Maps Reveal Stereotyped Cell-Type-Based Cortical Architecture and Subcortical Sexual Dimorphism. *Cell*, 171(2), pp.456–469.e22.

- Klein, S. et al., 2010. Elastix: A toolbox for intensity-based medical image registration. *IEEE Transactions on Medical Imaging*, 29(1), pp.196–205.
- Lancaster, M.A. & Knoblich, J.A., 2014. Generation of cerebral organoids from human pluripotent stem cells. *Nature Protocols*, 9(10), pp.2329–2340.
- Lein, E.S. et al., 2007. Genome-wide atlas of gene expression in the adult mouse brain. *Nature*, 445(7124), pp.168–176.
- Li, X. et al., 2017. Generation of a whole-brain atlas for the cholinergic system and mesoscopic projectome analysis of basal forebrain cholinergic neurons. *Proceedings of the National Academy of Sciences of the United States of America*, 115(2), pp.415–420.
- Lin, M.K. et al., 2019. A high-throughput neurohistological pipeline for brain-wide mesoscale connectivity mapping of the common marmoset. *eLife*, 8, pp.1–36.
- Liu, C., 2013. Strategies for Designing Transgenic DNA Constructs., 1027, pp.369–385.
- Liu, C. et al., 2018. A digital 3D atlas of the marmoset brain based on multi-modal MRI. *NeuroImage*, 169(July 2017), pp.106–116. Available at: <https://doi.org/10.1016/j.neuroimage.2017.12.004>.
- Livet, J. et al., 2007. Transgenic strategies for combinatorial expression of fluorescent proteins in the nervous system. *Nature*, 450(November). Available at: <https://search.proquest.com/docview/204558395?accountid=14509>.
- Luo, L., Callaway, E.M. & Svoboda, K., 2018. Genetic Dissection of Neural Circuits: A Decade of Progress. *Neuron*, 98(2), pp.256–281. Available at: <https://doi.org/10.1016/j.neuron.2018.03.040>.
- Madisen, L. et al., 2010. A robust and high-throughput Cre reporting and characterization system for the whole mouse brain. *Nature Neuroscience*, 13(1), pp.133–140.
- Matsuzaki, Y. et al., 2018. Intravenous administration of the adeno-associated virus- PHP.B capsid fails to upregulate transduction efficiency in the marmoset brain. *Neuroscience Letters*, 665(June 2017), pp.182–188. Available at: <https://doi.org/10.1016/j.neulet.2017.11.049>.
- Matthaei, K.I., 2007. Genetically manipulated mice: A powerful tool with unsuspected caveats. *Journal of Physiology*, 582(2), pp.481–488.
- Mellios, N. et al., 2018. MeCP2-regulated miRNAs control early human neurogenesis through differential effects on ERK and AKT signaling. *Molecular Psychiatry*, 23(4), pp.1051–1065.

- Miller, C.T. et al., 2016. Marmosets: A Neuroscientific Model of Human Social Behavior. *Neuron*, 90(2), pp.219–233. Available at: <http://dx.doi.org/10.1016/j.neuron.2016.03.018>.
- Miller, J.A. et al., 2014. Transcriptional landscape of the prenatal human brain. *Nature*, 508(7495), pp.199–206.
- Murakami, T.C. et al., 2018. A three-dimensional single-cell-resolution whole-brain atlas using CUBIC-X expansion microscopy and tissue clearing. *Nature Neuroscience*, 21(4), pp.625–637. Available at: <http://dx.doi.org/10.1038/s41593-018-0109-1>.
- Murray, E. et al., 2015. Simple, Scalable Proteomic Imaging for High-Dimensional Profiling of Intact Systems. *Cell*, 163(6), pp.1500–1514. Available at: <http://dx.doi.org/10.1016/j.cell.2015.11.025>.
- Muzumdar, M. et al., 2006. A Global Double-Fluorescent Cre Reporter Mouse. *Genesis*, 224(September), pp.219–224.
- Oh, S.W. et al., 2014. A mesoscale connectome of the mouse brain. *Nature*, 508(7495), pp.207–214. Available at: <http://dx.doi.org/10.1038/nature13186>.
- Okano, H. & Mitra, P., 2015. Brain-mapping projects using the common marmoset. *Neuroscience Research*, 93, pp.3–7. Available at: <http://dx.doi.org/10.1016/j.neures.2014.08.014>.
- Park, Y.G. et al., 2019. Protection of tissue physicochemical properties using polyfunctional crosslinkers. *Nature Biotechnology*, 37(1), p.73.
- Podgorski, K. et al., 2012. Ultra-Bright and -Stable Red and Near-Infrared Squaraine Fluorophores for In Vivo Two-Photon Imaging. *PLoS ONE*, 7(12).
- Proen  a, L. et al., 1997. Electrocatalytic oxidation of D-sorbitol on platinum in acid medium: Analysis of the reaction products. *Journal of Electroanalytical Chemistry*, 432(1-2), pp.237–242.
- Pu  ka  , N. et al., 2005. Localisation and morphology of cocaine- and amphetamine-regulated transcript (CART) peptide immunoreactive neurons in rat amygdala. *Acta Veterinaria*, 55(5-6), pp.423–434.
- Renier, N. et al., 2016. Mapping of Brain Activity by Automated Volume Analysis of Immediate Early Genes. *Cell*, 165(7), pp.1789–1802. Available at: <http://dx.doi.org/10.1016/j.cell.2016.05.007>.
- Renier, N. et al., 2014. iDISCO: A simple, rapid method to immunolabel large tissue samples for volume imaging. *Cell*, 159(4), pp.896–910. Available at: <http://dx.doi.org/>

10.1016/j.cell.2014.10.010.

Rudy, B. et al., 2011. Three groups of interneurons account for nearly 100% of neocortical GABAergic neurons. *Developmental Neurobiology*, 71(1), pp.45–61.

Sharma, K. et al., 2015. Cell type- and brain region-resolved mouse brain proteome. *Nature Neuroscience*, 18(12), pp.1819–1831.

Swaney, J. et al., 2019. Scalable image processing techniques for quantitative analysis of volumetric biological images from light-sheet microscopy. *bioRxiv*. Available at: <http://dx.doi.org/10.1101/576595>.

Tallini, Y.N. et al., 2006. BAC transgenic mice express enhanced green fluorescent protein in central and peripheral cholinergic neurons. *Physiological Genomics*, 27(3), pp.391–397.

Tehrani-Bagha, A.R. & Holmberg, K., 2013. Solubilization of hydrophobic dyes in surfactant solutions. *Materials*, 6(2), pp.580–608.

Valjent, E. et al., 2009. Looking BAC at striatal signaling: cell-specific analysis in new transgenic mice. *Trends in Neurosciences*, 32(10), pp.538–547.

Vogel, C. & Marcotte, E.M., 2012. Insights into the regulation of protein abundance from proteomic and transcriptomic analyses. *Nature Reviews Genetics*, 13(4), pp.227–232.

Von Engelhardt, J. et al., 2007. Functional characterization of intrinsic cholinergic interneurons in the cortex. *Journal of Neuroscience*, 27(21), pp.5633–5642.

Wang, X. et al., 2018. Three-dimensional intact-tissue sequencing of single-cell transcriptional states. *Science*, 361(6400).

Watanabe, J., Asaka, Y. & Kanamura, S., 1996. Relationship between immunostaining intensity and antigen content in sections. *Journal of Histochemistry and Cytochemistry*, 44(12), pp.1451–1458.

Woodward, A. et al., 2018. Data descriptor: The Brain/MINDS 3D digital marmoset brain atlas. *Scientific Data*, 5, pp.1–12. Available at: <http://dx.doi.org/10.1038/sdata.2018.9>.

Yang, B. et al., 2014. Single-cell phenotyping within transparent intact tissue through whole-body clearing. *Cell*, 158(4), pp.945–958. Available at: <http://dx.doi.org/10.1016/j.cell.2014.07.017>.

Zhang, C. et al., 2017. A platform for stereological quantitative analysis of the brain-wide distribution of type-specific neurons. *Scientific Reports*, 7(1), pp.1–12. Available at: <http://dx.doi.org/10.1038/s41598-017-14699-w>.

Chapter 4

Scalable image processing techniques for quantitative analysis of volumetric biological images from light-sheet microscopy

Justin Swaney*, Lee Kamentsky*, Nicholas Evans, Katherine Xie, Young-Gyun Park,
Gabrielle Drummond, Dae Hee Yun, Kwanghun Chung¹

4.1 Abstract

Here we describe an image processing pipeline for quantitative analysis of terabyte-scale volumetric images of SHIELD-processed mouse brains imaged with light-sheet microscopy. The pipeline utilizes open-source packages for destriping, stitching, and atlas alignment that are optimized for parallel processing. The destriping step removes stripe artifacts, corrects uneven illumination, and offers over 100x speed improvements compared to previously reported algorithms. The stitching module builds upon Terastitcher to create a single volumetric image quickly from individual image stacks with parallel processing enabled by default. The atlas alignment module provides an interactive web-based interface that automatically calculates an initial alignment to a reference image which can be manually refined. The atlas alignment module also provides summary statistics of fluorescence for each brain region as well as region segmentations for visualization. The expected runtime of our pipeline on a whole mouse brain hemisphere is 1-2 d depending on the available computational resources and the dataset size.

¹* indicates co-first authorship.

4.2 Introduction

Light-sheet fluorescence microscopy (LSFM) is an optical sectioning technique that provides high-speed acquisition of high resolution images. Affordable open-access systems have promoted adoption of LSFM (Pitrone et al. 2013). As a result, LSFM has become commonplace in the study of complex biological systems (Tomer et al. 2012; Stefaniuk et al. 2016; Murakami et al. 2018; Power & Huisken 2017). However, the high-throughput acquisition offered by LSFM can quickly generate terabytes of image data, posing challenges in data storage, processing, and visualization. These challenges must be addressed in order to perform the quantitative analyses needed to answer the complex biological question at hand.

SHIELD is a tissue transformation technique that preserves endogenous biomolecules for imaging within intact biological systems (Park et al. 2018). SHIELD retains fluorescent protein signals through the clearing process and is compatible with stochastic electrotransport staining, allowing visualization and quantification of fluorescence signals throughout the entire brain (S.-Y. Kim et al. 2015). When SHIELD-processed tissues are imaged using LSFM, entire organs such as the mouse brain can be imaged at single-cell resolution in just 2 hours, offering more data than was previously available to answer new biological questions.

Here we present detailed protocols for quantifying fluorescence signals in each brain region of SHIELD-processed mouse brain LSFM datasets. The pipeline is composed of modules for image destriping, stitching, and atlas alignment. Each module can either be used independently or in combination to perform region-based statistical analyses of fluorescence within intact mouse brainsamples. The pipeline and all its dependencies have been packaged into a single Docker container, allowing for simple installation and cross-platform use. The ease of deployment offered by Docker makes our image processing pipeline more accessible to researchers without much programming experience. We also provide a dataset of a whole mouse brain hemisphere for users to test our pipeline.

4.2.1 Development of the protocol

In order to analyze large-scale volumetric images acquired using LSFM, research labs typically create their own image processing pipelines (Amat et al. 2015; Stegmaier et al. 2016; Vogelstein et al. 2018). These image processing pipelines are designed to solve specific problems in applying LSFM to the study of complex biological systems. Real-time cell tracking systems have been reported to study the dynamics of embryogenesis in *D. melanogaster*. The cell tracking pipeline relies on optimized CUDA programming to

achieve real-time performance. Several computational pipelines geared toward processing time-lapse images of *D. melanogaster* assume that each time point image is smaller than the amount of available memory. In contrast, LSFM of whole mammalian organs often generates individual volumetric images that are larger than the amount of available memory.

Recently, LSFM images of a whole mouse brain have been used to create a single-cell mouse brain atlas (Murakami et al. 2018). The pipeline consisted of a heterogeneous mix of MATLAB, Python, and C++ software as well as expensive computer hardware, including a dedicated image processing server equipped with four NVIDIA graphics processing units (GPU). In order to handle individual volumetric images that are larger than the amount of available memory, images were processed slice-by-slice for cell detection and rescaled to a manageable size for atlas alignment. Although computationally impressive, such tools often require a great deal of programming expertise or access to proprietary software. As a result, the current large-scale image processing pipelines may be inaccessible to non-experts, and there is a need for large-scale image processing tools for researchers focused on biological questions rather than computational challenges.

The protocols presented here are designed to be easy to setup and applicable to users without much experience in setting up complex development environments. Since some users may only want to use part of our pipeline, the protocols are partitioned into three computational modules: first, our image destriping for removing streaks and performing flat-field correction in raw LSFM images; second, stitching for creating a single 3D image from the individual 2D images; and third, semi-automatic atlas alignment for segmenting brain regions and quantifying fluorescence (Fig. 4.1). Our protocols have been tested on images of SHIELD-processed mouse brain hemispheres acquired with an axially-swept light-sheet microscope.

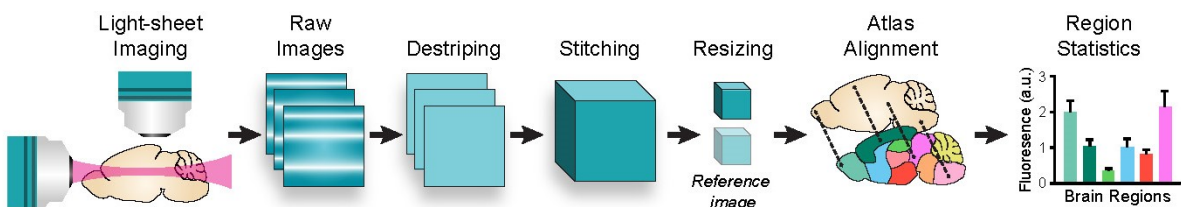


Figure 4.1: Overall image processing pipeline for whole brain analysis. Raw images from LSFM of a SHIELD-processed mouse hemisphere are destriped and corrected for uneven illumination. Destriped images are then stitched into a multichannel volumetric image, which is resampled to match a reference atlas. Point correspondences from an automatic alignment procedure are manually refined to obtain a region segmentation for the full-resolution, stitched image. The region segmentation is then used to quantify mean fluorescence in each brain region.

4.2.1.1 Development of the destriping module

Stripe artifacts are commonplace in images acquired with LSFM due to irregularities in the refractive index (RI) of the sample (Salili et al. 2018). This RI mismatch can be compensated for using an immersion medium that has a similar RI to that of the sample (Murray et al. 2015). However, the material properties of biological tissues, including the RI, are generally not uniform throughout, making some degree of RI mismatch inevitable. RI mismatch usually results in uneven illumination patterns due to optical aberrations that disrupt the incident light.

Current strategies for image destriping are either based on optical filtering or digital filtering (Fehrenbach et al. 2012; Münch et al. 2009; Liang et al. 2016). Optical filtering strategies attempt to compensate for RI mismatch during imaging, effectively removing the stripe artifacts from the source. However, these methods may disrupt the axial resolution of the LSFM system in the process and may not be applicable to large biological samples. In contrast, digital filtering strategies attempt to remove the stripe artifacts after acquisition by exploiting the noise characteristics induced by the optical aberrations. Since digital destriping methods are implemented as image filters, they can be applied more generally to any images with stripe artifacts.

Previous digital destriping methods have included hybrid wavelet-FFT filters, variational removal of stationary noise (VSNR), and multidirectional filters using the contourlet transform (MDSR). Although VSNR and MDSR have shown superior destriping performance, they are prohibitively slow for applying to whole-brain datasets. The hybrid wavelet-FFT filter is the fastest destriping method of these, but its implementation requires a MATLAB license to use and is single-threaded.

In order to provide a fast, open-source destriping solution, we implemented a new digital destriping tool called `pystripe`. `Pystripe` is a Python implementation of the previously reported hybrid wavelet-FFT destriping method with parallel processing support and other improvements. `Pystripe` uses open-source tools instead of proprietary software such as MATLAB. As in the hybrid wavelet-FFT approach, the amount of filtering in `pystripe` can be tuned using a bandwidth parameter. `Pystripe` also adds support for a dual-band filtering mode where the background and foreground of the images can be filtered with separate bandwidths.

4.2.1.2 Development of the stitching module

Imaging large samples with LSFM involves acquiring partially overlapping image stacks which can be stitched together into a single image stack. Several open-source stitching

packages are available (Schindelin et al. 2012; Bria & Iannello 2012). Terastitcher has been widely adopted for stitching large volumetric images acquired with LSFM. However, the Terastitcher merging step executes within a single thread by default, resulting in longer execution times than necessary. It should be noted that the Terastitcher team provides a parallelized version of Terastitcher based on message passing interface (MPI) upon request, but we found implementing our own merging step based on the multipro-
cessing module in Python to be more straightforward than managing MPI.

To address these shortcomings, we created the TSV (Terastitcher Volume) module, which implements the Terastitcher merging step in Python with support for lossless TIFF compression and parallel processing. TSV uses the stack displacements computed from Terastitcher to create a memory-mapped array representing the entire image volume. Multiple workers use this memory-mapped array to convert individual images into a single stack, providing faster overall execution. Each worker merges images together and then saves the result using lossless TIFF compression, resulting in lower overall dataset sizes.

4.2.1.3 Development of the atlas alignment module

In order to segment whole-brain LSFM images into different brain regions, the stitched dataset must be registered to a reference atlas, such as the Allen Mouse Brain Atlas (ABA) (Lein et al. 2007). The ABA consists of an averaged anatomical reference image of autofluorescence and the corresponding region segmentation image. The ABA also contains tools for registering 3D reconstructions from histological sections to the atlas. However, research labs have resorted to custom atlas alignment methods for LFSM images of intact brain samples (Murakami et al. 2018).

Elastix is an open-source medical image registration library that is widely used for non-rigid atlas alignment (Klein et al. 2010). Elastix performs non-rigid atlas alignment by maximizing the mutual information between source and reference images. Elastix was found to have the highest mutual-information benchmark scores in image registration of cleared brain samples among five freely-available software packages (Nazib et al. 2018). The global optimization of mutual information is difficult to scale to whole-brain LSFM datasets since the entire dataset cannot be stored in memory. Following previous work on atlas alignment, we address this issue by rescaling the source image to be a similar size compared to the reference atlas, which is a more manageable size. We use the alignment computed from Elastix to generate a set of approximate point correspondences which can manually refined.

To visualize the atlas alignment and edit the approximate point correspondences, we

created an interactive web-based registration tool called nuggt (NeUroGlancer Ground Truth). Nuggt is built on an open-source visualization package called Neuroglancer. Nuggt does not modify the underlying Neuroglancer code but rather wraps it into a convenient package for interactive LSFM visualization and atlas alignment. Nuggt displays the source and reference images side-by-side along with the point correspondences overlaid on each image. Using nuggt, the point correspondences can be edited and adjusted to improve the atlas alignment. The source image can also be warped while editing the point correspondences, providing rapid visual feedback of the atlas alignment accuracy.

4.2.1.4 Development of the Docker image

One of the main challenges in adopting a new computational pipeline is obtaining the dependencies and recreating the runtime environment that was intended by the developers. In order to simplify the installation of our pipeline, we packaged our pipeline and all of its dependencies into a single Docker container by creating a Dockerfile describing our runtime environment. Docker provides a consistent, light-weight virtual Linux environment on all major operating systems, and our container has been successfully tested on Windows, Mac, and Linux. Docker can be installed from the Docker website, and our container can be downloaded from Docker Hub. By containerizing our pipeline and using web-based visualization, our modules can either be run locally or on dedicated image processing servers which can be accessed from other clients.

4.2.2 Applications of the method

The overall image processing pipeline described in this protocol is designed to calculate fluorescence summary statistics from whole-mouse brain images acquired with LSFM on a per-region basis. Our pipeline has been used to quantify mRuby2 and EGFP fluorescence of virally labeled neurons and presynaptic terminals in SHIELD-processed mouse brain hemispheres 6. Thus, the overall pipeline may be applied in systems neuroscience to quantify fluorescent reporters in cleared samples from mouse models. However, the individual modules that comprise the overall pipeline can also be used independently.

Pystripe can be applied to any images corrupted with horizontal or vertical stripe artifacts. We restricted pystripe to filtering horizontal or vertical stripes because the illumination beam path in most LSFM systems is aligned with the camera detector. Pystripe can, therefore, also be used with multi-view LSFM systems that rotate the sample rather than change the orientation of the illumination beam path (Preibisch et al. 2014). Pystripe also includes the ability to provide a reference flat-field image for illumination correction

of vignetting and other stationary artifacts.

TSV can be used to merge an array of partially overlapping image stacks saved in Terastitcher hierachal format into a single image stack. The memory-mapped array used for stitching is also useful for retrieving sub-volumes of image data. TSV also includes optional utilities for partitioning the stitched image into smaller, uniformly shaped chunks for custom parallel processing. The stitched images can be stored in Neuroglancer precomputed format and served via HTTP, allowing for efficient visualization of whole-brain LSFM datasets at full resolution either locally or over the web.

Nuggt has been used to register SHIELD-processed mouse brain hemisphere datasets to the ABA. Our alignment protocol can be used to register a pair of 3D volumes with mutual information between them and a gradient of mutual information in the initial overlap that can be followed to modify the alignment. In our experience, images that have 90% overlap and rotations of a few degrees can be aligned using this method. The automatic alignment can be refined by adding manually-placed correspondences. The atlas alignment module also provides utilities for calculating image statistics for each brain region given the aligned atlas segmentation.

4.2.3 Comparison with other methods

Many standard solutions exist for similar tasks addressed in our image processing pipeline. In this section, we compare the methods used in our protocol to existing methods in the context of whole brain LSFM image analysis.

4.2.3.1 Destriping

The previously reported digital destriping algorithm MDSR has achieved state of the art destriping performance on LSFM images. MDSR relies on the contourlet transform to perform energy compaction of striping artifacts in arbitrary orientations, whereas pystripe uses the discrete wavelet transform to remove either horizontal or vertical striping artifacts.

When comparing the resulting images from MDSR and pystripe, similar filtering performances are observed from both methods on our test images (Fig. 4.2a). This suggests that the contourlet transform does not drastically improve energy compaction of the stripe artifacts compared to the discrete wavelet transform when the stripes are oriented horizontally. When comparing the average execution speed for destriping using MDSR and pystripe on a single core, MDSR takes over 30 min per frame, while pystripe takes

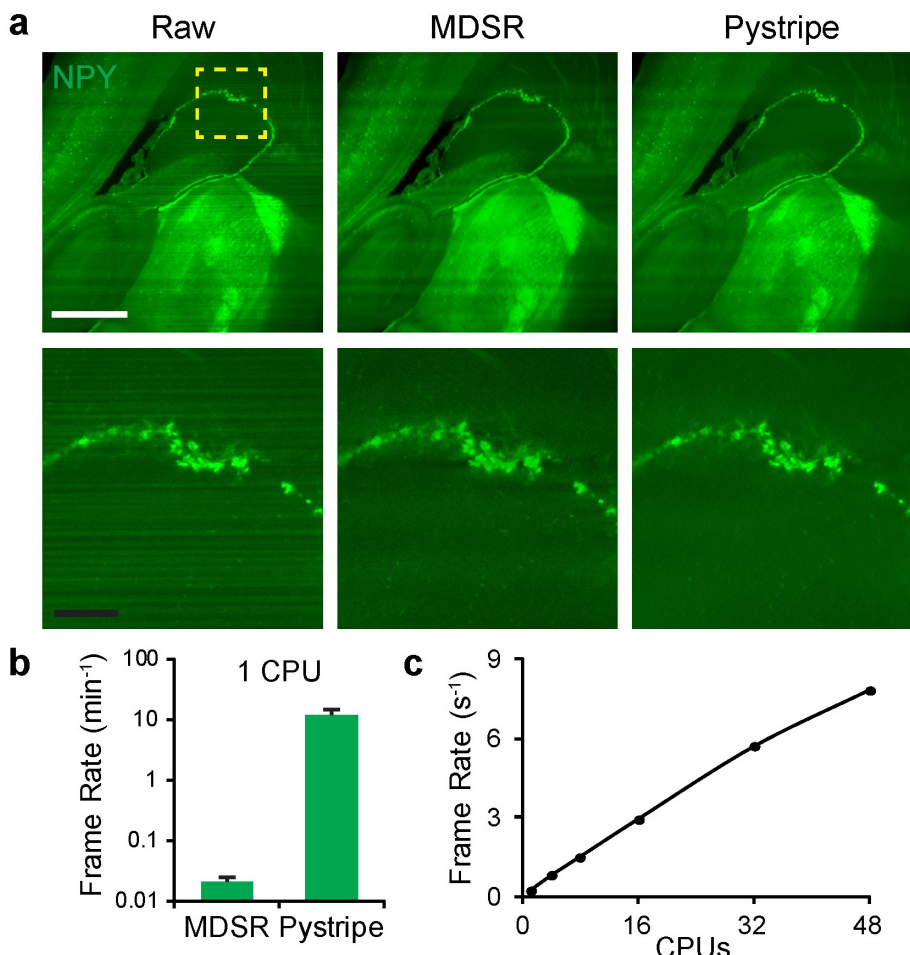


Figure 4.2: Destriping of light-sheet microscopy images using pystripe. (a) Comparison of destriping results from MDSR and pystripe on LSFM images of a SHIELD-processed mouse hemisphere stained for Neuropeptide Y (NPY). Scale bars, 1 mm (white) and 200 m (black). (b) Average single-core destriping speed for MDSR and pystripe on 2048 × 2048 images ($n = 10$, error bars indicate standard deviation). (c) Scaling of destriping speed using pystripe with parallel processing on 2048 × 2048 images.

only 5 seconds (Fig. 4.2b). Using multiple cores, the destriping frame rate for `pystripe` increases linearly with the number of cores, reaching 8 frames per second with 48 cores (Fig. 4.2c, Supplementary Video 1).

`Pystripe` also allows the user to provide an optional reference image for flat-field correction. Ideally, the reference flat would be calculated retroactively from the imaging data, but in practice a single flat for each channel of a particular imaging system still provides significant improvement. The example dataset includes a reference flat for illumination correction during the destriping step. By performing the illumination correction in `pystripe`, reading and writing the whole dataset multiple times can be avoided.

4.2.3.2 Stitching

Building on `Terastitcher`, `TSV` allows fast merging of stacks saved in `Terastitcher` hierachal format. `TSV` obtains similar stitching quality as `Terastitcher` since it uses the same stack displacements and blending functions. Using `TSV`, a whole mouse hemisphere dataset was stitched with and without illumination correction and destriping using `pystripe` (Fig. 4.3a). Moderate vignetting effects were visible in the stitched original images at the intersections between adjacent stacks. These tiling artifacts were effectively reduced using flat-field correction in `pystripe`. Together, `pystripe` and `TSV` generate volumetric images that are ready for quantification by removing shadow and tiling artifacts before stitching (Fig. 4.3b, Supplementary Video 2). When comparing the stitching speed of `TSV` using multiple cores, the stitching frame rate increases linearly, reaching 2.6 frames per second with 48 cores (Fig. 4.3c).

4.2.3.3 Atlas Alignment

Our hybrid automated atlas alignment method with manual refinement differs from wholly automated methods in that the alignment can be improved to the desired degree of accuracy via addition and modification of correspondences between the two volumes to be aligned (Fig. 4.4a). Tools for manual refinement are generally not used in combination with `Elastix` because integrating the transformations across multiple registration tools can be challenging. To the best of our knowledge, there are no web-based tools for interactive atlas alignment currently available.

After aligning a source autofluorescence or nuclear stain image to the reference image, other channels can be aligned to the atlas using the same calculated alignment. For example, neuropeptide Y (NPY) and somatostatin (SST) expression are included with `syto 16` in separate channels of the provided example data (Fig. 4.4b). Using the alignment

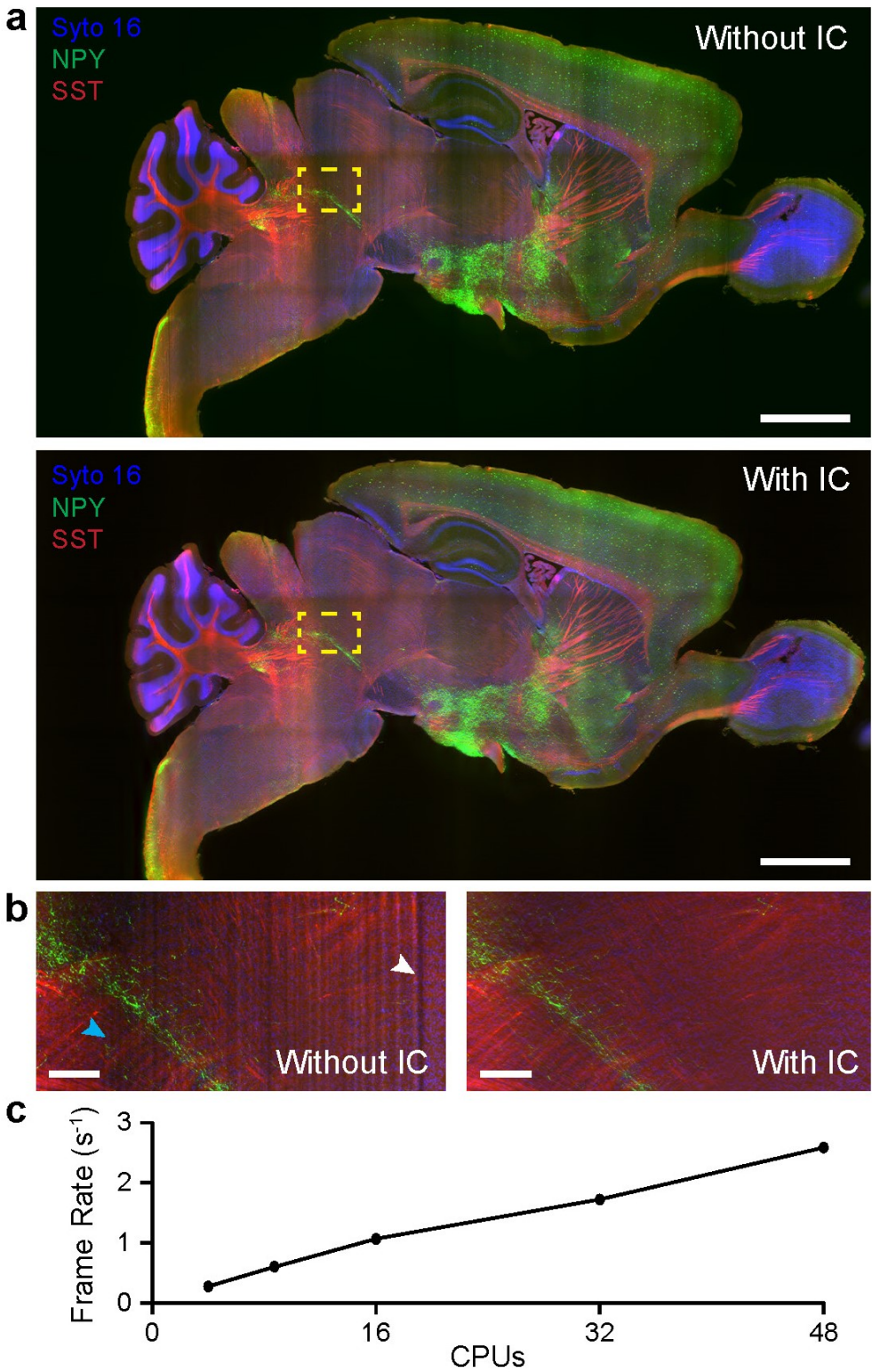


Figure 4.3: Stitching and illumination correction of light-sheet microscopy images using TSV. (a) Comparison of stitching results with and without destriping and illumination correction (IC) performed with pystripe on LSFM images of a SHIELD-processed mouse hemisphere. Scale bar, 2 mm. (b) Comparison of a region of interest with and without IC. Without IC, both uneven illumination (cyan arrow) and stripe artifacts (white arrow) corrupt the images. (c) Scaling of stitching speed using TSV with parallel processing on 2048 x 2048 images.

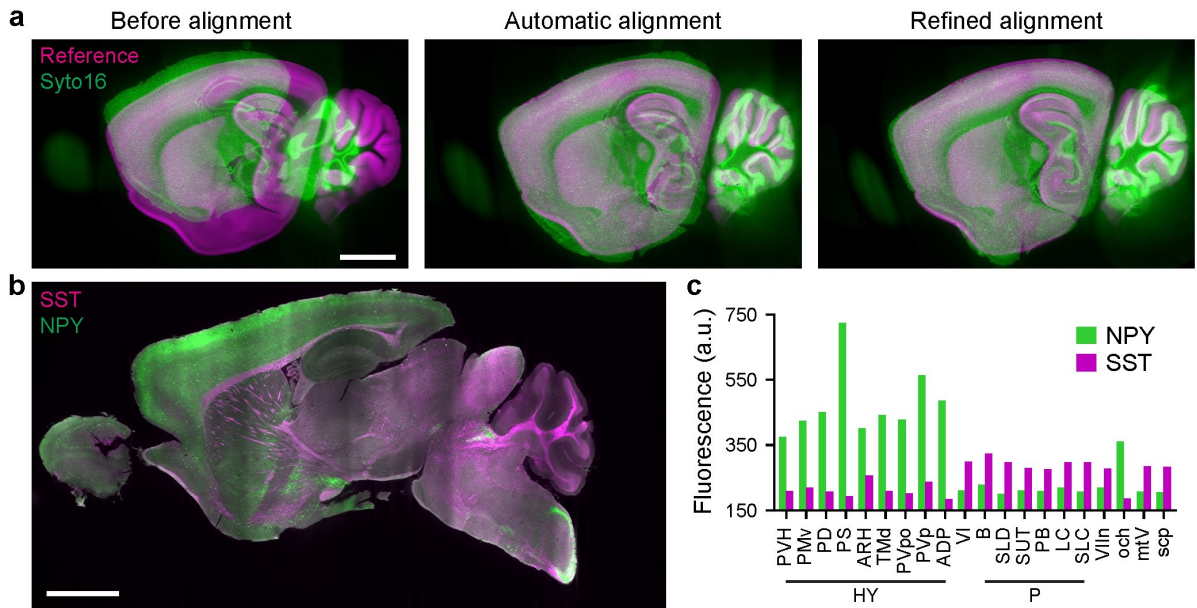


Figure 4.4: Atlas alignment and region-based fluorescence quantification using nuggt. (a) Comparison of atlas alignment of a syto 16 LSFM image to the reference image in the ABA before alignment, after automatic alignment, and after manual refinement. Scale bar, 2 mm. (b) Overlay of NPY and SST in the whole hemisphere example dataset (c) Mean fluorescence for the top 10 regions for both NPY and SST calculated after manual refinement. All other regions from the ABA are omitted for clarity.

calculated by registering the syto 16 channel and the reference from the ABA, the mean fluorescence intensity of NPY and SST in each brain region can be calculated (Fig. 4.4c).

4.2.4 Experimental design

All software modules are available from Github at

<http://www.github.com/chunglabmit/shield-2018>

as well as from Docker hub at

<https://hub.docker.com/r/chunglabmit/shield-2018>

We also provide example LSFM images of a SHIELD-processed mouse hemisphere dataset, which is available from

<http://leviathan-chunglab.mit.edu/nature-protocols-2019>

In order to adapt our image processing pipeline to other experimental situations, users should first complete our protocol using the provided example dataset. This dataset includes raw LSFM images as well as our intermediate results for users to compare and

checkpoint their results throughout the pipeline. We also include a downsampled version of the full example dataset for users that would like to try our protocol on more modest computational hardware.

Young adult (2–4 months; median age 3 months) C57BL/6 mice were housed in a 12 h light/dark cycle with unrestricted access to food and water. To generate the example dataset, a single mouse brain was SHIELD-processed and stained with syto 16 and antibodies targeting NPY and SST using stochastic electrotransport. The mouse brain sample was cut along the mid-sagittal plane and includes the olfactory bulb and the cerebellum. The stained hemisphere was then incubated in a RI-matching solution and imaged using a custom axially-swept LSFM system equipped with a 3.6x/0.2 objective (Special Optics). The resulting voxel width and depth are 1.8 m and 2.0 m, respectively. Although only one animal was involved in preparing the example dataset, our image processing protocol has been tested on over 15 intact mouse brain hemispheres from separate animals. All experimental protocols were approved by the MIT Institutional Animal Care and Use Committee and the Division of Comparative Medicine and were in accordance with guidelines from the National Institute of Health. All experiments using mice were conducted in strict adherence to the ethical regulations of MIT Institutional Animal Care and Use Committee and the Division of Comparative Medicine.

Our protocols have been developed for images of SHIELD-processed mouse brain tissues sectioned along the midsagittal plane with or without the olfactory bulb and cerebellum excised. The images must be acquired in a geometry that allows a transformation of axes (flipping, transposition) and cropping that bring the images into rough alignment with the atlas. In our experience, acquisition of either autofluorescence or a nuclear stain such as syto 16 provides enough mutual information for alignment with the reference volume for the ABA. Images were processed using only the techniques described in the protocol, and figures were prepared using linear lookup tables with adjustment of the minimum and maximum display range.

4.2.5 Expertise needed to implement the protocol

Some minimal computer skills are needed to install Docker and navigate using the command line. If you are unfamiliar with Docker, important introductory information about Docker can be found at <https://docs.docker.com/get-started/>. Our protocol relies on several Docker features for volume sharing and network access, so a basic understanding of Docker is a prerequisite. Since Docker and most of our software is used from the command line, a basic understanding of how to use a terminal on the host operating system is also required.

4.2.6 Limitations

Our overall image processing pipeline currently has been tested for analyzing mouse brain hemisphere datasets using the ABA autofluorescence reference volume. Therefore, we cannot guarantee that our overall pipeline will work in all cases for other species and atlases.

As previously mentioned, `pystripe` cannot remove striping artifacts that are not horizontally or vertically oriented within raw images. When processing images with very bright signals, the hybrid wavelet-FFT filter may introduce some ringing artifacts to the destriped images. The dual-band mode can mitigate these ringing artifacts, but in some cases, these artifacts may be undesirable. The user can elect to reduce the filter bandwidth or skip the destriping step in such cases.

When analyzing mouse brain hemispheres, severe tissue deformation due to improper sample preparation or handling may result in poor atlas alignment since the initial non-rigid alignment may not converge to a global optimum in such cases. Our atlas alignment protocol can be applied to mouse brain hemispheres with the olfactory bulb and cerebellum excised; however, this excision must be mirrored in the anatomical reference volume. This involves cropping the anatomical reference volume to match the source image, which is somewhat ad hoc. We provide referencevolumes from the ABA for use in our Docker container along with reference volumes with the olfactory bulb, cerebellum, or both excised.

Processing whole-brain LSFM datasets is computationally expensive. We provide minimum system requirements that are recommended for processing our example mouse hemisphere dataset. However, we also provide a downsampled version of the original dataset for users without immediate access to computer hardware that meet the minimum system requirements.

4.3 Materials

4.3.1 Equipment

4.3.1.1 Example Data

All Example data is available from our laboratory servers (<http://leviathan-chunglab.mit.edu/nature-protocols-2019>), including:

- Raw data, comprising the raw LSFM images and a flat reference image from the provided mouse brain dataset.
- Destriped data, comprising the destriped LSFM images from the provided dataset.
- Stitched data, comprising the stitched destriped LSFM images from the provided dataset.
- Alignment data, containing the mean fluorescence in each region and intermediate results obtained during atlas alignment.
- Downsampled data, comprising our whole brain raw data downsampled and zipped for testing our pipeline on more modest computer hardware.

4.3.1.2 Computer Equipment

- For benchmarks, the computational pipeline was deployed on a workstation (TWS-1686525, Exxact) running Ubuntu 16.04 LTS on a 1 TB solid-state drive (Samsung) with two 24-core processors (Intel Xeon Platinum 8168), 768 GB of ECC memory, and a single 16 GB NVIDIA GPU (Tesla P100).
- Recommended minimum system requirements for processing the full-resolution example LSFM dataset. A computer with enough hard drive space to store the raw image data as well as the intermediate processing results is required. Our total example data is approximately 3 TB, suggesting that at least 4 TB of extra space is required. We recommend the following minimum system requirements in this case:
 - 8-core processor
 - 64 GB of memory
 - 256 GB solid-state drive with at least 32 GB available
 - 4 TB HDD available for data storage
- Recommended minimum system requirements for the processing the downsampled example LSFM dataset:
 - 2-core processor
 - 16 GB of memory
 - 128 GB solid-state drive with at least 32 GB available
- Software requirements.
 - Docker is recommended to run our software, but expert users can also directly install our software using the pip Python package manager from GitHub. If using our preconfigured Docker image to run our pipeline, Docker must be installed locally. Docker offers a free version of their software called Docker Community Edition.

- We recommend using FIJI for inspecting images throughout our pipeline. FIJI can be obtained from <https://fiji.sc/>

4.3.2 Equipment Setup

4.3.2.1 Docker setup

1. Create a Docker ID to gain access to Docker software and Docker Hub using your preferred email address at <https://hub.docker.com/>. You may need to verify your email address.
2. Download Docker Community Edition for your particular operating system at <https://www.docker.com/products/docker-engine>.
3. Follow the installation instructions and the provided commands to verify that Docker has been installed correctly.
4. With the Docker deamon running, open a terminal and run the following command to install our preconfigured Docker image:

```
docker pull chunglabmit/shield-2018
```

This command will download our software including all of the dependencies as well as commonly used resources needed for atlas alignment with the ABA. Note that we refer to the computer that is running Docker as the “host” and an instance of our Docker image as the “container”.

4.3.2.2 Downloading full resolution example data

This step requires 4 TB of available hard drive space if the whole dataset and intermediate results are downloaded. The raw data is approximately for each channel is approximately 560 GB. Proceed to *downloading downsampled example data* section if your computer does not have this much available space.

1. Create a folder named “data” to contain all of the example data on your machine and note its full path.
2. Start the Docker container with the data folder mounted by entering the following command into the command line:

```
docker run -it -v path_to_data:/data chunglabmit/shield-2018
```

where “path_to_data” should be replaced with the full path to the data folder on the host. The command prompt should indicate that you are now the root user inside a running Docker container (as opposed to your usual username on the host). We refer to the command prompt inside a running container as the “Docker terminal window”.

3. Download the example data needed for a particular stage in the protocol by entering the following command(s) into the Docker terminal window. The data should begin to appear in the data folder that was created. Note that each download may take several hours.
 - Raw data (needed for destriping)

```
wget -P /data -r --no-parent -Nh --cut-dirs 1 -R "index.html*" \
http://leviathan-chunglab.mit.edu/nature-protocols-2019/raw_data/
```

- Destriped data (needed for stitching)

```
wget -P /data -r --no-parent -nH --cut-dirs 1 -R "index.html*" \
http://leviathan-chunglab.mit.edu/nature-protocols-2019/destriped_data/
```

- Stitched data (needed for atlas alignment)

```
wget -P /data -r --no-parent -nH --cut-dirs 1 -R "index.html*" \
http://leviathan-chunglab.mit.edu/nature-protocols-2019/stitched_data/
```

- Alignment data (for comparison of results)

```
wget -P /data -r --no-parent -nH --cut-dirs 1 -R "index.html*" \
http://leviathan-chunglab.mit.edu/nature-protocols-2019/atlas/
```

4.3.2.3 Downloading downsampled example data

1. Navigate to <http://leviathan-chunglab.mit.edu/nature-protocols-2019/> in your browser.
2. Click the `downsampled_data.zip` link and choose to save the file instead of opening it.
3. Unzip the `downsampled_data.zip` file to a new folder called “data” and make note of the full path of this folder on the host.

4.4 Procedure

See Appendix for step-by-step protocol

4.5 Anticipated Results

Upon successful completion of our image processing pipeline, our protocol will yield corrected and stitched multichannel volumetric images of a whole mouse brain hemisphere as well as an alignment with a provided atlas for brain region segmentation. The atlas alignment is used to create spreadsheets in CSV format containing the volume, total fluorescence, and mean fluorescence of each brain region and each channel. These results can be used to create visualizations summarizing the fluorescence in each brain region (Fig. 4c). The reported regions volumes are in voxel units, so the physical volumes will depend on the voxel dimensions used during imaging.

4.6 Acknowledgements

We thank the entire Chung laboratory for support and discussions. K.C. was supported by the Burroughs Wellcome Fund Career Awards at the Scientific Interface, Searle Scholars Program, Packard award in Science and Engineering, NARSAD Young Investigator Award, and the McKnight Foundation Technology Award. This work was supported by the JPB Foundation (PIIF and PNDRF), the NCSOFT Cultural Foundation, the Institute for Basic Science IBS-R026-D1, and the NIH (1-DP2-ES027992, U01MH117072)

4.7 Author Contributions

J.S. worked on `pystripe` and prepared the main figures. L.K. worked on `TSV` and `nuggt`. K.X., Y.G.P. and D.H.Y prepared the example brain sample, and N.E. acquired the example data. G.D., K.X. and N.E. tested the protocol and provided feedback. J.S. and L.K. wrote the paper together, and all authors reviewed the manuscript. K.C. supervised the project.

4.8 Competing Interests

The authors declare no competing interests.

4.9 References

- Amat, F. et al., 2015. Efficient processing and analysis of large-scale light-sheet microscopy data. *Nature Protocols*, 10(11), pp.1679–1696.
- Bria, A. & Iannello, G., 2012. TeraStitcher - A tool for fast automatic 3D-stitching of teravoxel-sized microscopy images. *BMC Bioinformatics*, 13(1).
- Fehrenbach, J. et al., 2012. Variational algorithms to remove stationary noise: Application to SPIM imaging.
- Kim, S.-Y. et al., 2015. Stochastic electrotransport selectively enhances the transport of highly electromobile molecules. *Proceedings of the National Academy of Sciences*, 112(46), pp.E6274–E6283. Available at: <http://www.pnas.org/lookup/doi/10.1073/pnas.1510133112>.
- Klein, S. et al., 2010. Elastix: A toolbox for intensity-based medical image registration. *IEEE Transactions on Medical Imaging*, 29(1), pp.196–205.
- Lein, E.S. et al., 2007. Genome-wide atlas of gene expression in the adult mouse brain. *Nature*, 445(7124), pp.168–176.
- Liang, X. et al., 2016. Stripe artifact elimination based on nonsubsampled contourlet transform for light sheet fluorescence microscopy. *Journal of Biomedical Optics*, 21(10), p.106005. Available at: <http://biomedicaloptics.spiedigitallibrary.org/article.aspx?doi=10.1117/1.JBO.21.10.106005>.
- Murakami, T.C. et al., 2018. A three-dimensional single-cell-resolution whole-brain atlas using CUBIC-X expansion microscopy and tissue clearing. *Nature Neuroscience*, 21(4), pp.625–637. Available at: <http://dx.doi.org/10.1038/s41593-018-0109-1>.
- Murray, E. et al., 2015. Simple, Scalable Proteomic Imaging for High-Dimensional Profiling of Intact Systems. *Cell*, 163(6), pp.1500–1514. Available at: <http://dx.doi.org/10.1016/j.cell.2015.11.025>.
- Münch, B. et al., 2009. Stripe and ring artifact removal with combined wavelet-Fourier filtering. *EMPA Activities*, 17(2009-2010 EMPA ACTIVITIES), pp.34–35.
- Nazib, A. et al., 2018. Performance of Image Registration Tools on High-Resolution 3D Brain Images. Available at: <https://arxiv.org/abs/1807.04917>.
- Park, Y.-g. et al., 2018. Protection of tissue physicochemical properties using polyfunctional., (December).
- Pitrone, P.G. et al., 2013. OpenSPIM: an open-access light-sheet microscopy platform.

Nature Methods, 10(7), pp.598–599. Available at: <http://www.nature.com/doifinder/10.1038/nmeth.2507>.

Power, R.M. & Huisken, J., 2017. A guide to light-sheet fluorescence microscopy for multiscale imaging. *Nature Methods*, 14(4), pp.360–373. Available at: <http://arxiv.org/abs/nmeth.4224>.

Preibisch, S. et al., 2014. Efficient bayesian-based multiview deconvolution. *Nature Methods*, 11(6), pp.645–648. Available at: <http://arxiv.org/abs/1308.0730>.

Salili, S.M., Harrington, M. & Durian, D.J., 2018. Note: Eliminating stripe artifacts in light-sheet fluorescence imaging. *Review of Scientific Instruments*, 89(3), pp.43–45.

Schindelin, J. et al., 2012. Fiji: An open-source platform for biological-image analysis. *Nature Methods*, 9(7), pp.676–682.

Stefaniuk, M. et al., 2016. Light-sheet microscopy imaging of a whole cleared rat brain with Thy1-GFP transgene. *Scientific Reports*, 6, pp.1–9.

Stegmaier, J. et al., 2016. Real-Time Three-Dimensional Cell Segmentation in Large-Scale Microscopy Data of Developing Embryos. *Developmental Cell*, 36(2), pp.225–240. Available at: <http://dx.doi.org/10.1016/j.devcel.2015.12.028>.

Tomer, R. et al., 2012. Quantitative high-speed imaging of entire developing embryos with simultaneous multiview light-sheet microscopy. *Nature Methods*, 9(7), pp.755–763. Available at: <http://dx.doi.org/10.1038/nmeth.2062>.

Vogelstein, J.T. et al., 2018. A community-developed open-source computational ecosystem for big neuro data. *Nature methods*, 15(November), pp.846–847.

Chapter 5

3D Imaging and High-Content Morphological Analysis of Intact Human Cerebral Organoids

Alexandre Albanese*, **Justin Swaney***, Dae Hee Yun, Nick Evans, Jenna Antonucci-Johnson, Vincent Pham, Chloe Delepine, Mriganka Sur, Lee Gehrke, Kwanghun Chung¹

5.1 Introduction

This is the introduction. Phasellus non purus id mauris aliquam rutrum vitae quis tellus. Maecenas rhoncus ligula nulla, fringilla placerat mi consectetur eu. Aenean nec metus ac est ornare posuere. Nunc ipsum lacus, gravida commodo turpis quis, rutrum eleifend erat. Pellentesque id lorem eget ante porta tincidunt nec nec tellus.

5.2 Method

Vivamus consectetur, velit in congue lobortis, massa massa lacinia urna, sollicitudin semper ipsum augue quis tortor. Donec quis nisl at arcu volutpat ultrices. Maecenas ex nibh, consequat ac blandit sit amet, molestie in odio. Morbi finibus libero et nisl dignissim, at ultricies ligula pulvinar.

^{1*} indicates co-first authorship.

5.2.1 Subsection 1

This is the first part of the methodology. Integer leo erat, commodo in lacus vel, egestas varius elit. Nulla eget magna quam. Nullam sollicitudin dolor ut ipsum varius tincidunt. Duis dignissim massa in ipsum accumsan imperdiet. Maecenas suscipit sapien sed dui pharetra blandit. Morbi fermentum est vel quam pretium maximus.

5.2.2 Subsection 2

This is the second part of the methodology. Nullam accumsan condimentum eros eu volutpat. Maecenas quis ligula tempor, interdum ante sit amet, aliquet sem. Fusce tellus massa, blandit id tempus at, cursus in tortor. Nunc nec volutpat ante. Phasellus dignissim ut lectus quis porta. Lorem ipsum dolor sit amet, consectetur adipiscing elit.

5.3 Results

Table 5.1 shows us how to add a table. Integer tincidunt sed nisl eget pellentesque. Mauris eleifend, nisl non lobortis fringilla, sapien eros aliquet orci, vitae pretium massa neque eu turpis. Pellentesque tincidunt aliquet volutpat. Ut ornare dui id ex sodales laoreet.

Table 5.1: This is the table caption. Suspendisse blandit dolor sed tellus venenatis, venenatis fringilla turpis pretium.

| Column 1 | Column 2 | Column 3 |
|----------|----------|----------|
| Row 1 | 0.1 | 0.2 |
| Row 2 | 0.3 | 0.3 |
| Row 3 | 0.4 | 0.4 |
| Row 4 | 0.5 | 0.6 |

5.4 Discussion

This is the discussion. Etiam sit amet mi eros. Donec vel nisi sed purus gravida fermentum at quis odio. Vestibulum quis nisl sit amet justo maximus molestie. Maecenas vitae arcu erat. Nulla facilisi. Nam pretium mauris eu enim porttitor, a mattis velit dictum. Nulla sit amet ligula non mauris volutpat fermentum quis vitae sapien.

5.5 Conclusion

This is the conclusion to the chapter. Nullam porta tortor id vehicula interdum. Quisque pharetra, neque ut accumsan suscipit, orci orci commodo tortor, ac finibus est turpis eget justo. Cras sodales nibh nec mauris laoreet iaculis. Morbi volutpat orci felis, id condimentum nulla suscipit eu. Fusce in turpis quis ligula tempus scelerisque eget quis odio. Vestibulum et dolor id erat lobortis ullamcorper quis at sem.

Chapter 6

Vascularization of cerebral organoids using two-photon stereolithography

Justin Swaney*, Srinu Pujari*, Alexandre Albanese*, Nicholas Evans, Dae Hee Yun,
Kwanghun Chung¹

6.1 Introduction

This is the introduction. Nunc lorem odio, laoreet eu turpis at, condimentum sagittis diam. Phasellus metus ligula, auctor ac nunc vel, molestie mattis libero. Praesent id posuere ex, vel efficitur nibh. Quisque vestibulum accumsan lacus vitae mattis.

6.2 Method

In tincidunt viverra dolor, ac pharetra tellus faucibus eget. Pellentesque tempor a enim nec venenatis. Morbi blandit magna imperdiet posuere auctor. Maecenas in maximus est.

6.2.1 Subsection 1

This is the first part of the methodology. Praesent mollis sem diam, sit amet tristique lacus vulputate quis. Vivamus rhoncus est rhoncus tellus lacinia, a interdum sem egestas. Curabitur quis urna vel quam blandit semper vitae a leo. Nam vel lectus lectus.

¹* indicates co-first authorship.

6.2.2 Subsection 2

This is the second part of the methodology. Aenean vel pretium tortor. Aliquam erat volutpat. Quisque quis lobortis mi. Nulla turpis leo, ultrices nec nulla non, ullamcorper laoreet risus.

6.3 Results

These are the results. Curabitur vulputate nisl non ante tincidunt tempor. Aenean porta nisi quam, sed ornare urna congue sed. Curabitur in sapien justo. Quisque pulvinar ullamcorper metus, eu varius mauris pellentesque et. In hac habitasse platea dictumst. Pellentesque nec porttitor libero. Duis et magna a massa lacinia cursus.

6.4 Discussion

This is the discussion. Curabitur gravida nisl id gravida congue. Duis est nisi, sagittis eget accumsan ullamcorper, semper quis turpis. Mauris ultricies diam metus, sollicitudin ultricies turpis lobortis vitae. Ut egestas vehicula enim, porta molestie neque consectetur placerat. Integer iaculis sapien dolor, non porta nibh condimentum ut.

6.5 Conclusion

This is the conclusion to the chapter. Nulla sed condimentum lectus. Duis sed tempor erat, at cursus lacus. Nam vitae tempus arcu, id vestibulum sapien. Cum sociis natoque penatibus et magnis dis parturient montes, nascetur ridiculus mus.

Conclusion

6.6 Thesis summary

This work has addressed several major challenges associated with scaling up experimental techniques used in neuroscience research. These advances enable neuroscientists to answer long-standing biological questions in new ways by lowering the barrier for staining and imaging, providing scalable image processing tools for analysis, and engineering new culture systems for the study of large-scale brain models.

6.7 Future work

There are several potential directions for extending this thesis. Lorem ipsum dolor sit amet, consectetur adipiscing elit. Aliquam gravida ipsum at tempor tincidunt. Aliquam ligula nisl, blandit et dui eu, eleifend tempus nibh. Nullam eleifend sapien eget ante hendrerit commodo. Pellentesque pharetra erat sit amet dapibus scelerisque.

Vestibulum suscipit tellus risus, faucibus vulputate orci lobortis eget. Nunc varius sem nisi. Nunc tempor magna sapien, euismod blandit elit pharetra sed. In dapibus magna convallis lectus sodales, a consequat sem euismod. Curabitur in interdum purus. Integer ultrices laoreet aliquet. Nulla vel dapibus urna. Nunc efficitur erat ac nisi auctor sodales.

Appendix 1: Curriculum Vitae

Justin M. Swaney

jswaney@mit.edu
jmswaney.com

[linkedin.com/in/jmswaney](https://www.linkedin.com/in/jmswaney)

EDUCATION

| | |
|--|-----------------------------------|
| Massachusetts Institute of Technology , Cambridge, MA <i>PhD in Chemical Engineering, Minor in Computer Science</i> <i>Thesis title: Vascularization of Neural Organoids Using Two-Photon Stereolithography</i> | December 2019 (<i>expected</i>) |
| University of Wisconsin-Madison , Madison, WI <i>Bachelor of Science in Chemical Engineering, Certificate in Mathematics</i> | May 2014 GPA: 3.99/4.0 |

RESEARCH EXPERIENCE

| | |
|--|--------------------------|
| Samply LLC , Walworth, WI <i>Founder and CEO</i> | May 2019 – Present |
| Kwanghun Chung Lab, MIT , Cambridge, MA <i>Graduate Researcher</i> | September 2014 – Present |
| <ul style="list-style-type: none">Led development of a visual sample library explorer for music producers based on a novel deep audio embedding network trained by semi-supervised sample classification in Tensorflow.Performed demonstrations and poster presentations of Samply at the MIT Computing Exposition. | |

| | |
|---|----------------------|
| Regina Murphy Lab, UW-Madison , Madison, WI <i>Undergraduate Researcher</i> | June 2013 – May 2014 |
| <ul style="list-style-type: none">Applied Gustafson-Kessel Fuzzy clustering to the tracking analysis of amyloid beta nanoparticles to quantify aggregation dynamics in Alzheimer's disease. | |

TEACHING EXPERIENCE

| | |
|---|----------------------|
| Academy for Advanced Research and Development , Cambridge, MA <i>Assistant Professor (Part-time)</i> | March 2017 – Present |
| <ul style="list-style-type: none">Supervised STEM-oriented high-school and undergraduate students in individual research projects in data science and machine learning.Directed summer courses on self-driving cars using Raspberry Pi's and on applications of data science in healthcare including tumor segmentation in MRI images using Python.Provided editorial assistance for student publications and recommendations for college applications. | |

| | |
|---|---------------------------|
| UW-Madison Chemical Engineering Department , Madison, WI <i>Teaching Assistant (Part-time)</i> | December 2013 – June 2014 |
| <ul style="list-style-type: none">Taught MATLAB by live coding solutions to example problems in the context of chemical engineering.Demonstrated and explained the algorithms behind algebraic and differential equation solvers as well as non-linear optimization tools in MATLAB. | |

SKILLS and TECHNIQUES

| | | | |
|-----------------|----------------------|------------------|-------------------------|
| Python | Git | Docker | Flask / Django |
| MATLAB | Linux / Unix | TDD / Travis CI | iPSC & organoid culture |
| LabVIEW / DAQmx | Tensorflow / Pytorch | SLURM | Immunohistochemistry |
| Javascript | Closure(script) | Accumulo / MySQL | Light-sheet microscopy |
| C / C++ | AWS / Google Cloud | Spark | CLARITY |

PUBLICATIONS

- Swaney, J.***, Pujari, S.* , Albanese, A.* , Yun, D.H., Evans, N.B., Chung, K. "Vascularization of neural organoids using two-photon stereolithography", (*in preparation*).
- Albanese, A.* , **Swaney, J.***, Yun, D.H., Evans, N.B., Antonucci-Johnson, J., Gehrke, L., Chung, K. "3D Imaging and High Content Morphological Analysis of Intact Human Cerebral Organoids", (*in preparation*).
- Yun, D.H.* , Park, Y.G.* , Cho, J.H.* , Kamentsky, L., Evans, N.B., Albanese, A., Xie, K., **Swaney, J.**, Sohn, C.H., Tian, Y., Zhang, Q., Drummond, G., Guan, W., DiNapoli, N., Choi, H., Jung, H.Y., Ruelas, L., Feng, G., Chung, K. "Ultrafast immunostaining of organ-scale tissues for scalable proteomic phenotyping", *bioRxiv* (submitted to *Nature Biotechnology*), 2019, doi:10.1101/660373.
- Swaney, J.***, Kamentsky, L.* , Evans, N.B., Xie, K., Park, Y.G., Drummond, G., Yun, D.H., Chung, K. (2019) "Scalable image processing techniques for quantitative analysis of volumetric biological images from light-sheet microscopy", *bioRxiv*, doi:10.1101/576595.
- Ku, T.* , **Swaney, J.***, Park, J.Y.* , Albanese, A., Murray, E., Cho, J.H., Park, Y.G., Mangena, V., Chen, J., Chung, K. (2016) "Multiplexed and scalable super-resolution imaging of three-dimensional protein localization in size-adjustable tissues", *Nature Biotechnology*, doi:10.1038/nbt.3641.
- Murray, E.* , Cho, J.H.* , Goodwin, D.* , Ku, T.* , **Swaney, J.***, Kim, S.Y., Choi, H., Park, Y.G., Park, J.Y., Hubbert, A., McCue, M., Vassallo, S., Bakh, N., Frosch, M.P., Wedeeng, V.J., Seung, H.S., Chung, K. (2015) "Simple, scalable proteomic imaging for high-dimensional profiling of intact systems", *Cell*, 163, 6, 1500–1514. doi:10.1016/j.cell.2015.11.025
- (* indicates co-first author)

POSTERS and PRESENTATIONS

- Poster** "Non-Parametric Hyperdimensional Analysis of Multiscale Phenotypic Factors in Intact Human Cerebral Organoids", Society for Neuroscience, October, 2019, Chicago, IL.
- Poster** "Non-Parametric Hyperdimensional Analysis of Multiscale Phenotypic Factors in Intact Human Cerebral Organoids", Cell Symposia: Engineering Organoids and Organoids, August, 2019, San Diego, CA.
- Presenter** "Simple, scalable proteomic imaging for high-dimensional profiling of intact systems", Korea Advanced Institute of Science and Technology, January, 2018, Daejeon, South Korea.
- Presenter** "Vascularization of neural organoids using two-photon stereolithography", Massachusetts Institute of Technology, October, 2016, Cambridge, MA.
- Poster** "Simple, scalable proteomic imaging for high-dimensional profiling of intact systems", Society for Neuroscience, November, 2016, San Diego, CA.
- Poster** "Kinetic modeling of amyloid beta aggregation using nanoparticle tracking analysis", Undergraduate Research Symposium, December, 2013, Madison, WI.

HONORS and AWARDS

- 1st Place – Machine Learning Across Disciplines Challenge, MIT College of Computing. 2019
- Outstanding Seminar Award, MIT Chemical Engineering Department. 2018
- Individual Accomplishment Award, MIT Chemical Engineering Department. 2018
- Barbara J. Weedon Fellowship, MIT Picower Institute 2016-2017
- Lemelson Engineering Presidential Fellowship, MIT 2015
- Chancellor's Scholarship, UW-Madison 2010-2014 (Class Co-chair: 2010)
- Dean's Honor List, UW-Madison 2010-2014

Appendix 2: Image processing protocol

Part A: Destriping LSFM images using `pystripe`

TIMING: 30 min setup (excluding download time), 1-4 h unattended computer time (depending on data size)

Container setup

- i) Download the raw data (see ‘Downloading full resolution example data’ in the MATERIALS section) or move pre-existing raw data to a new folder called “data” and make note of the folder path on the host. Skip this step if using the downsampled example data.

CRITICAL STEP Pystripe only accepts TIFF and RAW file formats. If using the full-resolution example data, the data folder should be created on a device with at least 4 TB of available space.

? TROUBLESHOOTING

- ii) Inspect the raw images using FIJI. ? TROUBLESHOOTING
- iii) Open a terminal and start the Docker container with the data folder from the host mounted inside the container using the following command:

```
docker run -it -v path_to_data:/data chunglabmit/shield-2018
```

where “path_to_data” should be replaced with the full path of the data folder on the host. Note that the command prompt will change to the root user indicating that the prompt is now running interactively from within the container.

CRITICAL STEP The semantics for mounting a volume to share data with the container are to specify a source path on the host and a target path inside the container. The syntax for expressing this at the command line is “-v path_on_host:path_in_container”. Note that path_in_container is a Unix-style path since the container is a Linux virtual machine.

CRITICAL STEP Add quotes around the full path if it contains any spaces. ? TROUBLESHOOTING

- iv) Verify that the data folder is mounted correctly by running the following command from within the Docker terminal window.

```
ls /data
```

This command should list the contents of the shared data folder mounted in the container at the root path.

Destriping raw images from whole-brain LSF

- v) Run the following command to get the latest version of pystripe:

```
git -C /shield-2018/pystripe pull
```

Inspect the help message from pystripe by entering the following command from within the container.

```
pystripe --help
```

Instructions for using pystripe from the command line should print. Note from the instructions that an input folder and filter bandwidth are required and that pystripe will default to using all CPU cores available to the container.

- vi) Destripe the raw data one channel at a time by entering the following commands within the Docker terminal window for each channel:

```
pystripe -i /data/raw_data/channel -o /data/destriped_data/channel -s1 sigma1 -s2  
sigma2 -w wavelet -c compression -x crossover -f flat.tif -d dark
```

where “channel” represents the name of the folder containing images of the current channel, “sigma1” and “sigma2” represent the dual-band filter bandwidths in pixels (higher gives more filtering), “wavelet” is the mother wavelet name, “compression” is the amount of lossless TIFF compression, and “crossover” is the intensity range used to switch between filter bands. The arguments “flat” and “dark” are optional inputs for applying illumination correction. Including illumination correction in pystripe removes the need to load the images into memory multiple times.

If using the full-resolution example data, then enter the following command.

```
pystripe -i /data/raw_data/Ex_0_Em_0 -o /data/destriped_data/Ex_0_Em_0 -s1 256 -s2  
256 -w db10 -c 3 -x 10 --flat flat.tif --dark 100
```

If using the downsampled example data, then enter the following command.

```
pystripe -i /data/raw_data/Ex_0_Em_0 -o /data/destriped_data/Ex_0_Em_0 -s1 32 -s2  
32 -w db10 -c 3 -x 10 --flat flat_downsampled.tif --dark 100
```

A progress bar showing the destriping progress for that channel will appear, and the destriped images will appear in the data folder, which is also available from the host machine.

Inspect some of the resulting destriped images and the corresponding raw images in FIJI. Note that pystripe maintains the raw data folder structure in its output.

- vii) Repeat steps A) vi-vii for all other channels.
- viii) Shutdown the Docker container by typing “exit” in the Docker terminal window. The terminal will return to its original state before entering the Docker container.

CRITICAL STEP Since Docker creates new containers each time they are started, no files inside the Docker container will be saved when restarting the container except for files in shared folders on the host, such as the mounted data folder.

PAUSE POINT The destriped data folder can be archived for processing at a later date.

Part B: Stitching LSFM stacks using TSV

TIMING: 45 min setup (excluding download time), 4-12 h unattended computer time (depending on data size)

Container setup

- i) Download the destriped data (see ‘Downloading full resolution example data’ in the MATERIALS section) or use the destriped data from the previous step. If using the downsampled data, complete part A and use the resulting destriped data for part B.

CRITICAL STEP TSV only accepts TIFF and RAW file formats saved in Terastitcher hierarchical format. If using the full resolution example data, the data folder should be on a device with at least 4 TB of available space.

- ii) Open a terminal and start the Docker container with the data folder from the host mounted inside the container using the following command:

```
docker run -it -v path_to_data:/data chunglabmit/shield-2018
```

where “path_to_data” should be replaced with the full path of the data folder on the host. Note that the command prompt will change to the root user indicating that the prompt is now running interactively from within the container.

CRITICAL STEP The semantics for mounting a volume to share data with the container are to specify a source path on the host and a target path inside the container. The syntax for expressing this at the command line is “-v path_on_host:path_in_container”. Note that path_in_container is a Unix-style path since the container is a Linux virtual machine.

CRITICAL STEP Add quotes around the full path if it contains any spaces. Stitching images from whole-brain LSFM

- iii) Run the following command to get the latest version of TSV:

```
git -C /shield-2018/tsv pull
```

- iv) Use Terastitcher to create a stitching project file based on a single channel by entering the following command in the Docker terminal window.

```
terastitcher -1 --volin=/data/destriped_data/channel_master --ref1=H --ref2=V \
--ref3=D --vx11=x --vx12=y --vx13=z --sparse_data \
--projout=/data/destriped_data/channel_master/xml_import.xml
```

where “channel_master” represents the name of the folder containing images of the channel used for calculating stack displacements and x, y, and z are the physical voxel dimensions in micron. If using the full-resolution example data, then enter the following command:

```
terastitcher -1 --volin=/data/destriped_data/Ex_1_Em_1 --ref1=H --ref2=V \
--ref3=D --vx11=1.8 --vx12=1.8 --vx13=2 --sparse_data \
--projout=/data/destriped_data/Ex_1_Em_1/xml_import.xml
```

If using the downsampled example data, then enter the following command:

```
terastitcher -1 --volin=/data/destriped_data/Ex_1_Em_1 --ref1=H --ref2=V \
--ref3=D --vx11=14.4 --vx12=14.4 --vx13=16 --sparse_data \
--projout=/data/destriped_data/Ex_1_Em_1/xml_import.xml \
```

CRITICAL STEP The voxel dimensions must match the voxel dimensions for the LSFM system in microns.

? TROUBLESHOOTING

- v) Calculate the stack displacements using Terastitcher by entering the following command in the Docker terminal window:

```
terastitcher -2 --projin=/data/desriped_data/channel_master/xml_import.xml \
--projout=/data/desriped_data/channel_master/xml_displacement.xml
```

If using the example data, enter the following command:

```
terastitcher -2 --projin=/data/desriped_data/Ex_1_Em_1/xml_import.xml \
--projout=/data/desriped_data/Ex_1_Em_1/xml_displacement.xml
```

? TROUBLESHOOTING

- vi) Generate a Terastitcher project file by entering the following command in the Docker terminal window:

```
terastitcher -3 --projin=/data/desriped_data/channel_master/xml_displacement.xml \
--projout=/data/desriped_data/channel_master/xml_displproj.xml
```

If using the example data, enter the following command:

```
terastitcher -3 --projin=/data/desriped_data/Ex_1_Em_1/xml_displacement.xml \
--projout=/data/desriped_data/Ex_1_Em_1/xml_displproj.xml
```

- vii) Use TSV to generate stitched images by entering the following command in the Docker terminal window:

```
tsv-convert-2D-tif --xml-path /data/desriped_data/channel_master/xml_displproj.xml \
--output-pattern /data/stitched_data/channel_master/"{z:04d}.tiff" \
--compression compression --ignore-z-offsets
```

where “/data/stitched_data/channel_master” is a new folder that will be created for the stitched images from the master channel, and “compression” is the amount of lossless TIFF compression to use. If using the example data, enter the following command:

```
tsv-convert-2D-tif --xml-path /data/destriped_data/Ex_1_Em_1/xml_displproj.xml \
--output-pattern /data/stitched_data/Ex_1_Em_1_master/"{z:04d}.tiff" \
--compression 4 --ignore-z-offsets
```

A progress bar will appear showing the stitching progress. Note that TSV will default to using all processor cores available to the container.

- viii) Inspect the stitched images in FIJI. TSV generates TIFF images which can be imported directly into FIJI.
- ix) If there are no more channels to stitched, then proceed to part C of the protocol.
If there are more channels to be stitched, then the following command will stitch other channels using the displacements calculated from the master channel:

```
tsv-convert-2D-tif --xml-path /data/destriped_data/channel_master/xml_displproj.xml \
--output-pattern /data/stitched_data/channel/"{z:04d}.tiff" --compression compression \
--ignore-z-offsets --input /data/destriped_data/channel
```

Where “channel_master” represents the folder name of the channel used for calculating stack displacements, “channel” represents folder of images from another channel to be stitched using the previously computed displacements, and the other arguments are as described before. Repeat this command for all other channels to be stitched.

If using the example data, then enter the following commands:

```
tsv-convert-2D-tif --xml-path /data/destriped_data/Ex_1_Em_1/xml_displproj.xml \
--output-pattern /data/stitched_data/Ex_0_Em_0/"{z:04d}.tiff" --compression 4 \
--ignore-zoffsets --input /data/destriped_data/Ex_0_Em_0

tsv-convert-2D-tif --xml-path /data/destriped_data/Ex_1_Em_1/xml_displproj.xml \
--output-pattern /data/stitched_data/Ex_2_Em_2/"{z:04d}.tiff" --compression 4 \
--ignore-zoffsets --input /data/destriped_data/Ex_2_Em_2
```

- x) Close the Docker container by typing “exit” into the Docker terminal window and pressing “Enter”.

PAUSE POINT The stitched data folder can be archived for processing at a later date.

Part C: Atlas alignment with manual refinement using nuggt

TIMING: 1-2 hr setup (excluding download time), 6-12 h unattended computer time (depending on data set size)

Container setup and Neuroglancer basics

- i) Download the stitched data (see ‘Downloading full resolution example data’ in the MATERIALS section) or use the stitched data from the previous step. If using the downsampled data, complete part B and use the resulting stitched data for part C.
- ii) For Linux users, open a terminal and start the Docker container with the data folder from the host mounted inside the container using the following command:

```
docker run -it --expose 8999 -p 8999:8999/tcp --network host \
-v path_to_data:/data --shm-size 1g chunglabmit/shield-2018
```

For Windows and Mac users, enter the following command:

```
docker run -it --expose 8999 -p 8999:8999/tcp -v path_to_data:/data \
--shm-size 1g chunglabmit/shield-2018
```

CRITICAL STEP Add quotes around the full path if it contains any spaces.

- iii) The following files are included in the “/allen-mouse-brain-atlas” folder inside the Docker container:
 - autofluorescence_25_half_sagittal.tif - a 3D image of the autofluorescence channel for the mid-sagittal sectioning of the Allen Mouse Brain atlas reference (to be used in place of “/reference/reference.tiff”).
 - annotation_25_half_sagittal.tif - a 3D segmentation of the Allen Mouse Brain reference (to be used in place of “/reference/segmentation.tiff”).
 - coords_25_half_sagittal.json - the coordinates of key points on the reference (to be used in place of “/reference/points.json”)
 - AllBrainRegions.csv - a mapping of region ID numbers in the segmentation to names of regions.

Use nuggt to inspect the included mouse brain reference atlas by entering the following command into the Docker terminal window:

```
nuggt-display --port 8999 [--ip-address 0.0.0.0] \
--segmentation /allen-mouse-brainatlas/annotation_25_half_sagittal.tif \
--points /allen-mouse-brainatlas/coords_25_half_sagittal.json \
/allen-mouse-brainatlas/autofluorescence_25_half_sagittal.tif reference gray
```

where “–ip-address 0.0.0.0” should be included by Windows and Mac users. The nuggt-display application will print a URL similar to “<http://127.0.0.1:8999/v/...>” for Linux users in the Docker terminal window. For Windows and Mac users, the nuggt-display application will print a URL similar to “[http://\(container-id\):8999/v/...](http://(container-id):8999/v/...)” in the Docker terminal window, and the container ID should be replaced with “localhost” in the next step.

- iv) Open the URL in your browser to see the Neuroglancer user interface. The browser should display four panels. The top left one is the XY view, the top right is the XZ view, the bottom right one is the YZ view, and the bottom left one is a 3D view. The current cursor position in image coordinates is displayed at the top of the Neuroglancer user interface. A list of keyboard shortcuts is available if you type “h” while using Neuroglancer.[? TROUBLESHOOTING](#)

In Neuroglancer, you can move the stack by pressing the left mouse button with the cursor in any of the three orthogonal view panels and dragging. You can scroll through the depth of the stack by turning the mouse wheel, and you can zoom in and out by pressing the “ctrl” key and turning the mouse wheel. Each layer in Neuroglancer listed along the top of the user interface can be hidden by clicking the layer name. Segmentation layers can be used to highlight specific brain regions by double-clicking regions in any view panel.

- v) Exit the nuggt-display application by holding “ctrl” and pressing “C” in the Docker terminal window.

Create a points file for a custom reference atlas

This step is optional if you are aligning a sagittal image of a mouse brain hemisphere to the Allen Mouse Brain Atlas (which is the case when using the example data). If you are using the example data, proceed to step C xii.

- vi) Locate either a 3D TIFF file of the reference image (e.g. “path_to_reference/reference.tiff”) or a folder of 2D TIFF files named in strict ascending alphabetical order (e.g. “path_to_reference/images/img_0000.tiff”) on the host.

CRITICAL STEP You must prepare an accompanying segmentation of this reference (e.g. “path_to_reference/segmentation.tiff”) where each pixel of the segmentation has a value corresponding to the region in which the pixel lies. You must also have a mapping of region number to the region’s name in a format similar to the file “/allen-mouse-brainatlas/ AllBrainRegions.csv”.

- vii) Open a terminal and start the Docker container with the reference image(s) mounted using the following command:

```
docker run -it --expose 8999 -p 8999:8999/tcp [--network host] \
-v path_to_reference:/reference -v path_to_data:/data chunglabmit/shield-2018
```

where “path_to_reference” and “path_to_data” represent the full paths of the directories containing the reference image(s) and the images to be aligned to the reference on the host. The “–network host” argument should only be included by Linux users.

CRITICAL STEP Add quotes around the full path if it contains any spaces.

- viii) If you have a 3D reference TIFF file, type the following command into the Docker terminal window:

```
nuggt --port 8999 --image /reference/reference.tiff --output /reference/points.json
```

where “reference.tiff” should be replaced with the name of your reference image. If you have a folder of 2D TIFF files, type:

```
nuggt --port 8999 --image "/reference/images/*.tiff" --output /reference/points.json
```

CRITICAL STEP Use “*.tif” instead of “*.tiff” if that is the extension of your image files.

- ix) The nuggt application will display a line similar to “Editing viewer: <http://127.0.0.1:8999/v/...>” in the Docker terminal window. Windows and Mac users should replace the container ID in the URL with “localhost”. Open the URL in your browser to see the Neuroglancer user interface.

- x) Add fiducial points by placing the cursor where you want the point to be, holding the “shift” key and pressing “A”. You can delete a point by placing the cursor over it, holding the shift key and pressing “D”. You should annotate the image using easily identifiable locations like the dentate gyrus as well as the perimeter of the image (see Supplementary Fig. 1).? TROUBLESHOOTING
- xi) Hold the “shift” key and press “S” to save the annotations. Bring up the Docker terminal window again, hold “ctrl” and press “C” to exit from the nuggt application.

PAUSE POINT The points.json file can be saved and reused for future atlas alignment tasks using the same reference image(s).

Perform automatic alignment

- xii) Determine whether the images to be aligned with the reference atlas needs to be flipped or rotated by inspecting the stitched and reference images.

If aligning to the provided sagittal mouse brain atlas, each z-plane of the stitched images should be approximately a sagittal section with the olfactory bulb at the top of the image and the cortex to the right (see Supplementary Fig. 1). The z-plane corresponding to the medial sagittal section should be the last image in the stack (the one that is the last in alphabetical order if 2D planes are used). If the cortex is at the left, you will need to “flip-X”. If the olfactory bulb is at the bottom, you will need to “flip-Y”. If the medial sagittal section is at $Z = 0$, then you will need to “flip-Z”. Note that “flipping” in this case means reversing the index of an image dimension, which corresponds to a reflection of the image in that dimension. ? TROUBLESHOOTING

If aligning the example data to the provided mouse brain atlas, then the Ex_0_Em_0 channel (containing syto 16 nuclear stain) should be used for atlas alignment and flipped in the X and Z dimensions (see Supplementary Fig. 2).

- xiii) Determine whether the channel to be aligned with the reference atlas needs to be cropped.

Typically, the reference image extends to the left, right, top and bottom with no background margins, but the stitched images to be aligned have a margin to the left, right, top or bottom. If these margins are large, they will prevent the automatic alignment from succeeding; thus, the image to be aligned must be cropped to match when performing the automated alignment. Note the X-start and X-end, Y-start and Y-end, and Z-start

and Z-end (if whole planes need to be cropped) coordinates of the image after cropping using FIJI to examine the images.

CRITICAL STEP These cropping coordinates apply to the image before flipping.

If using the full resolution example data, then use the following crop coordinates:

- X-start, X-stop: None
- Y-start, Y-stop: 0, 9800
- Z-start, Z-stop: None

If using the downsampled example data, then use the following crop coordinates:

- X-start, X-stop: None
- Y-start, Y-stop: 0, 1225
- Z-start, Z-stop: None

- xiv) Run the rescale-image-for-alignment program to rescale, flip, and crop the channel used for atlas alignment. If step (xiii) determined that the image needs X-flipping, use the `--flipx` switch, and similarly for Y and Z. Likewise, if step (xiii) determined the image needs Xcropping, use the `--clip-x` argument, and similarly for Y and Z. For example, if an image needs to be flipped in X and Z and cropped in Y at the bottom of the image at coordinate 9100, the resulting command to be typed into the Docker terminal window is:

```
rescale-image-for-alignment --input "/data/stitched_data/channel_alignment/*.tiff" \  
--atlas-file /reference/reference.tiff --output \  
/data/downsampled_flip-x_flip-z_clip-y-0-9100.tiff --flip-x --flip-z --clip-y 0,9100
```

where “channel_alignment” is the folder containing the stitched images of the channel used for alignment. If using the full resolution example data with the provided reference atlas, then type:

```
rescale-image-for-alignment --input "/data/stitched_data/Ex_0_Em_0/*.tiff" \  
--atlas-file /allen-mouse-brain-atlas/autofluorescence_25_half_sagittal.tif \  
--output /data/downsampled_flip-x_flip-z_clip-y-0-9800.tiff \  
--flip-x --flip-z --clip-y 0,9800
```

If using the downsampled example data with the provided reference atlas, then type:

```
rescale-image-for-alignment --input "/data/stitched_data/Ex_0_Em_0/*.tiff" \  
--atlas-file /allen-mouse-brain-atlas/autofluorescence_25_half_sagittal.tif \  
--output /data/downsampled_flip-x_flip-z_clip-y-0-1225.tiff \  
--flip-x --flip-z --clip-y 0,1225
```

```
--atlas-file /allen-mouse-brain-atlas/autofluorescence_25_half_sagittal.tif \
--output /data/downsampled_flip-x_flip-z_clip-y-0-1225.tiff \
--flip-x --flip-z --clip-y 0,1225
```

CRITICAL STEP Record the values for the –flip-x, –flip-y, –flip-z –clip-x, –clip-y and –clip-z switches in the output image name. These parameters will be used again in step C xxiv.

CRITICAL STEP If using the example data, make sure that Ex_0_Em_0, the syto 16 channel, is rescaled and used for atlas alignment.

- xv) Align the rescaled image to the reference using Elastix. If using a custom reference image in the same example scenario presented in step C xiv, then the following command would be used:

```
sitk-align --moving-file /data/downsampled_flip-x_flip-z_clip-y-0-9100.tiff \
--fixed-file /reference/reference.tiff --fixed-point-file /reference/points.json \
--xyz --alignment-point-file /data/alignment.json
```

CRITICAL STEP Substitute the name of your reference image for “reference.tiff” above and substitute the name you used as the –moving-file in step (C)(xiii) for “downsampled.tiff” above.

If using the full resolution example data with the provided reference atlas, then type:

```
sitk-align --moving-file /data/downsampled_flip-x_flip-z_clip-y-0-9800.tiff \
--fixed-file /allen-mouse-brain-atlas/autofluorescence_25_half_sagittal.tif \
--fixed-point-file /allenmouse-brain-atlas/coords_25_half_sagittal.json \
--xyz --alignment-point-file /data/alignment.json
```

If using the downsampled example data with the provided reference atlas, then type:

```
sitk-align --moving-file /data/downsampled_flip-x_flip-z_clip-y-0-1225.tiff \
--fixed-file /allen-mouse-brain-atlas/autofluorescence_25_half_sagittal.tif \
--fixed-point-file /allenmouse-brain-atlas/coords_25_half_sagittal.json \
--xyz --alignment-point-file /data/alignment.json
```

? TROUBLESHOOTING

Refine the alignment manually

- xvi) Use nuggt-align to manually refine the automatic alignment. If using a custom reference image in the same example scenario presented in step C xiv, then the following command would be used:

```
nuggt-align --port 8999 [--ip-address 0.0.0.0] \
--reference-image /reference/reference.tiff \
--moving-image /data/downsampled_flip-x_flip-z_clip-y-0-9100.tiff \
--points /data/alignment.json
```

where “–ip-address 0.0.0.0” should be included by Windows and Mac users.

CRITICAL STEP Substitute the name of your reference image for “reference.tiff” above and substitute the name you used as the –moving-file in step (C)(xiii) for “downsampled.tiff” above.

If aligning the full resolution example data to the provided reference atlas, then enter the following command in the Docker terminal window:

```
nuggt-align --port 8999 [--ip-address 0.0.0.0] --reference-image \
/allen-mouse-brainatlas/ autofluorescence_25_half_sagittal.tif \
--moving-image downsampled_flip-x_flipz_ clip-y-0-9800.tiff \
--points /data/alignment.json
```

If aligning the downsampled example data to the provided reference atlas, then enter the following command in the Docker terminal window:

```
nuggt-align --port 8999 [--ip-address 0.0.0.0] --reference-image \
/allen-mouse-brain-atlas/autofluorescence_25_half_sagittal.tif \
--moving-image /data/downsampled_flipx_ flip-z_clip-y-0-1225.tiff \
--points /data/alignment.json
```

- xvii) There are two links that are displayed by nuggt-align in the Docker terminal window. One is the link to a Neuroglander webpage displaying the reference image and one is a link to the image that is to be aligned. Copy each of the links and open them in separate windows in your web browser. Windows and Mac users should change the container ID in the URL to “localhost” (see step C iii).
- xviii) Refine the locations of each of the fiducial points in the image. This is done by selecting the reference image browser window (e.g. by clicking in it), holding down the “shift” key and typing “N”. A red point will appear in both the reference and moving image browsers. You should adjust the point in the moving image browser to correspond with its location in the reference image if it is placed incorrectly. This

is done by holding down the “ctrl” key and clicking on the location in the reference image where the point should be. The point can be readjusted multiple times until you are satisfied with the location. After this is done, hold the shift key down and type, “D” (for “done”) and hold the shift key down and type “N” to move to the next fiducial point. Repeat the adjustment procedure until all of the fiducial points have been adjusted. ? TROUBLESHOOTING

- xix) Hold the shift key down and press “S” to save the adjusted alignment.

CRITICAL STEP The location of the refined fiducial points are not saved automatically. The refined atlas alignment progress will be lost if the adjusted alignment points are not saved.

- xx) Hold the shift key down and type “W” to warp the image to be aligned to the reference image.

CRITICAL STEP Wait for the message, “Warping complete”, to be displayed before doing anything further.

- xxi) Add additional points to refine the warping further. Add a point to the reference image by holding the “ctrl” key down and pressing the mouse button while hovering over the location of a discrepancy. Focus the alignment image to this location by holding down the “shift” key and pressing “T” (for “translate”). In the alignment image Neuroglancer webpage, adjust the location of the point by holding down the “ctrl” key and pressing the left mouse button, then hold the shift key down and press “D” (for “Done”).

CRITICAL STEP Adding duplicate points in the same location will cause the warping to fail. To avoid this problem, it is helpful to warp the moving image after adding each point to verify that the warping is successful.? TROUBLESHOOTING

- xxii) Hold the shift key down and press “S” to save the adjusted alignment.

CRITICAL STEP The location of the refined fiducial points are not saved automatically. The refined atlas alignment progress will be lost if the adjusted alignment points are not saved.

- xxiii) In the Docker terminal window, hold down the “ctrl” key and press “C” to exit the nuggt-align program.

- xxiv) Rescale the alignment to the size of your original image. If using a custom reference image in the same example scenario presented in step C xiv, then the following command would be used:

```
rescale-alignment-file --stack "/data/stitched_data/channel_alignment/*.tiff" \
--alignmentimage /data/downsampled_flip-x_flip-z_clip-y-0-9100.tiff \
--input /data/alignment.json --output /data/rescaled-alignment.json \
--flip-x --flip-z --clip-y 0,9100
```

CRITICAL STEP replace “–flip-x –flip-z –clip-y 0,9100” above with the values used in step C xiv

If aligning the full resolution example data to the provided reference atlas, then enter the following command in the Docker terminal window:

```
rescale-alignment-file --stack "/data/stitched_data/Ex_0_Em_0/*.tiff" \
--alignment-image /data/downsampled_flip-x_flip-z_clip-y-0-9800.tiff --input
/data/alignment.json --output /data/rescaled-alignment.json --flip-x --flip-z
--clip-y 0,9800
```

If aligning the downsampled example data to the provided reference atlas, then enter the following command in the Docker terminal window:

```
rescale-alignment-file --stack "/data/stitched_data/Ex_0_Em_0/*.tiff" \
--alignment-image /data/downsampled_flip-x_flip-z_clip-y-0-1225.tiff \
--input /data/alignment.json --output /data/rescaled-alignment.json \
--flip-x --flip-z --clip-y 0,1225
```

PAUSE POINT The alignment.json and rescaled-alignment.json files can be saved for continuing the analysis at a later date.

Compute the total and mean intensity per region

- xxv) Use the rescaled alignment file to compute fluorescence statistics of each channel for all brain regions. If using a custom reference image, then enter the following command into the Docker terminal window:

```
calculate-intensity-in-regions --input "/data/stitched_data/channel/*.tiff" \
--alignment /data/rescaled-alignment.json \
--reference-segmentation /reference/segmentation.tiff \
--brain-regions-csv /reference/brain-regions.csv \
--output /data/results-level-7.csv --level 7
```

where “channel” represents the folder of the current channel to be analyzed.

CRITICAL STEP the “–level” argument picks the granularity of the segmentation description from 7 (finest granularity) to 1 (coarsest granularity). You can specify multiple levels to be calculated at the same time at little additional computational cost.

If aligning the full resolution example data to the provided reference atlas, then enter the following command:

```
calculate-intensity-in-regions --input "/data/stitched_data/Ex_1_Em_1_master/*.tiff" \
--alignment /data/rescaled-alignment.json \
--reference-segmentation /allen-mouse-brainatlas/annotation_25_half_sagittal.tif \
--brain-regions-csv /allen-mouse-brainatlas/AllBrainRegions.csv \
--output /data/results-level-3.csv --level 3 \
--output /data/results-level-4.csv --level 4 \
--output /data/results-level-5.csv --level 5 \
--output /data/results-level-6.csv --level 6 \
--output /data/results-level-7.csv --level 7 --shrink 2 -ncores N
```

where N is the number of cores to use for calculating fluorescence statistics. Note that using more cores causes the memory usage to increase as well. If memory becomes a limiting factor, then limit the number of cores used or increase the shrink factor if acceptable.

If aligning the downsampled example data to the provided reference atlas, then enter the following command:

```
calculate-intensity-in-regions --input "/data/stitched_data/Ex_1_Em_1_master/*.tiff" \
--alignment /data/rescaled-alignment.json \
--reference-segmentation /allen-mouse-brainatlas/annotation_25_half_sagittal.tif \
--brain-regions-csv /allen-mouse-brainatlas/AllBrainRegions.csv \
--output /data/results-level-3.csv --level 3 \
--output /data/results-level-4.csv --level 4 \
--output /data/results-level-5.csv --level 5 \
--output /data/results-level-6.csv --level 6 \
--output /data/results-level-7.csv --level 7
```

This command can be repeated for all other channels to be analyzed. The results file that is created contains a spreadsheet of the region names, the volume of each region in voxels, the sum of all intensities in each region (total_intensity) and the average intensity of the voxels in each region (mean_intensity).

Timing

For processing the full resolution example data:

Stage A, 30 min for setup and 2-4 h of unattended computer time

Stage B, 45 min for setup and 4-12 h of unattended computer time

Stage C, 1-2 h for setup and manual refinement and 4-12 h of unattended computer time

For processing the downsampled example data:

Stage A, 30 min for setup and 10 min of unattended computer time

Stage B, 45 min for setup and 20 min of unattended computer time

Stage C, 1-2 h for setup and manual refinement and 30 min of unattended computer time

Troubleshooting

A troubleshooting table is available in the online version of the protocol, which is available at <https://www.biorxiv.org/content/10.1101/576595v1>

Appendix 3: Supplemental Information

Chapter 1

Add supplemental figures here for SWITCH

Chapter 2

Add supplemental figures here for eFLASH

Chapter 3

Add supplemental figures here for MAP

Chapter 4

Add supplemental figures here for NP paper

Chapter 5

Add supplemental figures here for organoid phenotyping

Chapter 6

Add supplemental figures here for vascularization